

Vol. 12 Spring 2021

scientia

Undergraduate Journal of Scientific Research
University of Notre Dame

**Biggest Models of
2020: Modeling
COVID-19 in the
Perkins Lab**
PAGE 10

**Cytokine Storms
and SARS-CoV-2
Deaths**
PAGE 11

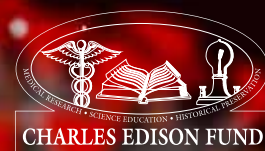
**Numerical
Investigation into
Modeling LEO
Orbital Decay**
PAGES 38-44

**Fluorinated
Compounds in Fast
Food Packaging**
PAGES 45-48



UNIVERSITY OF
NOTRE DAME

SCIENCE



Letter from the Interim Dean

Dear College of Science Undergraduates,

Undoubtedly, this has been a year unlike anything we have seen before. You have all faced academic, social, and health-related challenges, and yet you have persevered. Despite all of the difficulties, including ever-changing safety protocols and lab closures, many of you have continued to follow your passion for scientific research. The determination and flexibility you've developed through this crisis will serve you well in your scientific careers, or in whatever else you pursue.

Scientific research is fundamental to understanding and solving the world's most pressing problems, and unsurprisingly the COVID-19 pandemic has spurred scientific research at Notre Dame. In this issue you will read about COVID-19 surveillance research led by Professor Alex Perkins, and COVID-19 inflammation research led by Graduate Student Christina Oh. Other topics of interest include community-based learning in neuroscience and breakthroughs in cancer research from the labs of Professors Zhang, Baker and Littlepage.

Conducting research and learning to publish and effectively communicate your research is an essential part of the undergraduate experience at Notre Dame. The 2021 issue of Scientia features research conducted by juniors and seniors in topics such as physics, biology, medicine and health, and mathematics.

Scientia allows undergraduates not to submit research for publication, but also to produce an entire journal. Every step is student-led: from editorial planning to design and layout, undergraduate students make every issue of Scientia a reality. Participation in student research and in publishing research is a valuable experience. I encourage you to be a part of Scientia in the future, whether publishing your original research, serving an editorial role, or simply attending the engaging Talk Science lectures held throughout the year which feature a faculty member and a student talking about their research.

As Interim Dean, and on behalf of the faculty and staff of the College of Science, I wish to express my gratitude to you for your perseverance, resilience, and adaptability over this most difficult year. Your dedication to scientific discovery is a great inspiration to all of us.

In Notre Dame,

Michael D. Hildreth, Ph.D.
Interim Dean of the College of Science
Professor of Physics



Table of Contents

News

- 10 The Biggest Models of 2020: Lessons in Epidemiological Modeling through the Eyes of the Perkins Lab
- William Geoffroy
- 11 LOC Immunosensor for Detection of Cytokine Storms Has the Potential to Detect and Prevent a Leading Cause of SARS-CoV-2 Deaths
- Jack Heatherman
- 12 Mycobacterium avium Complex Infection Study Paves Way for Treatment
- Emily Hunt
- 12 CITE-seq Analysis of Immune Cells Highlights Transcriptional Plasticity in the Aged Brain
- Rafael Kuc
- 13 The 3-Dimensional Structure of Cancerous Antigens in Determining Immunogenicity and Possible Implications for Novel Cancer Vaccines
- Emily Kozlowski
- 15 Developmental Neuroscience and the Self-Healing Communities Initiative
- Noel Vincent
- 16 Insulin Upgrade: Using Supramolecular Motifs to Advance Diabetic Therapeutics
- Jackson Vyletel
- 17 Synaptic Mechanisms Impaired by Disease-Causing Mutations
- Madeline Cole
- 18 Littlepage Lab Bone Metastasis Research Opens Window into the Future of Cancer Treatment
- Allan George
- 18 The Zika Virus Epidemic: Reassessing Case Numbers and Global Impact
- Jared Meisel

- 19 Rhythmic, Diurnal Behavior of Sloths in Disturbed Forests of Northeastern Brazil
- Michael Marino
- 20 Using the Arctic Tussock to Study Carbon Cycling on Alaska's North Slope
- Michael Marino
- 21 Creating a Process for Optimizing Antibacterial Peptides
- Stephanie Swegle

Health & Medicine

- 23 Endoscopic Submucosal Dissection vs. Endoscopic Mucosal Resection for the Treatment of Colorectal Lesions: A Meta-Analysis
- Christian Oakley

Biology

- 29 Investigation of the Use of Camouflage in the Sally Lightfoot Crab (Grapsus grapsus)
- Abigail White
- 32 A Reproducible and Scalable Genome Assembly Pipeline for Sulfolobaceae
- John Le

Physics

- 38 A Numerical Investigation Into Modeling LEO Orbital Decay
- Andrew Langford
- 45 Fluorinated Compounds in Fast Food Packaging
- Molly DeLuca

Mathematics

- 49 Zeros of Riemann Zeta Function
- Yuxin Lin

Letter from the Editors

April 29, 2021



Since its establishment in 2009, Scientia has been an inclusive journal community dedicated to supporting and celebrating the scientific research of undergraduate students at Notre Dame. The students and faculty advisors of our journal work together to provide a voice for emerging scientists of all types, and we believe that students should have the opportunity to professionally engage in scientific publishing and editing. We welcome submissions of student research in any discipline in the College of Science and seek to provide equal representation of student contributions to biology, chemistry, health, physics, and mathematics.

We empower students to pursue their scientific goals not only through our annual publication of undergraduate research, but also through editorial board positions in the recruitment, editing, writing, and design process of our journal. This fall, because of the increasing student eagerness to become involved in our journal, we applied for and were awarded club status through the Student Activities Office at the University of Notre Dame. This new status as an official student organization will enable Scientia to increase our visibility on campus and provide new opportunities for underclassmen to engage in the

scientific writing community beyond journal publication, such as grant-writing workshops, science journalism career panels, and academic writing training. We also became one of the founding members of the National Undergraduate Consortium on Scientific Journalism, collaborating with undergraduate research journals across the nation to organize its first annual conference. We hope that this ongoing partnership will continue into the future for years to come.

This year, Scientia also faced the unprecedented challenges of the COVID-19 pandemic and its resultant effects on campus activities. We are exceptionally grateful for the adaptability of our staff, faculty, and guests who made this transition possible and supported our hybrid “Talk Science” seminars the past two semesters. We would particularly like to thank the editorial team for their flexibility and support in the publication process. We chose to focus portions of this issue on current research at Notre Dame related to COVID-19, including news features about epidemiological modeling in the lab of Dr. Alex Perkins and cytokine storm research by Ph.D. candidate Christina Oh.

We are so excited to see how Scientia will grow and what the new leadership will accomplish in the upcoming years, and we are exceptionally confident in passing the roles of Editors-in-Chief to Andrew Langford and Abigail Abikoye. They have shown an outstanding commitment to the success of our journal, and we look forward to what they and our excellent editorial team will accomplish for Scientia in the 2021–2022 academic year. Scientia, we will miss you!

In Notre Dame,

Aidan Crowley & Lauren English
Editors-in-Chief

2020–2021 Editorial Board

Editors in Chief

Aidan Crowley ’21
Lauren English ’21

Managing Editors

Abigail Abikoye ’22
Andrew Langford ’22

Outreach Coordinator

Megan McCabe ’21

Biology

Gretchen Andreasen ’21 (lead)
Olivia Jazbutis ’21 (lead)
Sarah Betts ’22 (associate)
Alex Dittmar ’23 (associate)
Michael Miramontes ’22 (associate)

Health

Meghan McReynolds ’22 (lead)
Emilia Wang ’21 (lead)
Stella Cho ’22 (associate)
Emily Hunt ’23 (associate)

Mathematics

Ting Gong ’21 (lead)
Alex Kokot ’21 (lead)
Alexa Morgan ’23 (associate)

Physics

Molly DeLuca ’22 (lead)
Rebecca Boyle ’23 (associate)

Chemistry & Biochemistry

Kimberly Riordan ’21 (lead)
Skyler Hamilton ’22 (associate)
Claire Nkwo ’22 (associate)
Eli Travis ’21 (associate)

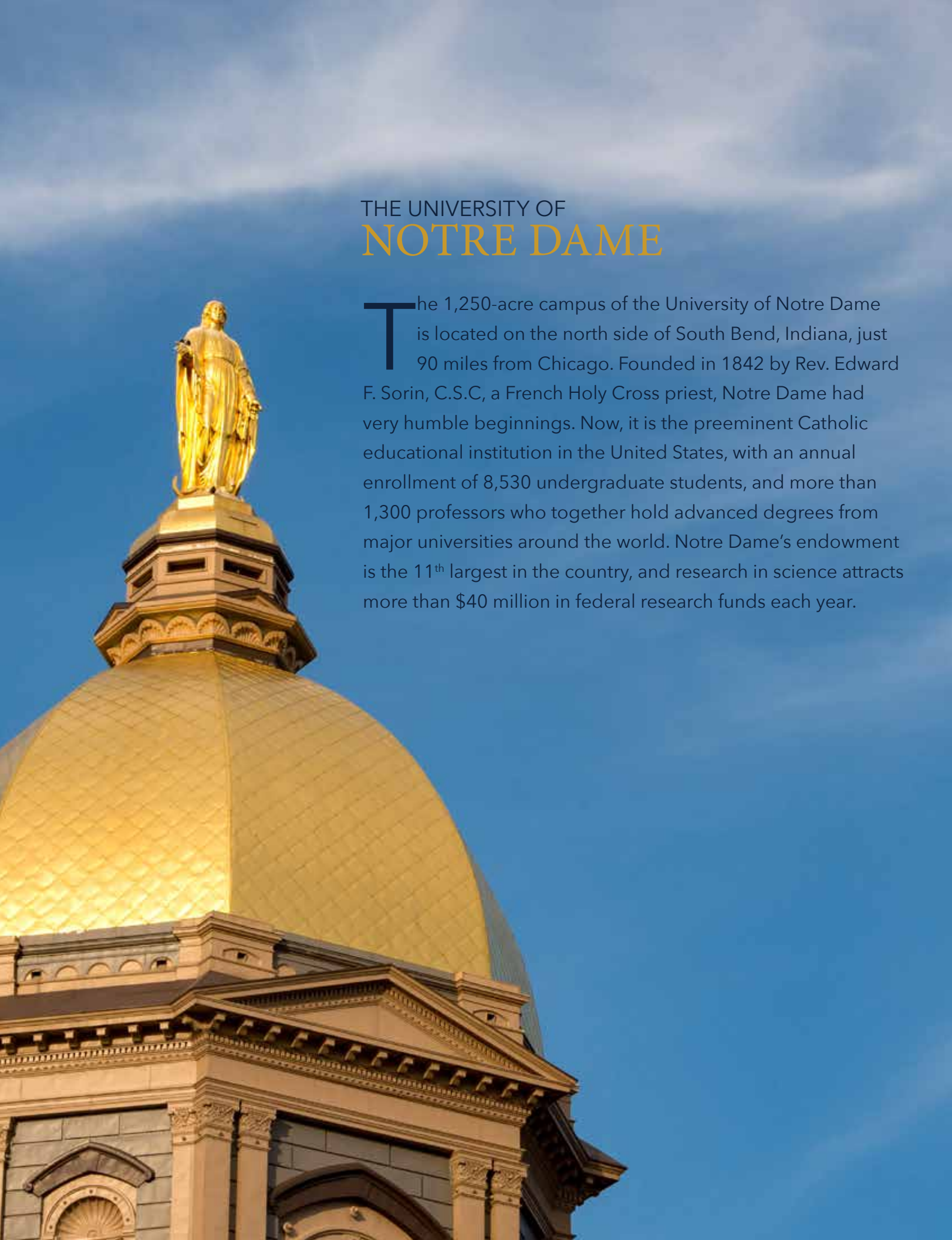
Layout, Design, & Publishing

Michelle Moskal ’22 (lead)
Erin Coyne ’22 (associate)
Matt Millado ’21 (associate)
Stephanie Swegle ’24 (associate)

News

Noel Vincent ’21 (lead)
Jack Heatherman ’23 (associate)
Alexandra Martinez ’21 (associate)
Alex Noble ’23 (associate)





THE UNIVERSITY OF NOTRE DAME

The 1,250-acre campus of the University of Notre Dame is located on the north side of South Bend, Indiana, just 90 miles from Chicago. Founded in 1842 by Rev. Edward F. Sorin, C.S.C, a French Holy Cross priest, Notre Dame had very humble beginnings. Now, it is the preeminent Catholic educational institution in the United States, with an annual enrollment of 8,530 undergraduate students, and more than 1,300 professors who together hold advanced degrees from major universities around the world. Notre Dame's endowment is the 11th largest in the country, and research in science attracts more than \$40 million in federal research funds each year.

RESEARCH

Want to get involved in undergraduate research? For more information about undergraduate research opportunities at the University of Notre Dame, visit science.nd.edu/undergradresearch.

Learn more about the Charles Edison Student Fellowship of *Scientia* on scientia.nd.edu or email scientia@nd.edu for details.



College of Science Faculty Spotlights



Christopher Patzke, Ph.D., the John M. and Mary Jo Boler Assistant Professor in the Department of Biological Sciences, studied biology and philosophy at the Freie Universität before earning his Ph.D. in developmental neurobiology at the Max Delbrück Center for Molecular Medicine. He continued his work in Developmental Neurobiology at the Max Delbrück Center for Molecular Medicine from 2009 to 2011 as a

postdoctoral research fellow. Then, in 2012, Patzke took his knowledge and expertise to Stanford University where he completed his postdoctoral research in the Department of Molecular and Cellular Physiology. He remained at Stanford until 2020 when he accepted a position as the John M. and Mary Jo Boler Assistant Professor in the Department of Biological Sciences at the University of Notre Dame. His laboratory within Notre Dame's Boler-Parseghian Center for Rare and Neglected Diseases studies the role of cell adhesion, synaptic signaling, and neuromodulation of signal transmission in the human brain. By combining various advanced disciplines of science including genetic engineering, cell imaging, biochemistry, brain organoid cultures, and physiology, his laboratory investigates the mutations that lead to several brain disorders. His use of human pluripotent stem cell-derived neuronal cells and brain organoid cultures allows him and his team to create models of brain cells to study the formation of the human nervous system and these mutations at a deeper level. Patzke shares his excitement about opening up his own lab and working on his ideas together with his team members within Notre Dame's creative, collaborative, and welcoming environment.



Kasturi Haldar, Ph.D., is a Rev. Julius A. Nieuwland, C.S.C. Professor in the Department of Biological Sciences and the James Parsons and Carrie Quinn Director for the Boler-Parseghian Center for Rare and Neglected Diseases. She earned her Ph.D. in biochemistry with the Department of Chemistry from Massachusetts Institute of Technology. She then went on to do a postdoctoral fellowship at Rockefeller

University in New York. Before coming to Notre Dame, she was an assistant and then associate professor in the Department of Microbiology-Immunology at Stanford University. She then went to teach as a Charles and Emma Morrison Professor of Pathology at Northwestern University School of Medicine from 1999 to 2008. Haldar's research aims to better understand disease pathology in order to develop treatments for rare and neglected diseases, especially neurological diseases such as Niemann-Pick Type C Disease. With the COVID-19 outbreak, Haldar has been researching the neurological symptoms and outcomes associated with the disease.



Dervis Can Vural, Ph.D., associate professor of condensed matter and biophysics, earned his B.S. in physics from Middle East Technical University in Ankara, Turkey, in 2002. He went on to receive both his M.S. and Ph.D. in physics from the University of Illinois at Urbana-Champaign. After doing a postdoc at Harvard, and then Yale, he accepted a position as professor of physics at the University of Notre Dame. His group

at Notre Dame focuses on using analytic and computational approaches to solve many-body problems surrounding statistical mechanics, complex materials, ecology, and evolution. At the intersection of many-body physics and biology, Vural's laboratory interests include research themes such as complex networks, population genetics and evolution, disordered/soft materials, many-body quantum mechanics, inverse problems, reliability theory, swarms, and active matter. Vural has published numerous papers, such as the recent publications "Predictive Maxwell's Demons," "Depletion force between disordered macromolecules," and "Evolution of Specialization in Dynamic Fluids" (2020). In the fall, he taught the course "Science Literacy" to Arts and Letters students, which was an exciting deviation from his typical math-focused courses, and in the spring he is teaching "Patterns of Life," which explores his research interest of modeling evolution and ecology. In addition to his research and teaching, Vural also has a strong interest in music. He plays the piano, harmonica, and various wind and percussion instruments from the Middle East, composes in multiple genres, and even has his own artist page on Spotify.



Jeff Schorey, Ph.D., is a George B. Craig Jr. Professor in the Department of Biological Sciences. He earned his Ph.D. at the University of Texas Health Science Center in San Antonio, Texas, in 1992. Afterward, he did a postdoctoral fellowship at the Washington University School of Medicine in St. Louis in the Division of Infectious Diseases from 1993 to 1996. He was an instructor of medicine

at the Washington University School of Medicine, and then came to Notre Dame as an assistant professor in 1998. Schorey's research focuses on tuberculosis, an infectious organism that kills approximately 1.5 million people each year. He is especially interested in the body's immunological response to tuberculosis because of the increase in drug-resistant strains of the disease. Schorey's goal is to develop better diagnostic tests and treatment for tuberculosis to eventually eradicate it through further cellular and immunological research.

College of Science Faculty COVID-19 Research Spotlights



Brian Baker, Ph.D., the Rev. John A. Zahm Professor and chair of the Department of Chemistry and Biochemistry, studied biochemistry at New Mexico State University before earning his Ph.D. in biochemistry at the University of Iowa. He continued his studies as a postdoctoral fellow at Harvard University. In 2001, he came to Notre Dame as an assistant professor and has been with the school since serving as

a professor, the director of graduate studies in the Department of Chemistry and Biochemistry, associate dean for research and graduate studies, and the founding director of the Integrated Biomedical Sciences Graduate Program. His laboratory studies immunology for cancer therapy with the Harper Cancer Research Institute. He works specifically with immune cells called T cells that can recognize virally infected cells as well as cancer cell antigens. By understanding T cell recognition, Baker hopes to engineer new T cells that are equipped to target cancer cells specifically. During the COVID-19 lockdown, most of the Notre Dame laboratories went into hibernation, and Baker was able to shift the focus of his work to the SARS-CoV-2 virus, which causes COVID-19. Since much of the research about T cells in cancer recognition involves first understanding viral immunology, Baker went back to that research to find parts of the SARS-CoV-2 genome that T cells may be able to recognize. Most of this work can be modeled on a computer, to see immune responses with hopes to create a therapeutic T cell vaccine. Upon returning to the laboratory, Baker was ready to validate what the computer model was predicting.



Alex Perkins, Ph.D., associate professor of infectious disease epidemiology in the Department of Biological Sciences and concurrent faculty in Applied and Computational Mathematics and Statistics (ACMS), studied computational ecology at the University of Tennessee, Knoxville, before earning a Ph.D. in population biology from the University of California, Davis. Following the completion of his Ph.D. in 2011, he

served as a RAPIDD Postdoctoral Fellow at both the University of California, Davis and the NIH Fogarty International Center until 2014. That same year, he joined the University of Notre Dame as an Eck Family Assistant Professor until 2020. In 2015 he took concurrent faculty member positions in the ACMS department and an associate professor in the biology department. The Perkins Laboratory within the Department of Biological Sciences applies mathematical, computational, and statistical approaches to model disease spread. Perkins's research is characterized by three themes: incorporating transmission dynamics into the mapping of infectious diseases, utilizing models to assess the efficacy of different forms of disease intervention, and exploring the dynamics of disease spread in the context of global change. In exploring these facets of epidemiology, the Perkins lab aims to improve our ability to understand the ways that our interactions with other organisms and the environment shape the spread of disease both locally and globally. Publications from the Perkins lab have focused on a variety of vector-borne diseases, including Zika virus disease, dengue fever, and, notably, COVID-19. In recent months, the Perkins lab has worked to gain a deeper understanding of the transmission of SARS-CoV-2, and its work is encapsulated in the recent publications "Estimating unobserved SARS-CoV-2 infections in the United States" and "Optimal control of the COVID-19 pandemic with non-pharmaceutical interventions." In the midst of one of the most severe global health crises in history, Perkins has drawn upon his unique background in statistics, computer science, and biology to help combat the immense uncertainty that surrounds this disease.

The Biggest Models of 2020: Lessons in Epidemiological Modeling through the Eyes of the Perkins Lab

WILLIAM GEOFFROY

There were many people whose efforts and expertise contributed to the ongoing fight against COVID-19. Nurses, doctors, and workers on the frontline dealt firsthand with COVID's initial surge and continue to serve our people. Workers of all kinds had to adapt to new environments to continue to provide us with a stable livelihood and sense of normalcy. Grocery stores, restaurants, and other businesses found creative solutions in the face of economic recession. Scientists and epidemiologists tried their hardest to stay one step ahead of the COVID curve, and individuals both inside and outside the scientific community contributed to the funding and development of vaccines, which will hopefully appear as a light at the end of our epidemiological tunnel. These and many others who go unnamed deserve our gratitude and recognition.

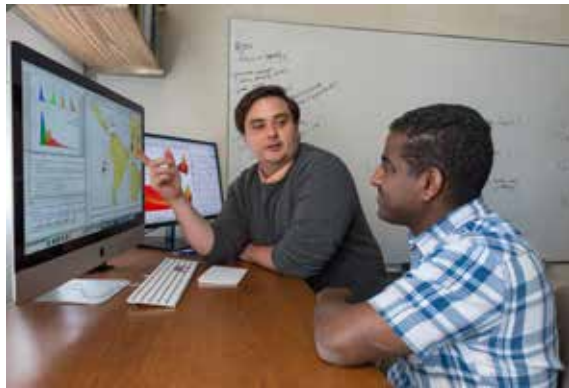
Among these people is a group of scientists and researchers dedicated to what one might call the “strategic” side of the COVID-19 response. These scientists are responsible for developing and refining mathematical models which help us analyze and sometimes predict the spread of disease. One of our very own, Dr. Alex Perkins, the Eck Family Assistant Professor of Biological Sciences, worked for the past year developing such models, and his insight on how they work supplies important lessons from both an epidemiological and societal perspective.

After pursuing a self-designed major in computational ecology at the University of Tennessee, Dr. Perkins went on to obtain a Ph.D. in population biology at UC Davis and did his postdoctoral fellowship with NIH on infectious diseases. Before the COVID-19 pandemic hit, the Perkins lab was dedicated to modeling the emergence and potential undetected presence of mosquito-borne illnesses such as dengue fever and the Zika virus, as well as the effects of “interventions” (such as vaccines, insecticides, and other preventive measures) on these diseases. As a result of their work in modeling these viruses, Perkins and his lab were not entirely ill-prepared to take on the challenge of the coronavirus.

Work at the Perkins Lab—and much of the COVID-19 response—relies on mathematical modeling. Dr. Perkins explains such a process in the following way: “Generically the concept of a model, whether it’s in disease modeling or other areas, is a simplified representation of the system. So if you think about a model car, it’s obviously not a real car, but it has a lot of the same parts and is put together in a very similar way.” With regards to the virus, models attempt to take all the relevant information into account to make predictions, test alternative “containment” strategies, or store data on the disease.

Early on in the epidemic, Dr. Perkins became interested in the possible discrepancy between the number of known cases in the U.S. and the number of cases that were actually

present according to the models. He found that in February 2020, early surveillance testing of the disease was not sufficient enough to measure the real number of COVID cases, and as a result, the large spike in cases came as a surprise to the U.S., leading to the increasing economic lockdown and toilet-paper panic of March which we all know and love. According to Dr. Perkins, while discrepancies in our knowledge of the spread are a recurring problem, “it’s really a function of two things—that is, how many tests are out there and available for people to use, and then how many people out there are infected. And so, prior to mid-March, when we did our initial analysis, that’s probably the worst that it’s been. Especially in February, we estimated that probably fewer than 10 percent of cases were being reported.” A more robust surveillance testing system at the start of the epidemic would have allowed precise and effective containment of the virus; this of course is a valuable lesson for future epidemiological issues.



Another important takeaway for epidemiologists (especially those focused on developing disease models) is that society takes time to respond to circumstances that are already assumed to be true in scientific fields. When asked if the pandemic came as a surprise to those in the epidemiological world, Dr. Perkins revealed a key dichotomy: “Epidemiologists in a lot of ways are not all that surprised about what has happened. I think a lot of people have been predicting that something like this would happen, it was just a matter of time.” It was more the case that the rest of society was shocked by the arrival of this new disease and its social repercussions. So on society’s part, a stronger scrutiny and understanding of science in general and the research and findings of epidemiologists in particular could inform future decisions in given scientific fields about issues that concern broad swaths of people.

Perhaps even more importantly, epidemiologists would benefit from input coming from outside the scientific community. As Dr. Perkins notes, “I would say the biggest [surprise]—to me—is that this is not simply a biological phe-

nomenon. So the biology of the virus and how it spreads plays a huge role, but the behavior of people, both on an individual level and also how policymakers respond and what kind of information gets portrayed in the media are all hugely consequential for this pandemic.” Future models of diseases which take into account many social factors would therefore better prepare people to make informed decisions about emerging diseases. “There was some recognition of the importance of behavioral feedback onto transmission before, but going forward we need more collaboration between epidemiologists and people who understand the social sciences and economics.”

LOC Immunosensor for Detection of Cytokine Storms Has the Potential to Detect and Prevent a Leading Cause of SARS-CoV-2 Deaths

JACK HEATHERMAN

Since its introduction to the United States in early 2020, the SARS-CoV-2 novel coronavirus has led to over 350,000 deaths and countless more hospitalizations. Of the near 1.8 million world-wide deaths recorded, over 20% can be traced to a rare immune event called a cytokine storm, an excessive immune response that often leads to multi-organ failure and eventual death. While the complications from coronavirus-induced cytokine storms are severe, early detection of an occurrence can prevent organ failure from taking place. In the Bohn lab at the University of Notre Dame, fourth-year Ph.D. candidate and 2020 Berry Family Foundation Graduate Fellowship recipient Christina Oh is using her expertise in both biochemistry and microfluidics to engineer a nanopore electrode array (NEA) immunosensor to detect cytokine storms in coronavirus patients before organ failure can set in.

Cytokine storms are the result of excessive immune responses caused by an overproduction of proinflammatory cytokine proteins. While cytokines typically induce healthy immune responses within cells, certain pathogens can induce the overproduction of proinflammatory cytokines. This large proinflammatory response causes the immune system to attack healthy organ tissues instead of the pathogens in question. While researching these coronavirus-induced cytokine storms, Oh came across a study which suggested that one particular cytokine, interleukin-6 (IL-6), is often a precursor to coronavirus-induced cytokine storms. Oh theorized that the creation of an IL-6 detection device would allow physicians to more easily identify and treat coronavirus-induced cytokine storms, events which were previously undetectable in early stages.

Utilizing her knowledge of microfluidics gained at the City College of New York, along with her biochemistry and biomolecular engineering expertise gathered from her time in the Bohn lab, Oh designed the NEA-based Electrochemical Lab-On-a-Chip (LOC) Immunosensor for the detection of cytokine storms. This nanofluidic device employs bunches of micropores, each only about 600 nm in diameter, through which biological samples will be circulated. Once the sample

While the COVID-19 pandemic is not yet over, now is a better time than ever to begin taking a closer look at the mistakes and triumphs scientists and other actors have made in the face of pandemic. While models serve as a key component of disease mitigation, this disease can serve as a model from which we may learn the best practices of science’s practical application and improve the relationships between scientists and society. ■

is run through the nanopores, an electrochemical sandwich enzyme-linked immunosorbent assay (ELISA) will selectively capture IL-6 cytokines on intrapore electrodes deploying target antibodies specific to IL-6. The device enables the rapid assaying and quantification of IL-6 levels in the patient’s blood. Additionally, the nanoscale device can fit in the palm of one’s hand, making it easily insertable into a patient.

According to Oh, detection of IL-6 in patients can predict up to 92% of coronavirus respiratory complications before they occur, allowing for timely distribution of ventilators and respiratory treatment before the cytokine storm can set in. Overall, she hopes that the device will reduce the number of coronavirus fatalities through early cytokine storm detection, prevention, and treatment.

Oh’s research was made possible through the mentorship of Dr. Paul Bohn, the Arthur J. Schmitt Professor of Chemical and Biomolecular Engineering at the University of Notre Dame. Oh expressed her gratitude to Dr. Bohn for his continuous support, as well as to the Advanced Diagnostics and Therapeutics Berry Family Foundation Graduate Fellowship Program for funding her research. “I was overwhelmed when I received the grant for this project as it allowed me to combine my interests in both biochemistry and nanoscale fluidics for the greater good,” Oh stated. “It was my interest in nanoscale sensors that brought me to Notre Dame in the first place, and I am honored and excited to be able to produce a device such as this to assist physicians in combating the coronavirus pandemic.” While Oh is still making tweaks to the device design, she anticipates having the LOC ready for medical trials by early 2021. Oh, who took a year of absence to develop the immunosensor, plans to resume her doctoral work upon the completion of the project. Once in the hands of physicians, the LOC will have a major impact on coronavirus treatment, hopefully preventing up to 20% of deaths through early-onset detection and treatment. ■

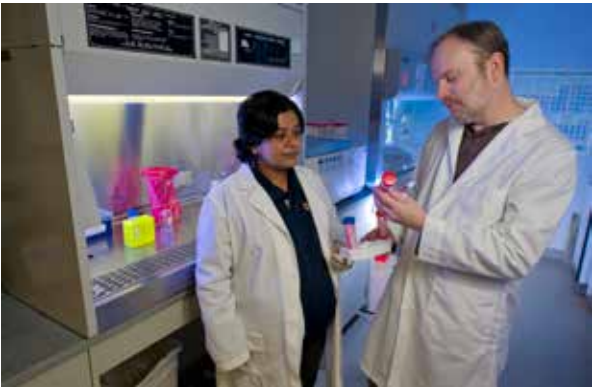
Mycobacterium avium Complex Infection Study Paves Way for Treatment

EMILY HUNT

The disease tuberculosis, which results in 1.5 million deaths each year, is caused by a group of bacteria called Mycobacteria. Mycobacterium avium complex (MAC) is a group of bacteria related to tuberculosis. While tuberculosis is an obligate human pathogen, meaning it is transmitted human to human, Mycobacterium avium (M. avium) is an environmental microbe transmitted through one’s surroundings, living in places such as water and soil.

Infection by M. avium can be transmitted in a variety of ways, such as by showerheads or hot tubs. Although the number of individuals who have a lung disease caused by M. avium is limited (~10 per 100,000 individuals), the number of cases are increasing approximately 5% each year with little understanding of this sudden rise.

Dr. Jeffrey Schorey, the George B. Craig Jr. Professor of Biological Sciences at the University of Notre Dame, is a researcher of the pathobiology of Mycobacterial diseases. A study from his lab brought light to how RNA sensors play a critical role in eliciting a response in T lymphocytes (T cells), which are cells of the body’s adaptive immune response that play an essential role in fending off diseases such as MAC. A MAC infection can be life-threatening to those with severely suppressed or compromised immune systems who are not taking proper treatment. While symptoms of the disease vary with the site of infection, the lungs are the primary site due to their unique microenvironment which differs from other major bodily organs.



When an individual is infected with MAC, Mycobacterium RNA is recognized by the RIG-I/MAVS/TBKI RNA sensing pathway and is activated as a result. The activation of this RNA-sensing pathway in infected cells stimulates the production of ICAM-1, a ligand-receptor protein involved in cell-cell adhesion in cells such as the T cell LFA-1. The upregulation of ICAM-1 in cells infected with MAC helps activate the acquired immune system by promoting T cell binding to infected cells which in turn promotes bacterial killing.

While much of what is currently understood about MAC stems from tuberculosis research, there are two main conclusions from Dr. Schorey’s research. The first is “what applies to TB [tuberculosis] and its pathogenesis doesn’t necessarily apply to Mycobacterium avium in its pathogenesis,” said Dr. Schorey. “Even though they’re both Mycobacteria... both intracellular pathogens, their mechanism of virulence definitely differs and we need to better understand what makes MAC pathogenic.” This understanding can lead to better treatment of the disease, leading to Dr. Schorey’s second takeaway: “We need more effective antibiotics.”

Better understanding of the pathogenesis of MAC is essential to develop effective vaccines and treatments. A large challenge in controlling the spread of Mycobacterium diseases in recent years is the increase in multi-drug-resistant strains. Individuals not taking their full course of antibiotics is a large contributing factor to this increase. “Drug resistance is such a problem with these mycobacteria. If you treat them with just one drug, it’s highly likely some bacteria will mutate and become resistant to the antibiotic,” said Dr. Schorey.

MAC cannot be treated with the same drugs as tuberculosis. Progress toward developing new vaccines and drugs for MAC and tuberculosis is not as rapid as for other types of infections, such as SARS-CoV-2, due to mycobacterial disease prevalence being primarily in low- and middle-income nations that have fewer resources to develop new treatments. Dr. Schorey and his team are currently working in conjunction with Dr. Marv Miller in the Department of Chemistry and Biochemistry and others in the US and Japan to develop new antibiotics to treat MAC infections. ■

CITE-seq Analysis of Immune Cells Highlights Transcriptional Plasticity in the Aged Brain

RAFAEL KUC

Longer life expectancies lead to an increased prevalence of neurological disorders and disability. In addition to the direct cellular changes caused by aging, disruption in the gut microbiome (dysbiosis) can impact neurological health

through changes in plasticity of brain immune cells. The development of both preventive strategies and treatment options is key to maintaining a healthy microenvironment in aged brains. However, the exact cellular changes leading to neurodegenera-

tion are not yet fully understood.

Samantha Golomb, a biology graduate student at Notre Dame, recently published a profiling study in Cell Reports that sheds light on immune cell plasticity during aging and gut dysbiosis. Golomb and her team performed cellular indexing on immune cells in the brains of young and aged mice with and without antibiotics-induced gut dysbiosis. Their findings show transcriptional plasticity of monocytes and lymphoid cells in the aged brain which is relevant to understanding neurological disease. Differentiated immune cells in the brain may undergo transcriptional changes to adapt and respond to aging, disease, infection, etc.

“It is already known that there are a lot of protein and immune factors that change when the brain ages. We wanted to study how gut dysbiosis on top of aging influences immune cells in the brain,” said Golomb. Specifically, her paper highlights that aged mice experienced an increase in innate lymphoid cell (ILC)-like cells that express a T memory stemness (Tscm) signature. However, in mice with induced gut dysbiosis, these ILCs were less prevalent. This finding is consequential as Tscm-like cells and ILCs are associated with increased chronic inflammation in brain tissue.

The team’s findings play an important role in the understanding of neuroinflammation and neurodegenerative disease. “Some of the immune cell changes might be encouraging additional infiltration of immune cells from the peripheral immune system. If more of those cells are coming into the brain and causing damage, that can be an issue,” explains Golomb. The team’s research builds a foundation for future studies on the association between age, the gut microbiome, and neurological disorders.

To extrapolate their results, Golomb and her team used a noteworthy and exciting cell analysis technique called Cellular Indexing of Transcriptomes and Epitopes by Sequencing, CITE-seq for short. CITE-seq combines two widely used techniques: single-cell RNA sequencing, which looks at the transcriptional profile of single cells, and single-cell mass cytometry, which looks at surface protein expression on single cells. According to Golomb, “CITE-seq allows us to

use the term plasticity. It is hard to define if a cell particularly resembles a subtype, but has a different gene or RNA profile and a different function. CITE-seq allows us to bridge that gap because defining cell types is more effective when looking at the surface protein expression profile.” Golomb’s team mapped immune cell plasticity in response to aging and gut dysbiosis. First, the cells’ surface protein profiles were examined to characterize them into subtypes, which Golomb explains is a “more traditional way of subtyping.” Then, within their identities, transcriptional profiles were examined to see if certain cell types were changing or shifting their transcriptomes. In this way, the team was able to effectively differentiate between specific cell subtypes.

Following publication of these findings, Golomb hopes to lead another project focusing on how the gut microbiome influences breast cancer metastasis to the brain. Her published findings provide groundwork for speculation; because the gut microbiome influences immune cells in response to aging and dysbiosis, they hypothesize that gut dysbiosis may alter immune response against brain metastasis as well. A better understanding of immune cell plasticity in response to these stimuli could lead to the development of clinical therapeutic interventions for neuro-related neurological disease. ■



The 3-Dimensional Structure of Cancerous Antigens in Determining Immunogenicity and Possible Implications for Novel Cancer Vaccines

EMILY KOZLOWSKI

Immunogenicity describes the ability of a substance to elicit an immune response. T cells, or T lymphocytes, a type of white blood cell, play an active role in the immune system by identifying foreign substances and accumulating a supply of memory T cells. In viral immunology, T cells can recognize the threat of a virus because of both the dissimilarity of the virus compared to healthy cells and the abundance of the virus in the body. After recognition, the T cells stimulate an immune response and generate memory T cells that can quickly react to

the same viral substance should they encounter it again. This phenomenon explains the general success of preventive viral vaccines.

Since T cells recognize substances that differ from our healthy, normal cells, cancer cells can often fail to evoke a significant immune response. Cancer results from mutations in the genome, causing a deformation of our normal cells into unspecialized cells with unchecked replication. This often leads to the formation of malignant tumors, with the exception of

some types of cancer, including blood cancers. Because cancerous cells are mutated versions of our regular cells, they can be the result of very minor changes to the genome and amino acid sequences, leading to cancerous cells and proteins that appear very similar to their wildtype (normal) counterparts. This similarity allows cancer cells to go unnoticed by the immune system as T cells fail to identify them as foreign.

The lab of the University of Notre Dame's Dr. Brian Baker, the Rev. John A. Zahm Professor of Structural Biology and Chair of the Department of Chemistry and Biochemistry, focuses on T cell recognition of targets and the effect of the 3-dimensional structure of both the targets and the receptors. In a paper published in *Nature Chemical Biology* in August 2020, Dr. Baker and his collaborators show that the 3-dimensional structures of peptides can differ largely from predictions based on the amino acid sequence, as seen by their observations of altered peptides with X-ray crystallography. Their paper suggests that the major histocompatibility complex-presented peptide they worked with yielded "an immunogenic tumor neoepitope" (neoepitope referring to a class of cancerous mutant peptides recognized by T cell receptors) when immune tolerance was expected, explaining that the mechanism causing immunogenicity "would not be predicted from sequence alone, emphasizing the importance of incorporating structural and associated physical principles into approaches for evaluating neoepitope immunogenicity" (Baker et al., 2020).

Identification of neoepitope structures (cancerous structures that successfully trigger a T-cell immune response) also has implications in developing novel cancer therapies known as cancer vaccines. Unlike most viral vaccines, these cancer vaccines would be therapeutic rather than preventive. By injecting a patient with synthesized neoantigens specific to their cancer, the immune response could be greatly intensified. As Dr. Baker described it, "it takes a lot to activate a T cell, and so a lot of times these tumors might have these antigens, but they're just not there enough to actually turn on a T cell. Once T cells are turned on they're much more sensitive." By increasing the abundance of a certain neoantigen in a cancer patient, T cell recognition could trigger an otherwise absent or minimal immune response, resulting in an immune system more sensitive to the presence of cancer cells containing the injected neoantigens.

When asked about the possibility of using this technology for preventive cancer vaccines, Dr. Baker responded that they are "not anywhere near to doing those experiments... that's a next-generation kind of question." However, he described current research done on public neoantigens, cancerous antigens that are common to a large population of cancer patients. For example, Dr. Baker's collaborators at Memorial Sloan Kettering have identified a public neoantigen shared between 60–70% of breast cancer patients. Public neoantigens are ideal candidates for therapeutic vaccines since patients with the neoantigen would not require vaccines catered specifically to them. Dr. Baker describes that these public neoantigens are also the link between current experiments on therapeutic cancer vaccines and future experiments on preventive cancer vaccines.

While it would seem that a public neoantigen injection would generate a reserve of memory T cells efficient in eliciting a quick immune response when exposed to the injected neoantigens, this would not necessarily be the case. Cancer cells can quickly adapt to their environment; they are much more resilient than viruses in this manner. Dr. Baker describes that one of the major concerns regarding a preventive cancer vaccine relying on memory T cells is that cancer cells "learn how to pump out little molecules that tell the T cells to go to sleep." However, there are now certain drugs called checkpoint inhibitors that are able to block these T cell-deactivating molecules. In terms of using public neoantigens in preventive cancer vaccines, Dr. Baker says, "If you can identify so-called public neoantigens, you now have an opportunity to make a preventative cancer vaccine out of that antigen. And so people are starting to identify some of these and that conversation is beginning to be had; some clinical trials are beginning to be held."



The Baker lab's work on the importance of 3-dimensional structures in determining T cell recognition forms the basis for novel cancer therapeutic vaccines. Before a potential antigen for a vaccine could be selected, the structure of the mutant protein first needs to be understood, and this 3-dimensional structure is shown to rely on many more factors than only the amino acid sequence. From there, neoepitopes can be identified and potentially used in a therapeutic vaccine. There is still much more experimentation required before the production of these therapeutic vaccines, and Dr. Baker voices one of the biggest challenges in current cancer immunology research—"We don't know what we don't know yet." Though the process of observing and identifying neoepitopes, as Dr. Baker and his collaborators did in their 2020 study, is unrealistic to perform for each cancer case, they are hopeful about the increasing accuracy of peptide-major histocompatibility complex structural modeling and its capacity to help predict promising neoantigens in individual cancer cases. ■

Developmental Neuroscience and the Self-Healing Communities Initiative

NOEL VINCENT

The advent of modern neuroscience has spurred a growing awareness of the behavioral implications at the intersection of environmental adversity and health. According to local research conducted by Beacon Health System of Michigan and Indiana, childhood trauma and violence are among the leading health concerns for the South Bend area. At the University of Notre Dame, in partnership with Beacon Health System and United Way of St. Joseph County, a Self-Healing Communities Initiative is being deployed to bridge the gap between theory and practice of neuroscience in an effort to empower the local community.

"The model for Self-Healing Communities includes working in earnest partnership with community organizations," described Dr. Nancy Michael, director of undergraduate studies for the neuroscience and behavior major in the College of Science. This model gives leaders of local community organizations, who may understand the problems they face better than external researchers, the ability to take ownership in the resolution of their most difficult problems while simultaneously leveraging the expertise of trained neuroscientists.



Dr. Michael joined the College of Science in 2014 and played an integral role in the development of the neuroscience and behavior major (NSBH). Since its inception, NSBH has been a popular course of study for undergraduate students. According to Dr. Michael, while the problems affecting South Bend in 2014 were reasonably understood, the community was less sure about how to most effectively and intentionally address these issues. In response, the Adverse Childhood Experiences (ACE) Interface was brought to South Bend in 2015 to raise awareness of the impact of childhood adversity on long-term community-level health. "If we just took care of kids and supported people better, we could do a lot better from a community perspective," emphasized Dr. Michael, who took part in early discussions with ACE Interface in the South Bend community.

Students in Dr. Michael's Developmental Neuroscience class take part in this community-based learning experience as part of their coursework. They apply the principles of

neuroscience and trauma-informed care that they have learned in the classroom to the level of the community and translate this knowledge into practical tools that local organizations can use.

One example of a recent student project is a training video made for the E. Blair Warner Clinic, a local primary care clinic that sees a patient population highly composed of Medicaid beneficiaries. The clinic was facing a high rate of turnover and burnout among its front office staff, relative to the resident physicians who provided clinical care. While the medical residents had received education in trauma-informed care, the front office staff had never been explicitly trained in strategies to deal with common behavioral presentations among the clinic's patient population. The student-developed training video leveraged academic knowledge about neuroscience, epigenetics, adverse childhood experiences, and resilience (the NEAR sciences) and delivered it to the front office staff to support them in their journey toward becoming trauma-informed.

Beyond collaborating to increase the capacity of community organizations, another objective of the Self-Healing Communities Initiative is to measure the impact of such interventions through a follow-up course called "Brain Health: Community-Engaged Research." According to Dr. Michael, data collection and assessment may not always be a top priority for nonprofit organizations working to alleviate social issues, especially those with tight or underfunded budgets. This presents another opportunity for the initiative to provide value to community organizations. In the example of E. Blair Warner Clinic, the student project can look beyond initial content understanding and into longer-term measures of compassion, empathy, and theory of mind, all working toward the goal of reducing staff burnout and turnover and increasing clinic capacity to address social needs.



"A better understanding of neuroscience is a better understanding of ourselves," said Dr. Michael, who was awarded the Society of Neuroscience Next-Generation Award for Education and Community Engagement by the Society of Neuroscience for her work in spearheading this project. "The

way I approach education and research is to think about how we might give opportunities for more stable communities,” said Dr. Michael. “I do the things I do because I want to be the best

teacher and the best mentor, and leave the world in a little bit of a better place.” ■

Insulin Upgrade: Using Supramolecular Motifs to Advance Diabetic Therapeutics

JACKSON VYLETEL

Insulin—possibly the word most frequently associated with diabetes. The high school definition of blood sugar regulation usually goes as follows: When animals eat, the sugars from food get converted to glucose in the bloodstream. Naturally, the body reacts to this change by secreting insulin from the pancreas, which transports the glucose from the blood to the cells that need it (more commonly cells that store it as glycogen). But is insulin all there is to it? One major component that is often left out of AP Biology classrooms is the function of amylin. Amylin, a peptide hormone, is co-secreted with insulin from the same pancreatic cells and plays a central role in blood sugar regulation. In turn, amylin function is lost when insulin function is lost. To combat the loss of amylin function, it can be beneficial to use an analog. The therapeutic equivalent of amylin is pramlintide, which mimics amylin function in the body and greatly improves insulin efficacy. Pramlintide, an adjunctive therapy, works with insulin to improve GI function, promote satiety, and even stimulate weight loss for some diabetics. Unfortunately, pramlintide’s therapeutic advantages are hindered by its lack of practicality for users. Pramlintide and insulin are not able to be injected from the same vial due to differences in solubility. For diabetics, this would translate to a second injection needed at mealtime, one for insulin and a separate one for pramlintide. In other words, it has been difficult to successfully utilize insulin and pramlintide together due to their differing molecular characteristics hindering their compatibility.

Insulin therapeutics became a topic of research for Dr. Matthew Webber, now professor of chemical and biomolecular engineering at the University of Notre Dame, during his postdoctoral training at the Massachusetts Institute of Technology (MIT). In this time, Dr. Webber and his colleagues started experimenting with synthesizing glucose-responsive insulin therapeutics. Their 2015 publication titled “Glucose-responsive insulin activity by covalent modification with aliphatic phenylboronic acid conjugates” demonstrated one of the first examples of glucose-responsive function for an insulin drug. At the time, Dr. Webber was working to modify insulin directly, which is difficult due to the limited number of available modification sites on the protein. This challenge led Dr. Webber to collaborate with his colleague, Dr. Eric Appel, to develop a strategy to modify the insulin protein non-covalently. The non-covalent modification of insulin offered a more scalable approach to the generation of improved insulin formulations to achieve better therapy. This protein formulation strategy was published in 2016 in a paper titled “Supramolecular PEGyla-

tion of Biopharmaceuticals.”

The team next explored this strategy as a way to afford co-formulation of pramlintide and insulin in the same vial. As opposed to the current standard of care necessitating separate injections, such an approach would enable insulin and pramlintide to be administered concurrently in a single injection or infusion, despite their naturally differing solubility profiles. To achieve this outcome, the team explored a new use for their previously developed cucurbit[7]uril-conjugated poly(ethylene glycol), or CB[7]-PEG, which enables insulin and pramlintide to have similar solubility profiles at physiological pH. Their co-delivery also translates to the simultaneous availability of the pramlintide and insulin to the body. This feature better mimics the function of a healthy pancreas, as these molecules are secreted by the pancreas at the same time in the healthy state. As illustrated in their 2020 publication titled “A co-formulation of supramolecularly stabilized insulin and pramlintide enhances mealtime glucagon suppression in diabetic pigs,” the research team found that utilizing this approach of non-covalent modification holds promise for improving the lives of diabetic individuals.



Dr. Webber and his collaborators are looking to further this research, and are exploring the integration of their formulations into automated delivery systems. With further research and testing, Dr. Webber and his team are hopeful for future scaled production of novel insulin formulations empowered by CB[7]-PEG. They are looking to bring this technology to market, which would improve the lives of many diabetic patients. They are also working to conduct research in scaled-up manufacturing and to better understand safety and toxicology toward advancing those aspirations. ■

Synaptic Mechanisms Impaired by Disease-Causing Mutations

MADELINE COLE

At a cellular level, the human brain is made up of billions of neurons, each connected through an intricate network of synapses. Information is passed between synapses in the form of neurotransmitters or electrical impulses, providing information necessary for the body to function properly. Because these synaptic connections transmit information for vital cellular processes, they can be affected and impaired by different disease-causing mutations. Changes that occur at the synaptic level can provide excellent models for different diseases, offering insight into potential treatments and therapeutic agents.

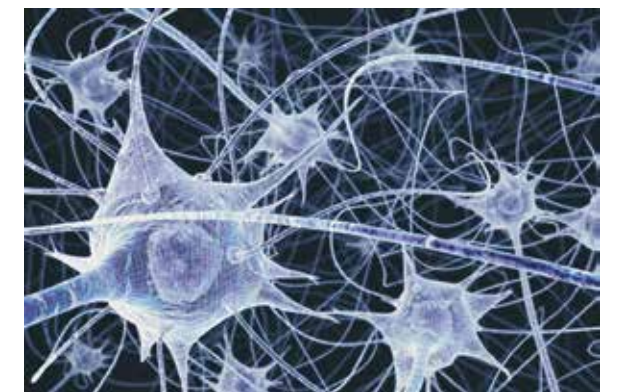
Neurobiologist and new Notre Dame John M. and Mary Jo Boler Assistant Professor in the Department of Biological Sciences Dr. Chris Dr. Patzke focuses his research on the molecular makeup and functioning of the nervous system. Dr. Patzke uses pluripotent stem cells to look at cellular processes impaired by genetic mutations underlying many pathological conditions such as epilepsy, schizophrenia, and autism. He describes his research as “basic science with a translational goal.” He aims to “understand how molecular processes in neurons work and how they are undermined in disease. The goal is to find ways to bypass any impaired signaling pathways and alleviate disease conditions based on their causes, not only on their symptoms.”

Having previously studied cell adhesion proteins and their role in brain development, Dr. Patzke first began his work with human neurons while working as a postdoctoral researcher at Stanford University. New technological developments in biomedical research, including rapid advances in genome sequencing, robust methods to derive human pluripotent stem cells without the use of embryos, and the introduction and optimization for laboratory purposes of site-specific nucleases for genome-editing have allowed biologists like Dr. Patzke to use human neurons as model systems for various pathologies. Using these advanced techniques to create models of the human nervous system allows for the potential to create agents that bypass disrupted signaling pathways and treat pathological conditions.

The usefulness of human neurons as a model system lies in the fact that they allow for a connection between the physical symptoms of a disease and analysis of the underlying

cause. Dr. Patzke explains that “the exact biological impact of genetic variants remains elusive and the causality to the clinical disease presentation is an area of active investigation. Approaches like human neurons are one way to bridge that gap. They offer the opportunity to model diseases in the culture dish but are also an excellent tool to figure out mechanisms.”

Dr. Patzke’s interest in the study of neuroscience and biology stemmed from his early interest in philosophy. As a student in Berlin, he became fascinated with epistemologists René Descartes and Immanuel Kant. He began to pursue biology, specifically neuroscience, as a way to “learn more about the functioning of the human mind and modern approaches to solve the mystery of how thinking works.” Eventually, this led to him working with human nerve cells. One specific branch of Dr. Patzke’s research focuses on neuromodulation and the impact of neuromodulators such as serotonin and epinephrine on synaptic transmission. He notes that past research has indicated that the presence of neuromodulators can act to increase or decrease the number of vesicles containing neurotransmitters, effectively altering the synaptic connection. Dr. Patzke notes that this area of study, and the application to therapeutic agents such as cannabinoids, warrants further study. Future research on neuromodulators and synaptic transmission can provide insight into the underlying mechanisms behind some of the most troublesome diseases, bringing us much closer to finding potential therapeutic agents and cures. ■



Littlepage Lab Bone Metastasis Research Opens Window into the Future of Cancer Treatment

ALLAN GEORGE

Bone metastasis is an incurable condition that often-times proves fatal for those affected. Metastasis is when the original cancer cells spread through various pathways in the body to other sites and proliferate. When metastasis occurs, the focus of the treatment is to slow the growth of the cancer and reduce the pain as there is currently no treatment that eradicates the disease permanently. In order to start researching different methods of treatment, there needs to be certain models developed that can help cancer researchers as a whole.

Through the work of Ricardo Romero Moreno, a former graduate student in the Littlepage laboratory, an ex vivo cell culture model was able to be developed. This model ensured a proper, replicable way of studying bone metastasis in the laboratory. In addition, this cell culture model enables bones in model organisms, such as mice, to be properly extracted to further study metastasis. This novel study works with mice in preclinical trials in the hope that these results can work with humans as well. This model is important for achieving replicable treatment of metastasis.

The Littlepage laboratory was also able to identify two new key players in bone metastasis: CXCL5 and its receptor CXCR2. These two are important in the process of cancer cells escaping the primary tumor and going to other sites such as the brain, bone, liver, etc. The cancer cells can travel to the bone and then remain dormant till activated. In this activation process, the CXCL5 and the receptor CXCR2 are involved. In order to come to this conclusion, there were many different experiments that had to be done. Some of these experiments include isolating cancer cells and adding certain proteins such as CXCL5. The Littlepage lab would observe the effects of different proteins and the proliferation of the cancer cells and draw conclusions from these interactions. Mice were injected with an intracardiac injection to prime the bones for metastasis to establish cancer cells, and then antagonists for CXCR2 were added to the primed bones in an ex vivo culture system. The researchers saw a decrease in proliferation which highlighted the role of CXCR2-CXCL5 axis in the bone metastasis process.

Some difficulty arose in this research process when trying to discover how to document the work, or more specifically, how to image the bone metastasis in the mice models as metastasis are small lesions. Antagonists or inhibitors need to be developed and used to study the effect of the protein of choice in cancer proliferation. Thankfully, the Littlepage lab was able to find an antagonist to study CXCR2's role in cell proliferation in bone metastasis, but there is much more work to be done in order to make it more potent.

Graduate student Maria Cristina Miranda-Vergara states, "Ideally, a preclinical model that utilizes both the inhibitor to CXCR2 and mechanical loading of the bone in a combination therapy could improve the outcome in mouse models." Combination therapy is needed when addressing bone metastases as there is no singular method that when used alone can cure the condition. If mice trials go well, the lab hopes to move forward with human trials in the coming years. Combination therapy is the future for cancer research with the goal of curing a patient's cancer once and for all. ■



The Zika Virus Epidemic: Reassessing Case Numbers and Global Impact

JARED MEISEL

A study performed by Notre Dame researchers shows that during the 2015–2018 Zika virus outbreak in Latin American countries, the number of Zika cases reported was less than 1 percent of the actual number of infections. The mosquito-transmitted Zika virus is particularly dangerous for

pregnant women because it causes microcephaly. Microcephaly results in newborn babies having significantly smaller than average-sized heads, and can lead to other complications such as intellectual disabilities and dwarfism. While the study's results show low risk of outbreaks in the immediate future, the great

degree of underreporting still displays a need for improved viral surveillance systems.

According to Dr. Sean Moore, the lead author and an assistant research professor in Notre Dame's Department of Biological Sciences, the study was prompted by a number of factors indicating that underreporting had occurred. Firstly, a significant portion of Zika patients are asymptomatic or experience only mild symptoms, such as fever or rash. A doctor's visit and thus a test or diagnosis would not likely result from these less severe situations. Additionally, the higher infection rate of routinely tested pregnant women as compared to the rest of the population suggested that Zika was spreading more than the official numbers indicated. "Unlike in the general population, when pregnant women in some locations went in for their wellness exams they were being screened to see if they had been infected with Zika. So we had data that was specifically from pregnant women, and the reporting rate in pregnant women was higher than it was in the general population," says Dr. Moore. The considerable number of news reports detailing the prevalence of the sickness also indicated that there were more cases of the virus than were officially reported during the epidemic.

Once the researchers determined that underreporting occurred, they used a Bayesian statistical model, along with the limited data that was available to them, to find out the extent of the underreporting in various localities. "If you have a certain number of microcephaly cases reported, then you can extrapolate how many pregnant women were infected from that. Furthermore, you can extrapolate beyond that to the total population if you assume that pregnant women are affected at the same rate. The model has assumptions like that built in," says Dr. Moore. Additionally, the prevalence of the Guillain-Barre

syndrome, which occurs in 1 out of every 10,000 Zika patients, was recognized and used to formulate a prediction for Zika cases. Guillain-Barre, a rare neurological disorder in which the immune system attacks the nervous system, is usually quite rare, so the heightened number of cases also evidenced the greater number of correlated Zika cases. The results showed that the underreporting was significant, with over 100 million cases having not been reported.

Determining the number of Zika cases is crucial for evaluating the risk of future outbreaks. It is believed that a single Zika infection immunizes a patient for life. Most of the studied areas experienced high enough infection rates that their degree of herd immunity will prevent a serious outbreak in the near future. However, as time goes on, the population will change as uninfected people are born and infected people pass away. Herd immunity will thus decrease over time, increasing the risk of another outbreak. The great extent of underreporting, coupled with the possibility of future spread of the virus, thus shows a need for better surveillance systems and general epidemiological preparedness. Expressing this concern, Dr. Moore states, "We probably want to really improve our surveillance for infection in the general population... hopefully that surveillance will allow us to implement effective control measures, whether it's spraying for the mosquito, or, at the very least, educational campaigns so that people know that there's a risk and they can take personal protection."

Co-authors of this study included Dr. Rachel J. Oidtman, Dr. Amir S. Siraj, Dr. K. James Soda, and Dr. Alex Perkins, researchers at the University of Notre Dame, in addition to Dr. Moore. Since working on this study, Dr. Moore has engaged in research regarding the challenges for spatial analyses of vector-borne diseases. ■

Rhythmic, Diurnal Behavior of Sloths in Disturbed Forests of Northeastern Brazil

MICHAEL MARINO

Because of diet and habitat restrictions, sloths (*Bradypus*) have remarkably altered their behaviors and metabolism levels to spend up to 90% of each day resting. They have been shown to be cathemeral, meaning that they can be active during the day or night. Ambient air temperature, predation, competition, and conditions for food acquisition often determine when sloths of a certain area are active and occupied with certain activities, but deforestation and disturbance of sloths' habitats have thrown many of these factors into flux. Many studies have already observed sloth behavior to assess the impacts of human-caused factors such as the extinction of predators, the presence of feral dogs, human hunting at night, and the extinction of certain tree species from sloth habitats. Such studies have often found that sloths in disturbed habitats are primarily active during the day, or diurnal, but significant variation in experiments' locations, types of human disturbance, and even experimental methods complicate any conclusions attempting to explain what parts of habitat disturbance might

cause sloths to become primarily diurnal and why. As pristine forests become increasingly rare in Central and South America where sloths live, it becomes increasingly important to know human development's effects on forest ecosystems, especially such a significant impact as changing an animal's very niche. Dominic Acri, former undergraduate researcher in Dr. Giles Duffield's biology lab in the Department of Biological Sciences at the University of Notre Dame, found his "niche" researching this exact question and others like it.

After hearing Dr. Duffield give a lecture about his lab's work, which focuses on the molecular basis of circadian rhythms in vertebrates and invertebrates, Acri discovered his own interest in the biological clock and quickly began working with Dr. Duffield during his freshman year. Acri worked in the Duffield Lab through most academic semesters and one summer and spent a summer at each of Notre Dame's environmental research centers UNDERC East and West. He further realized his interest in behavioral and neurological data by

working on studies of the rhythmic behavior of mosquitoes in the Duffield Lab and deer mouse behavior, including seasonal rhythms, at the UNDERC sites.

In Acri's senior year, Dr. Duffield invited Acri to work with him and collaborators in northeastern Brazil on a study of circadian rhythms in sloth behavior. For a total of 29 days over a five- to six-month period, collaborators recorded observations of 3 adult brown-throated three-toed sloths (*B. variegatus*)—2 females and 1 male—once every 15 minutes of the 24-hour day. During the study, both adult females birthed infants, and the behavior of each infant was also recorded every 15 minutes. Sloth activity was classified as resting, moving (without changing location), traveling, eating, or autogrooming, and the time of day for each observation was also recorded. While, on average, these observations revealed that only 60% of resting took place during night hours, 78% of traveling, 87% of moving, 94% of grooming, and 95% of eating took place during daylight hours. Night hours almost exclusively were spent resting, and no sloth was ever active from 10:00 p.m. to 1:00 a.m. X² periodogram and Fast Fourier Transformation analyses were applied to data to test how well the graphs of observations over time fit into sinusoidal curves and curves with additional harmonics representing different forms of circadian (24-hour) and ultradian (less than 24-hour) rhythmicity. These analyses showed strong circadian rhythmicity with diurnal activity and additionally found that daytime activity generally peaked in frequency twice per day, once in the morning and

once in the afternoon.

What caused such consistently diurnal behavior? With over 50% of tree species extinct from the study's forest and over 98% of the original forest's area deforested by humans, these sloths' habitats are highly disturbed. Developed areas and roadways divide the forest into irregularly shaped segments, and this may benefit sloths by decreasing intra-specific competition and creating more forest borders where *Cecropia* trees, a common sloth food source, often grow. With easier food access and less competition, sloths may be more likely to spend their active hours during the day when ambient temperatures are more comfortable. Further, the lack of natural predators during the day and the presence of feral dogs and human gunshots at night may encourage diurnal behavior and discourage nocturnal behavior, respectively.

With pristine forests becoming increasingly rare, such research illuminating humans' direct effects on forest ecosystems becomes increasingly important for natural resource management policy and ecological understanding. As an undergraduate researcher on this and similar studies, Acri fostered his passion for neuroscience and generally learned to love the collaborative learning and achieving of science. He encourages undergrads interested in research to "be involved with a research lab early and often" to develop their interests and experience. Acri is continuing his scientific career as a third-year Ph.D. candidate in medical neuroscience at the Indiana University School of Medicine. ■

Using the Arctic Tussock to Study Carbon Cycling on Alaska's North Slope

MICHAEL MARINO

Arctic tundra—a type of cold, treeless, northern ecosystem—is home to one of the most important processes affecting climate change worldwide: the melting of permafrost. Permafrost is soil that typically stays frozen year-round and underlays vast areas of arctic tundra. When arctic plants die, their biomass accumulates in the frozen ground and leaves stores of carbon which, over time, have built up a collection of underground carbon twice as great as the amount of carbon in the atmosphere. When this frozen ground melts in response to climate change, microbes digest the carbon and release carbon dioxide into the atmosphere, leading to increased temperatures which can contribute to further permafrost melting. Other effects of climate change on vegetation further complicate these trends.

Because biological processes affect carbon storage in tundra, and climate change will continue to impact plant population dynamics in arctic ecosystems, human knowledge about arctic plants and their changing ecological roles will be crucial for understanding climate change. Ecosystem models already allow scientists to predict carbon and energy flows into and out of arctic tundra ecosystems, but many treat tundra as homogeneous, ignoring changes in plant population dynamics

across geographic space. Many current models fail to explicitly consider how shifts in arctic vegetation will influence carbon cycling and respond to climate change. Salvatore Curasi, a graduate researcher in Dr. Adrian Rocha's ecology lab at the University of Notre Dame, is working to change that.

The Rocha Lab studies ecosystems across a wide variety of spatial and temporal scales and has focused its attention on the arctic tundra on Alaska's North Slope. Curasi has spent much of the past six years studying tussocks, a type of plant which creates mounds of soil, roots, and leaves as it grows and is a foundational species in arctic tundra ecosystems. Curasi has observed regional variations within tussock species, dissected and measured the physiological characteristics of the tussock growth form, and surveyed tussocks' role in arctic ecosystems at large scales. His work aims to use the tussock to better understand foundational species' important roles driving ecosystem function and carbon cycling. This understanding is especially important in the face of recent observations that certain plants accustomed to warmer climates are invading arctic vegetation communities and threatening tussock populations.



An artist's rendition of an *Eriophorum vaginatum* tussock based on Curasi's observations

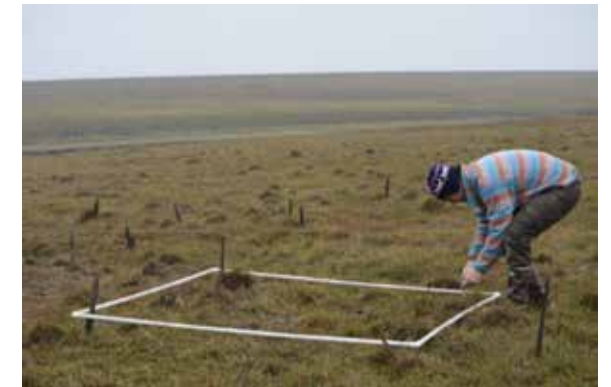
At the species level, the Rocha Lab has already shown that tussocks display significant ecotypic differentiation, a characteristic in which plants of the same species from different regions express different phenotypic characteristics. This was shown by moving each variant of a species into other variants' "home" regions and comparing the plants' fitness levels in the different regions. This experiment explored the relationship between ecotypic differentiation and plant fitness. The study suggests that ecotypic differentiation will also influence the responses of arctic ecosystems' gas fluxes to climate change.

At the wider level of the tussock growth form, Curasi has carefully dissected tussocks and done extensive fieldwork, both to collect his own data and to facilitate future studies attempting to measure belowground plant growth. Dissecting these plants allowed Curasi to quantify the relationship between simple field measurements such as a tussock's diameter and elusive mass and belowground carbon content. This work cleared the way for Curasi and others' future tussock studies; instead of uprooting tussocks to measure their mass values, field researchers can simply measure diameters and use preexisting equations to estimate mass. Curasi explains that belowground carbon "isn't fully represented in people's current understanding of these ecosystems, in part because it's very hard to survey and understand these belowground carbon pools, just from a technical perspective." Curasi's pioneering work advances tussock studies and empowers others to more accurately estimate belowground carbon stocks.

At the ecosystem level, data from Curasi and the Rocha Lab find greater meaning when used to enhance vegetation models. They have conducted transect surveys at nearly 100 arctic locations taking measurements including plant popu-

lation sizes and soil carbon stocks. These measurements are used to train vegetation models, some of which use machine learning methods. Such field measurements also can inform larger models created to predict the arctic tundra's impact on global climate change.

Curasi explains the goals of the lab, saying, "Hopefully our work will influence the way people model arctic ecosystems and think about how species influence flows of carbon within these ecosystems." With both quantitative results and the creative advancement of research methods, Curasi and the Rocha Lab are changing the way people understand arctic tundra and finding new motivation and meaning each step of the way. ■



Curasi using a quadrat on Alaska's North Slope to collect ecological data.



Curasi and a team of undergrads at the Toolik Field Station on Alaska's North Slope where the Rocha Lab headquarters its tundra research.

Creating a Process for Optimizing Antibacterial Peptides

STEPHANIE SWEGLE

As the most abundant domain of life forms on Earth, bacteria have evolved complex defense mechanisms to facilitate their survival amongst bacteria of similar size and makeup.

In their fight for survival, bacteria have developed small, ribosomally produced peptides called bacteriocins to kill competing bacteria. These bacteriocins have strong antibacterial prop-

erties that scientists are currently studying. At the University of Notre Dame, the Lee Lab is attempting to harness the power of bacteriocins in order to create a rapid and effective way to build antibacterial peptides. Dr. Shaun Lee, along with Jessica Ross, Francisco Fields, and a team of students at Notre Dame, has developed a methodology for building upon a key section of bacteriocins to create organized libraries of peptide variations. The peptides in this library can then be quickly evaluated in order to find optimized antibacterials. Their research aims to develop new, more effective antibiotics rapidly. According to Dr. Lee, the scientific world “[has] not explored the peptide space in terms of antibiotics that much.” He is hopeful they will play a major role in solving a variety of issues from antibiotic resistance to agricultural pollution and even novel pandemics.

The team theorized that a minimal peptide domain inside of bacteriocins is mainly responsible for their antibacterial properties. Their strategy was to build upon these minimized peptide sequences in order to create more easily synthesized peptide chains with improved antibacterial properties. To do this, the Lee Lab started with enterocin AS-48; they identified that cationic helices four and five were responsible for the bacteriocins’ ability to attract and penetrate bacterial membranes. Once they knew the sequence of 25 amino acids responsible for the antibacterial properties, they found homologous regions in other bacteria. Three other bacterial strains they tested had homologous regions to that of enterocin AS-48. Each of these four bacterial strains: *Enterococcus* sp. (containing enterocin AS-48), *Clostridium Sordellii*, *Bacillus xiamenensis* and *Paenibacillus* larvae became the starting point or “parent” from which they tested modifications to the peptide sequences. These modifications were made with the goals of minimizing the length of the peptide string while optimizing their antibacterial properties. To modify these peptides, the researchers systematically substituted alternate amino acids, specifically lysine and tryptophan, in specific locations. Since lysine has a positive charge, it was added with the aim of attracting negatively charged bacterial membranes. Due to tryptophan’s hydrophobic residues, the addition of this amino acid was meant to improve the peptide’s ability to penetrate bacterial membranes. In addition to these modifications, the researchers flipped certain amino acids. After all the modifications and substitutions were made, the team synthesized four peptide libraries, each containing the minimized parent peptide sequence plus 95 variations of that parent’s amino acid sequence.

After developing these libraries, the next step was to see if any of the modifications to the parent strand had improved the antibacterial effectiveness of the peptides. To do this, the peptide sequences were tested against a mix of gram negative and gram positive bacteria: *Escherichia coli*, *Streptococcus pyogenes*, *Pseudomonas aeruginosa* and *Staphylococcus aureus*. The team was able to determine which peptides were optimal based on minimal inhibitory concentration (MIC) values. MIC values measure how much of each peptide it would take to kill a certain amount of bacteria; the lower the MIC value, the more effective the peptide. Using green fluorescent protein (GFP)-expressing *E. coli*, the team tested how well

different peptide variations penetrated bacterial membranes. GFP leakage indicated which peptides caused a loss of bacterial membrane integrity. They also tested the cytotoxicity and hemolytic activity of the peptides in order to make sure that these peptides would not harm human cells. After conducting these tests, the researchers ranked the peptides in terms of improved antibacterial properties versus their parent and found eight optimized peptides: four narrow-spectrum peptides and four broad-spectrum peptides. These optimized peptides had surprisingly low eukaryotic cytotoxicity and hemolytic rates.

Dr. Lee believes that “there are really some exciting potential applications of using peptides” to improve human health. With the alarming pace that bacteria can become resistant to antibiotics, antibacterial peptides could be an important tool. Researchers can follow the replicable system that the Lee Lab has created to test variants of other bacteriocin peptides. By following this systematic design and evaluation process, researchers can efficiently create optimized antibacterials. This system could offer new options for doctors and patients fighting life-threatening infections, like recurrent *C. difficile*. Since this system produces hundreds of new antibacterials that can be tested quickly, it could help provide replacement antibiotics for fighting strains of bacteria that have become resistant.

These antibacterial peptides could also be used for cleaning medical devices, like catheters and colonoscopy instruments. Dr. Lee notes that antibacterial peptides could potentially be loaded into nanoparticles and coated on medical devices or even bandaids. This coating could prevent bacterial contamination while not harming the human cells that they come in contact with.

One of the more topical potential applications for the Lee Lab’s research is fighting viruses and even novel pandemics. Dr. Lee says that “the idea that these peptides can penetrate lipid membranes... could make them potentially very efficacious against [some] viruses.” Since viruses such as the coronavirus, HIV, and influenza all have a lipid outer layer, it may be possible to use peptides to fight them. One way to use these peptides against viruses may be to spray them onto surfaces to prevent transmission. Dr. Lee believes a promising antiviral application could be inserting a bacteriocin with a high affinity for particular viral membranes into a commensal (beneficial bacteria). This could enable people to fight off viruses like norovirus, for example, while leaving the patient’s cells and microbiome bacteria intact.

A seemingly unrelated current issue is the amount of toxic and environmentally harmful chemicals that are being used in farming to kill bacteria on crops. Dr. Lee points out the advantage to using antibacterial peptides versus chemicals is that “peptides are generally recognized as safe to eat because when you swallow them they get degraded,” so they would not pose a threat to human health. In addition, by using these peptides instead of chemical sprays, we could protect the environment from polluted water runoff. The applications for this research seem incredibly diverse and it will be exciting to see how the scientific community uses this new and powerful information. ■

Endoscopic Submucosal Dissection vs. Endoscopic Mucosal Resection for the Treatment of Colorectal Lesions: A Meta-Analysis

Christian Oakley

University of Notre Dame, Department of Physics

Abstract

There is no current consensus for the optimal endoscopic method for the treatment of colorectal lesions. We aimed to compare the efficacy and safety of endoscopic submucosal dissection (ESD) and endoscopic mucosal resection (EMR). Following a systematic literature search via Ovid Medline in December 2019, studies comparing EMR and ESD for the treatment of colorectal lesions were pooled in a meta-analysis performed using the generic inverse variance model. The primary outcome was the en bloc resection rate. Secondary outcomes were procedure time, hospital length of stay, additional operations, positive margin involvement, negative margin involvement, and vertical margin involvement. Sixteen studies with 4,536 patients were included. ESD was associated with a significantly higher en bloc resection rate as compared to EMR (RD, 0.27; 95% CI, 0.16–0.38; $p < 0.001$). Compared to EMR, ESD had a significantly longer procedure time (SMD, 1.23; 95% CI, 0.940–1.520; $p < 0.001$) and hospital length of stay (SMD, 1.23; 95% CI, 0.68–1.78; $p < 0.001$). There was no statistical difference for the rate of additional operations between ESD and EMR (RD, 0.01; 95% CI = -0.027–0.041; $p = 0.70$). Compared to EMR, ESD was associated with a significantly lower rate of positive margin involvement (OR, 0.44; 95% CI, 0.23–0.86, $p = 0.02$). At multivariate meta-regression, rectal lesions were associated with a higher en bloc resection rate as compared to colonic lesions (beta = -0.005, $p < 0.01$). Overall, despite longer procedure times and hospital length of stays, ESD had a higher en bloc resection rate than EMR for colorectal lesions. Randomized controlled trials are needed to determine the long-term outcomes of ESD and EMR in patients with colorectal lesions.

Introduction

Early colorectal cancer lesions can be treated surgically or endoscopically. Endoscopic treatments comprise endoscopic mucosal resection (EMR), which involves submucosal injection and transection of tissue with a snare, and endoscopic submucosal dissection (ESD), which involves submucosal injection and circumferential incision with a bipolar needle knife (1,2). Current guidelines recommend en bloc resection of early colorectal lesions, regardless of tumor size (1,3). Compared with piecemeal resection, en bloc resection is associated with improved histological evaluation, better assessment of vertical deep and lateral resection margins, and lower local recurrence

(4,5).

Previous systematic reviews and meta-analyses comparing ESD and EMR for colorectal lesions have been limited to specific surgical approaches (ESD or EMR), macroscopic lesion types (flat, depressed, or laterally spreading), tumor sizes (≥ 20 mm), or poor study selection (unpublished conference abstracts or retrospective studies limited to only ESD or EMR) (6,7,8). An inclusive contemporary analysis of en bloc resection rates in patients undergoing endoscopic treatment for colorectal lesions and the factors associated with en bloc resection rates has not been performed.

In this meta-analysis, we evaluate ESD and EMR for the treatment of colorectal lesions in terms of en bloc resection, procedure time, additional operations, and margin involvement.

Materials and Methods

Search Strategy

A comprehensive search was performed by a medical librarian to identify randomized controlled trials (RCTs) and observational studies comparing ESD and EMR. Searches were conducted on December 22, 2019, in the following databases: Ovid MEDLINE (ALL; 1946 to December 20, 2019) and Ovid EMBASE (1974 to December 20, 2019). The search strategy included the terms “endoscopic,” “submucosal dissection,” “mucosal resection,” “colorectal,” and “cancer.” The full search strategy is available in Supplementary Table 1.

Study Selection and Data Extraction

Searches across the chosen databases retrieved 1,626 results. After results were deduplicated, two independent reviewers (C.O. and A.A.) screened a total of 1,297 citations. Discrepancies were resolved by the senior author (I.H.). Titles and abstracts were reviewed against predefined inclusion/exclusion criteria. Articles were included if they were in English and were either randomized controlled trials (RCTs) or adjusted or matched observational studies comparing EMR and ESD for treatment of colorectal lesions. Animal studies, case reports, conference abstracts/presentations, editorials, expert opinions, studies not defining the number of patients per endoscopic treatment, and studies not defining or reporting outcomes of interest were excluded.

Full text was pulled for selected studies for a second round of eligibility screening. Reference lists of articles selected for inclusion were scanned for relevant articles to identify other studies. The full preferred reporting items for systematic reviews and meta-analysis (PRISMA) flow diagram outlining the study selection process is available in Supplementary Figure 1. All studies were reviewed by two independent investigators (C.O. and A.A.) and disagreements were resolved by the senior author (I.H.). For overlapping studies, the largest series was included.

Two investigators (C.O. and A.A.) performed data extraction independently, and the extracted data were verified by a third investigator (I.H.) for accuracy. The following variables were included: study data (sample size, publication year, design, institution, and country) (Table 1), patient demographics and preprocedural lesion characteristics (age, sex, smoking his-

tory, previous alcohol consumption, use of aspirin or NSAIDS, endoscopically measured mean tumor size, overall tumor location [proximal colon, distal colon, or rectum], rectal lesion location [lower, middle, or upper], colonic lesion location [ileocecal junction, cecum, ascending colon, transverse colon, descending colon, or sigmoid colon], macroscopic appearance [protruding, non-granular laterally spreading, granular laterally spreading, flat or depressed, or recurrent], adenocarcinoma depth [mucosal, submucosal (<1000 mm), or supramucosal (>1000 mm)], and adenoma subtype [low or high grade dysplasia] (Supplementary Table 2), and procedural and postprocedural factors (endoscopic treatment, mean procedure time, en bloc resection, histologically complete resection, additional operations, lymphovascular invasion, immediate bleeding, delayed bleeding, perforation, histologically demonstrated local recurrence, and follow-up period).

The quality of the included studies was assessed using the Newcastle-Ottawa Scale for observational studies (Supplementary Table 3). Only high-quality studies, defined as those achieving seven or more total stars, were included in this review.

Outcomes and Statistical Analysis

The primary outcome was the en bloc resection rate. Secondary outcomes were 1) procedure time; 2) hospital length of stay; 3) additional operations; 4) negative margin involvement; 5) positive margin involvement; 6) vertical margin involvement.

Odds ratios (ORs) with standard error were calculated and aggregated on the log scale. Individual and pooled OR with 95% confidence intervals (CI) were calculated by means of the DerSimonian Laird (inverse variance) method. Risk difference (RD) was used as a summary estimate in the case of zero event summaries. Standardized mean difference (SMD) was used when outcomes were reported in terms of continuous measurement. Hypothesis testing for statistical homogeneity was set at the two-tailed 0.10 level and was based on the Cochran Q test. Heterogeneity was reported as mild (I2 = 0%–25%), moderate (I2 = 26%–50%), or severe (I2>50%). The random effects model was used for all outcomes. Funnel plots and Egger’s regression test were used to assess publication bias. Leave-one-out sensitivity analysis was performed for the primary outcome. EMR was the reference for pairwise comparisons.

Multivariate meta-regression was used to explore the effects of annual hospital volume, total hospital volume during the study period, study period, continent (Europe vs. Asia), mean tumor size, rectal lesions, proximal colon lesions, and cecal lesions on the risk difference of the primary outcome. Statistical analyses were performed using “meta” and “metafor” packages in R (version 3.3.3 R Project for Statistical Computing) within RStudio (0.99.489, <http://www.rstudio.com>) and Meta-DiSc software (version 1.4).

Results

Study and Patients Characteristics

A total of 1,630 studies were retrieved of which 16 studies with 4,536 patients met the inclusion criteria (Table 1).

Two were prospective observational studies and 14 were retrospective observational studies. Seven originated from Japan, 6 from the Republic of Korea, 2 from China, and 1 from France. The number of patients in the individual studies ranged from 11 to 1,845. Of the 4,536 patients, 2,061 (45.4%) underwent ESD and 2,475 (54.6%) EMR. The mean age ranged from 47.2–69.3 and 38.3–68.1 years for ESD and EMR, respectively (Supplementary Table 2). Males ranged from 45.7%–89.1% and 25.0%–79.3% for ESD and EMR, respectively. The assessment of the quality of individual studies is reported in Supplementary Table 3.

Primary Outcomes

ESD was associated with a significantly higher en bloc resection rate as compared to EMR (RD, 0.27; 95% CI, 0.16–0.38; p <0.001) (Fig. 1).

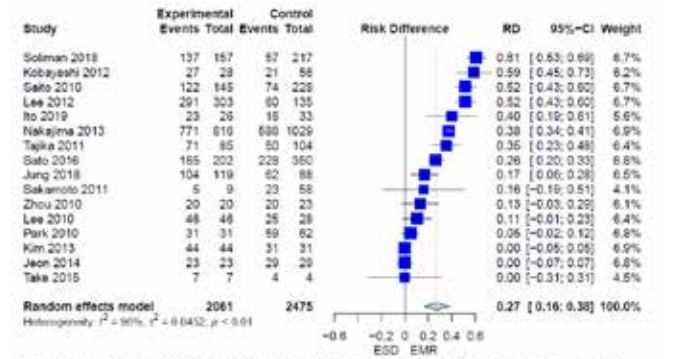


Figure 1: Forest plot of en bloc resection for endoscopic submucosal dissection (ESD) versus endoscopic mucosal resection (EMR).

Secondary Outcomes

There was no statistical difference in additional operation rates between ESD and EMR (RD, 0.01; 95% CI = -0.027–0.041; p=0.70) (Fig. 2). Compared to EMR, ESD had a significantly longer procedure time (SMD, 1.23; 95% CI, 0.940–1.520; p <0.001) and hospital length of stay (SMD, 1.23; 95%CI, 0.68–1.78; p<0.001) (Table 2). Compared to EMR, ESD was associated with a significantly lower rate of positive margin involvement (OR, 0.44; 95% CI, 0.23–0.86, p=0.02) (Table 2). There were no differences in negative margin involvement (OR, 2.57; 95% CI, 0.57–11.66; p = 0.22) and vertical margin involvement (OR, 4.12; 95% CI, 0.81–20.81; p= 0.09) between ESD and EMR (Table 2). The detailed results are reported in Supplementary Figures 2–4.

Multivariate Meta-Regression

On meta-regression, rectal lesions were associated with a lower en bloc resection rate (beta=-0.005, p <0.01) (Table 3). There was no association between the other patient- and procedure-related variables and the primary outcome.

Discussion

This is the largest pairwise meta-analysis comparing ESD and EMR for colorectal lesions and the first to evaluate lateral and vertical margin involvement for colorectal lesions between ESD and EMR. We found ESD to be associated with increased en bloc resection rate as compared to EMR.

Our analysis is also the first to explore the association between patient- and procedure-related variables and en bloc resection rates in ESD vs. EMR. At multivariable meta-regression, rectal lesions were associated with a higher en bloc resection rate as compared to colonic lesions. Previous meta-analyses comparing ESD versus EMR have been limited in their inclusion of patients. In 2016, Zhang et al. pooled data from 12 studies (2,929 lesions) undergoing ESD or EMR for the treatment of colorectal tumors (9). They found that ESD had a higher en bloc resection rate than EMR for tumors greater than 20 mm (OR: 9.62, 95% CI: 4.42–20.95), but that the rate did not reach statistical significance for tumors smaller than 20 mm (OR: 2.16, 95% CI: 0.61–7.58). Notably, the authors did not list or cite included studies in their analysis. Arrezo et al. pooled data from 11 studies and 4,678 patients undergoing endoscopic treatment of large colorectal lesions (>20 mm) between 1995–2012 (6). Consistent with our results, they found that ESD had a higher en bloc resection rate than EMR (RR: 1.93, 95% CI: 1.46–2.54). However, their meta-analysis included more unpublished conference abstracts than full-text articles and examined only large, noninvasive colorectal lesions. In another meta-analysis of 6 studies (1,642 lesions), Wang et al. found ESD to have higher en bloc resection rate than EMR (OR: 7.94, 95% CI: 3.96–15.91) (7).

As compared to piecemeal resection, en bloc resection facilitates improved pathological diagnosis and is independently associated with lower local recurrence rates (10,11). Local recurrence and additional surgery for colorectal lesions can prolong hospital stay, increase medical fees, and reduce post-operative patient quality of life (12,13). Additionally, lesions removed by ESD were larger than those removed by EMR. Although tumor size is associated with greater incomplete resection rates, ESD still had a higher en bloc resection rate than EMR (14). Further, we found that ESD had a lower rate of lateral margin involvement as compared to EMR (OR, 0.44; 95% CI, 0.23–0.86, p=0.02). Thus, for patients with favorable colorectal anatomy and no contraindications for colorectal endoscopic treatment, ESD may provide superior outcomes to EMR.

Notably, procedure times and hospital length of stay were longer in patients undergoing ESD as compared to EMR. For patients with poor cardiopulmonary status or advanced age, longer procedures may cause higher risks of complications. Thus, colorectal surgeons should consider patient status and tumor lesions characteristics when selecting the appropriate procedure for colorectal lesions.

Our study has limitations inherent from the use of retrospective observational studies in meta-analysis. The included studies were heterogeneous in terms of lesion location, operative detail, surgeon experience, and outcome definitions, which may limit the applicability of our findings to individual settings. The low to moderate heterogeneity across the studies,

however, suggests that the importance of these potential biases in our analysis was probably low. The use of meta-analysis cannot account for the presence of unmeasured confounders and treatment allocation bias. Additionally, differences in operator experience between studies cannot be accounted for using the meta-analytic approach. Nevertheless, this analysis represents the highest level of evidence since there are currently no randomized clinical trials examining ESD versus EMR for the treatment of early colorectal tumors.

Despite greater procedure times, ESD has a higher en bloc resection rate compared to EMR. Larger studies and randomized controlled trials are needed to determine the long-term clinical outcomes of ESD and EMR in patients with colorectal lesions.

Author	Study Period	Hospital	Country	Total	ESD	EMR	Type of Study
Ito/2019, (15)	2010-2016	Shizuoka Cancer Center	Japan	59	26	33	R
Jeon/2014, (16)	2007-2011	St. Mary's Hospital	South Korea	52	23	29	R
Jung/2018, (17)	2012-2013	Multicenter	South Korea	207	119	88	R
Kim/2013, (18)	2005-2011	Samsung Medical Center	South Korea	75	44	31	R
Kobayashi/2012, (19)	2005-2009	Tochigi Cancer Center	Japan	84	28	56	R
Lee/2010, (20)	2003-2009	Kyungpook National University Hospital	South Korea	74	46	28	R
Lee/2012, (21)	2004-2009	Dachang Hospital	South Korea	438	303	135	R
Nakajima/2013, (22)	2007-2010	Multicenter	Japan	1845	816	1029	P
Park/2010, (23)	2007-2009	Asan Medical Center	South Korea	93	31	62	P
Saito/2010, (24)	2003-2006	National Cancer Center Hospital	Japan	373	145	228	R
Sakamoto/2011, (25)	2004-2005	Multicenter	Japan	67	9	58	R
Sato/2016, (26)	2007-2012	Tokyo Medical University Hospital	Japan	552	202	350	R
Soliman/2018, (27)	2012-2016	Cochin Teaching Hospital	France	374	157	217	R
Tajika/2011, (28)	1995-2009	Aichi Cancer Center Hospital	Japan	189	85	104	R
Take/2015, (29)	2008-2015	Zhongshan Hospital of Fudan University	China	11	7	4	R
Zhou/2010, (30)	2004-2006	Zhongshan Hospital of Fudan University	China	43	20	23	R

EMR, endoscopic mucosal resection; ESD, endoscopic submucosal dissection; No., number; P, prospective; R, retrospective

Table 1. Summary of included studies.

Outcome	Studies	No. of patients	Effect estimate	95% CI	Heterogeneity	Test for overall effect
En bloc resection	16	4536	RD = 0.27	0.16-0.38	P = 0.00 I ² = 96.25%	P < 0.001
Procedure time	10	804	SMD = 1.23	0.94-1.52	P = 0.00, I ² = 65.47%	P < 0.001
Hospital LOS	2	63	SMD = 1.23	0.68-1.78	P = 0.83, I ² = 0.00%	P < 0.001
Additional operations	9	1245	RD = 0.01	-0.03-0.04	P = 0.26, I ² = 20.98%	P = 0.70
Negative lateral margin involvement	3	407	OR = 2.57	0.57-11.66	P = 0.00, I ² = 83.29%	P = 0.22
Lateral margin involvement	3	407	OR = 0.44	0.23-0.86	P = 0.62, I ² = 0.00%	P = 0.02
Vertical margin involvement	2	149	OR = 4.12	0.81-20.81	P = 0.17, I ² = 48.03%	P = 0.09

LOS, length of stay; OR, odds ratio; RD, risk difference (in case of equal events and total number of patients or zero events in both sides); SMD, standardized mean difference.

Table 2. Outcomes summary (significant results in bold).

Variable	Regression coefficient (Beta*) ± standard deviation, P-value
Annual hospital volume	0.0003± 0.0004, P= 0.42
Total hospital volume during study period	0.0002± 0.0001, P= 0.23
Study period	0.0041± 0.0307, P= 0.89
Continent (Europe vs Asia)	0.3627± 0.2108, P= 0.09
Mean tumor size [†]	0.0006± 0.0009, P= 0.48
Rectal lesions (vs colonic lesions)	-0.0051± 0.0018, P <0.01
Proximal colon lesions (vs distal colon lesions)	-0.0045± 0.0047, P= 0.33
Cecal lesions	-0.0248± 0.0167, P= 0.14

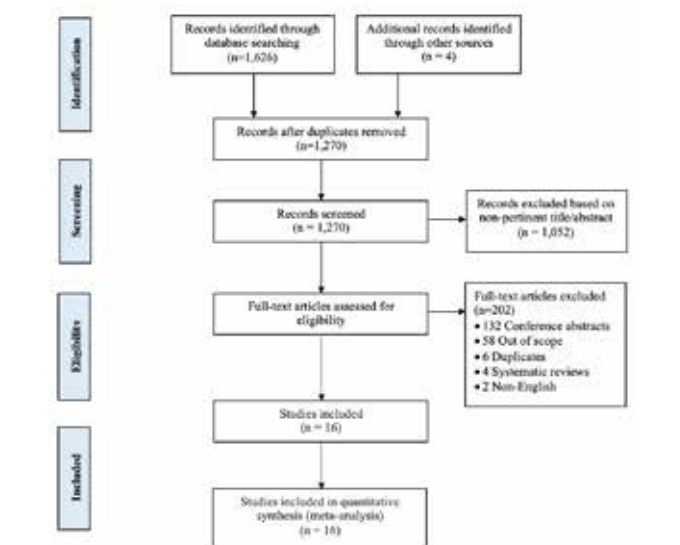
*Positive beta signifies higher MD with higher occurrence of the variable while negative beta signifies lower MD with higher occurrence of the variable
† Endoscopically measured

Table 3. Multivariate meta-regression for en bloc resection (significant results in bold).

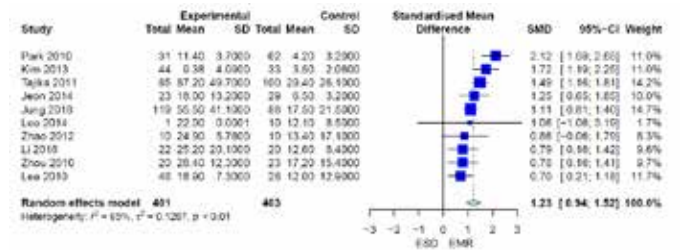
Confidentiality Statement

All figures, tables, and data have not been previously published. Our manuscript has not been previously published or submitted elsewhere for publication.

Appendix

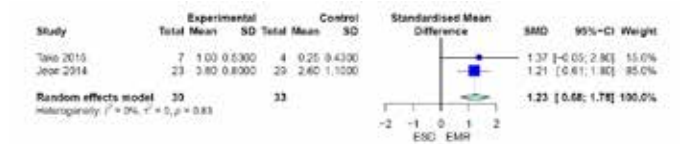


Supplementary Figure 1. Preferred Reporting Items for Systematic Reviews and Meta-Analysis (PRISMA) flowchart of our analysis.



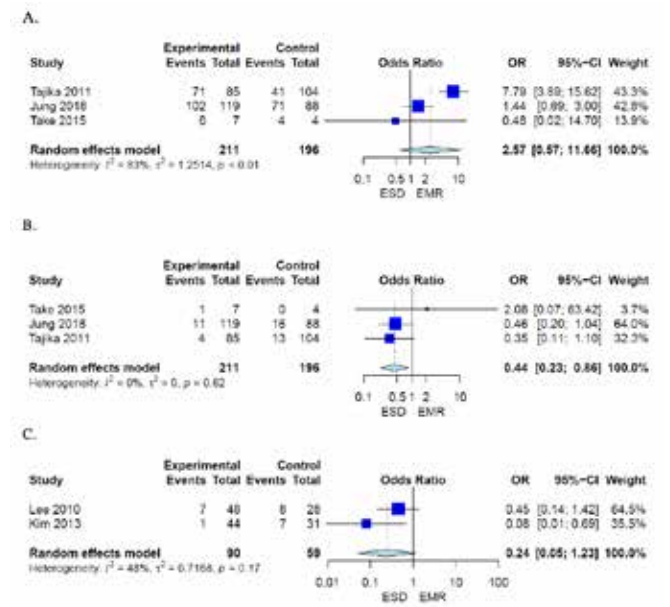
CI, confidence interval; SMD, standardized mean difference; SD, standard deviation. Standardized mean difference measures the effect size of outcomes between groups when included studies measure the same outcome through differently. Patients undergoing ESD had significantly longer procedure times than those undergoing EMR.

Supplementary Figure 2. Forest plot of procedure time for endoscopic submucosal dissection (ESD) versus endoscopic mucosal resection (EMR).



CI, confidence interval; SMD, standardized mean difference; SD, standard deviation. Patients undergoing ESD had significantly longer hospital lengths of stays as compared to those undergoing EMR.

Supplementary Figure 3. Forest plot of hospital length of stay for endoscopic submucosal dissection (ESD) versus endoscopic mucosal resection (EMR).



CI, confidence interval; OR, odds ratio. Odds ratio measures the ratio of the incidence rates of an event between the experimental and control groups. ESD and EMR were the experimental and control groups respectively. ESD was associated with a significantly lower incidence of positive margin involvement as compared to EMR. There were no differences in negative margin involvement and vertical margin involvement between ESD and EMR.

Supplementary Figure 4. Forest plots of margin involvement for endoscopic submucosal dissection (ESD) versus endoscopic mucosal resection (EMR). A) Negative margin involvement; B) Positive margin involvement; C) Vertical margin involvement.

Ovid MEDLINE(R) ALL (1946 to December 20, 2019)

Searched on December 22, 2019 (No date, language, or article type restrictions)

Line #	Search
1	(endoscopic or endoscopy or minimally invasive or minimal invasion).adj3.
2	((cancerous or cancer or benign or malignant or malignancy or metastasis or lump or neoplasm or adenoma growth or tumor or carcinoid) and (neuroendocrine or colorectal or rectum or rectal or colon or colic or coli or rectal or proctology or anal canal or anus or sphincter)).mp.
3	(mucosal resection or mucosal resection or mucous membrane resection or EMR).mp.
4	(submucosal dissection or submucosal dissections or submucosal dissect or ESD).mp.
5	3 and 4
6	1 and 5
7	2 and 6
8	Remove duplicates from 7

Supplementary Table 1. Full search strategy.

Year	Month	Day	Temperature		Humidity		Wind		Precipitation		Clouds		Sun		Moon		Stars		Planets	
			(°C)	(°F)	(%)	(%)	(km/h)	(mph)	(mm)	(in)	(%)	(%)	(h)	(h)	(h)	(h)	(h)	(h)	(h)	(h)
2019	Jan	01	10	50	60	70	80	90	100	110	120	130	140	150	160	170	180	190	200	
2019	Jan	02	11	52	61	71	81	91	101	111	121	131	141	151	161	171	181	191	201	
2019	Jan	03	12	54	62	72	82	92	102	112	122	132	142	152	162	172	182	192	202	
2019	Jan	04	13	56	64	74	84	94	104	114	124	134	144	154	164	174	184	194	204	
2019	Jan	05	14	58	66	76	86	96	106	116	126	136	146	156	166	176	186	196	206	
2019	Jan	06	15	60	68	78	88	98	108	118	128	138	148	158	168	178	188	198	208	
2019	Jan	07	16	62	70	80	90	100	110	120	130	140	150	160	170	180	190	200	210	
2019	Jan	08	17	64	72	82	92	102	112	122	132	142	152	162	172	182	192	202	212	
2019	Jan	09	18	66	74	84	94	104	114	124	134	144	154	164	174	184	194	204	214	
2019	Jan	10	19	68	76	86	96	106	116	126	136	146	156	166	176	186	196	206	216	
2019	Jan	11	20	70	78	88	98	108	118	128	138	148	158	168	178	188	198	208	218	
2019	Jan	12	21	72	80	90	100	110	120	130	140	150	160	170	180	190	200	210	219	
2019	Jan	13	22	74	82	92	102	112	122	132	142	152	162	172	182	192	202	212	220	
2019	Jan	14	23	76	84	94	104	114	124	134	144	154	164	174	184	194	204	214	221	
2019	Jan	15	24	78	86	96	106	116	126	136	146	156	166	176	186	196	206	216	222	
2019	Jan	16	25	80	88	98	108	118	128	138	148	158	168	178	188	198	208	218	223	
2019	Jan	17	26	82	90	100	110	120	130	140	150	160	170	180	190	200	210	219	224	
2019	Jan	18	27	84	92	102	112	122	132	142	152	162	172	182	192	202	212	220	225	
2019	Jan	19	28	86	94	104	114	124	134	144	154	164	174	184	194	204	214	222	226	
2019	Jan	20	29	88	96	106	116	126	136	146	156	166	176	186	196	206	216	224	227	
2019	Jan	21	30	90	98	108	118	128	138	148	158	168	178	188	198	208	218	226	228	
2019	Jan	22	31	92	100	110	120	130	140	150	160	170	180	190	200	210	220	228	229	
2019	Jan	23	32	94	102	112	122	132	142	152	162	172	182	192	202	212	222	229	230	
2019	Jan	24	33	96	104	114	124	134	144	154	164	174	184	194	204	214	224	230	231	
2019	Jan	25	34	98	106	116	126	136	146	156	166	176	186	196	206	216	226	231	232	
2019	Jan	26	35	100	108	118	128	138	148	158	168	178	188	198	208	218	228	232	233	
2019	Jan	27	36	102	110	120	130	140	150	160	170	180	190	200	210	220	230	233	234	
2019	Jan	28	37	104	112	122	132	142	152	162	172	182	192	202	212	222	232	234	235	
2019	Jan	29	38	106	114	124	134	144	154	164	174	184	194	204	214	224	234	235	236	
2019	Jan	30	39	108	116	126	136	146	156	166	176	186	196	206	216	226	236	236	237	
2019	Jan	31	40	110	118	128	138	148	158	168	178	188	198	208	218	228	238	237	238	
2019	Feb	01	41	112	120	130	140	150	160	170	180	190	200	210	220	230	238	238	239	
2019	Feb	02	42	114	122	132	142	152	162	172	182	192	202	212	222	232	239	239	240	
2019	Feb	03	43	116	124	134	144	154	164	174	184	194	204	214	224	234	239	240	241	
2019	Feb	04	44	118	126	136	146	156	166	176	186	196	206	216	226	236	240	241	242	
2019	Feb	05	45	120	128	138	148	158	168	178	188	198	208	218	228	238	241	242	243	
2019	Feb	06	46	122	130	140	150	160	170	180	190	200	210	220	230	240	242	243	244	
2019	Feb	07	47	124	132	142	152	162	172	182	192	202	212	222	232	242	243	244	245	
2019	Feb	08	48	126	134	144	154	164	174	184	194	204	214	224	234	244	244	245	246	
2019	Feb	09	49	128	136	146	156	166	176	186	196	206	216	226	236	244	245	246	247	
2019	Feb	10	50	130	138	148	158	168	178	188	198	208	218	228	238	245	246	247	248	
2019	Feb	11	51	132	140	150	160	170	180	190	200	210	220	230	240	245	247	248	249	
2019	Feb	12	52	134	142	152	162	172	182	192	202	212	222	232	242	246	248	249	250	
2019	Feb	13	53	136	144	154	164	174	184	194	204	214	224	234	244	247	249	250	251	
2019	Feb	14	54	138	146	156	166	176	186	196	206	216	226	236	246	248	250	251	252	
2019	Feb	15	55	140	148	158	168	178	188	198	208	218	228	238	248	249	251	252	253	
2019	Feb	16	56	142	150	160	170	180	190	200	210	220	230	240	249	251	252	253	254	
2019	Feb	17	57	144	152	162	172	182	192	202	212	222	232	242	250	252	253	254	255	
2019	Feb	18	58	146	154	164	174	184	194	204	214	224	234	244	251	253	254	255	256	
2019	Feb	19	59	148	156	166	176	186	196	206	216	226	236	246	252	254	255	256	257	
2019	Feb	20	60	150	158	168	178	188	198	208	218	228	238	248	253	255	256	257	258	
2019	Feb	21	61	152	160	170	180	190	200	210	220	230	240	250	254	256	257	258	259	
2019	Feb	22	62	154	162	172	182	192	202	212	222	232	242	251	255	257	258	259	260	
2019	Feb	23	63	156	164	174	184	194	204	214	224	234	244	252	256	258	259	260	261	
2019	Feb	24	64	158	166	176	186	196	206	216	226	236	246	253	257	259	260	261	262	
2019	Feb	25	65	160	168	178	188	198	208	218	228	238	248	254	258	260	261	262	263	
2019	Feb	26	66	162	170	180	190	200	210	220	230	240	250	255	259	261	262	263	264	
2019	Feb	27	67	164	172	182	192	202	212	222	232	242	251	256	260	262	263	264	265	
2019	Feb	28	68	166	174	184	194	204	214	224	234	244	252	257	261	263	264	265	266	
2019	Feb	29	69	168	176	186	196	206	216	226	236	246	253	258	262	264	265	266	267	
2019	Feb	30	70	170	178	188	198	208	218	228	238	248	254	259	263	265	266	267	268	
2019	Feb	31	71	172	180	190	200	210	220	230	240	250	255	260	264	266	267	268	269	
2019	Mar	01	72	174	182	192	202	212	222	232	242	251	256	261	265	267	268	269	270	
2019	Mar	02	73	176	184	194	204	214	224	234	244	252	257	262	266	268	269	270	271	
2019	Mar	03	74	178	186	196	206	216	226	236	246	253	258	263	267	269	270	271	272	
2019	Mar	04	75	180	188	198	208	218	228	238	248	254	259	264	268	270	271	272	273	
2019	Mar	05	76	182	190	200	210	220	230	240	250	255	260	265	269	271	272	273	274	
2019	Mar	06	77	184	192	202	212	222	232	242	252	256	261	266	270	272	273	274	275	
2019	Mar	07	78	186	194	204	214	224	234	244	254	258	263	268	272	274	275	276	276	
2019	Mar	08	79	188	196	206	216	226	236	246	256	260	265	270	274	276	277	278	277	
2019	Mar	09	80	190	198	208	218	228	238	248	258	262	267	272	276	278	279	280	278	
2019	Mar	10	81	192	200	210	220	230	240	250	260	264	269	274	278	280	281	282	279	
2019	Mar	11	82	194	202	212	222	232	242	252	262	266	271	276	280	282	283	284	280	
2019	Mar	12	83	196	204	214	224	234	244	254	264	268	273	278	282	284	285	286	281	
2019	Mar	13	84	198	206	216	226	236	246	256	266	270	275	280	284	286	287	288	282	
2019	Mar	14	85	200	208	218	228	238	248	258	268	272	277	282	286	288	289	290	2	

Lee D, Jeon S, Park S, Jung M, Cho C, Tak W, et al. The feasibility of endoscopic submucosal dissection for rectal carcinoid tumors: comparison with endoscopic mucosal resection. *Endoscopy*. 2010 Jul 28;42(08):647–51.

Lee E-J, Lee JB, Lee SH, Youk EG. Endoscopic treatment of large colorectal tumors: comparison of endoscopic mucosal resection, endoscopic mucosal resection–precutting, and endoscopic submucosal dissection. *Surg Endosc*. 2012 Aug;26(8):2220–30.

Nakajima T, Saito Y, Tanaka S, Iishi H, Kudo S, Ikematsu H, et al. Current status of endoscopic resection strategy for large, early colorectal neoplasia in Japan. *Surg Endosc*. 2013 Sep;27(9):3262–70.

Park H-W, Byeon J-S, Park YS, Yang D-H, Yoon SM, Kim K-J, et al. Endoscopic submucosal dissection for treatment of rectal carcinoid tumors. *Gastrointestinal Endoscopy*. 2010 Jul;72(1):143–9.

Saito Y, Fukuzawa M, Matsuda T, Fukunaga S, Sakamoto T, Uraoka T, et al. Clinical outcome of endoscopic submucosal dissection versus endoscopic mucosal resection of large colorectal tumors as determined by curative resection. *Surg Endosc*. 2010 Feb;24(2):343–52.

Sakamoto T, Saito Y, Matsuda T, Fukunaga S, Nakajima T, Fujii T. Treatment strategy for recurrent or residual colorectal tumors after endoscopic resection. *Surg Endosc*. 2011 Jan;25(1):255–60.

Sato T, Fukuzawa M, Gotoda T, Moriyasu F. Comparison of clinical outcomes between colorectal EMR and ESD. 2016;74(2):9.

Soliman H, Brieau B, Guillaumot M-A, Leblanc S, Barret M, Camus M, et al. Invasive pit pattern, macronodule and depression are predictive factors of submucosal invasion in colorectal laterally spreading tumours from a Western population. *United European Gastroenterology Journal*. 2018 Dec;6(10):1569–77.

Tajika M, Niwa Y, Bhatia V, Kondo S, Tanaka T, Mizuno N, et al. Comparison of endoscopic submucosal dissection and endoscopic mucosal resection for large colorectal tumors: *European Journal of Gastroenterology & Hepatology*. 2011 Nov;23(11):1042–9.

Take I. Endoscopic resection of colorectal granular cell tumors. *WJG*. 2015;21(48):13542.

Zhou P-H, Yao L-Q, Qin X-Y, Xu M-D, Zhong Y-S, Chen W-F, et al. Advantages of endoscopic submucosal dissection with needle-knife over endoscopic mucosal resection for small rectal carcinoid tumors: a retrospective study. *Surg Endosc*. 2010 Oct;24(10):2607–12.

About the Author

Christian Oakley is a senior at Notre Dame majoring in physics in medicine with a compassionate care in medicine minor. He is a member of the Sigma Pi Sigma Honor Society. His research was conducted at Weill Cornell Medicine/ New York-Presbyterian Hospital during a summer research internship. For the last two years, he has studied minimally invasive cardiothoracic surgery under Dr. Mario Gaudino and Dr. Irbaz Hameed at Weill Cornell Medicine. He has authored several peer-reviewed publications in high-impact journals, including the *International Journal of Surgery* and *The Journal of Thoracic and Cardiovascular Surgery*. After graduating from Notre Dame, Christian will be a clinical research fellow in adult reconstructive surgery at NYU Langone Orthopedic Hospital. Afterward, he hopes to attend medical school and become a sports medicine orthopedic surgeon.

Investigation of the Use of Camouflage in the Sally Lightfoot Crab (Grapsus grapsus)

Abigail A. White
University of Notre Dame, Department of Biological Sciences

Abstract

The sally lightfoot crab (*Grapsus grapsus*) is a tropical marine crab that inhabits the Galápagos Islands, as well as other tropical islands globally. These crabs start their lives a dark brown color and turn redder as they age until they reach a fully red adult stage. Much of the coastline of the Galápagos Islands, where the crabs live, is composed of dark basaltic rock or light sand. I investigated which color substrate the different color stages of crab prefer in order to evaluate whether the young crabs use their color as camouflage in defense against predators like the Galápagos lava heron. Since the dark juveniles blend in with the rock, I predicted that they would be more likely to be found on dark substrate than the more conspicuous red adults. However, I found that both crabs equally preferred dark substrates. Possible reasons for this preference, which include color, temperature, and texture differences between substrates, should be further explored in both observational and experimental studies. I also investigated the population structure of the crabs, finding far more young dark crabs than adult red crabs, as expected in an r-selected species. Overall, I advise population monitoring of the crabs and preservation of their preferred substrate of dark basaltic rocks on the shores of the Galápagos Islands.

Introduction

The sally lightfoot crab (*Grapsus grapsus*) inhabits the Galápagos Islands as well as many other tropical areas globally, including at least one freshwater habitat (Arai et al. 2017). Over their lives, they undergo a color transition from darker brown as juveniles to a striking red as adults (Freire et al. 2011). This color change is important in mating, as redder male crabs are more reproductively successful (Freire et al. 2011). These highly mobile crabs scurry away to avoid being preyed upon by birds and other predators, but the smaller juveniles may have a harder time getting away quickly and struggling free if captured (Rathbun 1918). Camouflage could help protect the juveniles from visual predators, such as a variety of birds and feral house cats (*Felis catus*) which prey upon the crabs (Miller 2013). In particular, the Galápagos lava heron (*Butorides striata sundevalli*) preys on sally lightfoot crabs as a primary food source (Kushlan 2009). Birds have good color vision, making camouflage a likely necessity to evade them (Tedore and Nilsson 2019). As such, the juveniles may utilize darker rocks, such as coastal basalt present on many Galápagos islands, as camouflage.

Sally lightfoot crabs perform important ecological

functions, eating carrion, bird droppings, bat guano, and algae (Miller 2013). These functions are desired by humans as they keep beaches clean. However, they also eat bird eggs, newly hatched blue-footed boobies, young sea turtles, other macroinvertebrates, and fish, which may be concerning from a conservation perspective if they deplete populations of rare animals (Miller 2013; Gianuca and Carolus 2007). An important effect of their algae consumption is that the sally lightfoot crabs control populations of erect forms of algae during El Niño years, affecting food availability for other algae-feeders such as fish and marine iguanas (Vinueza et al. 2006). Perhaps the most interesting item in these generalists’ diet is ticks that infest marine iguanas (*Amblyrhynchus cristatus*). This behavior suggests a mutualistic relationship between the crabs and iguanas as the iguanas are groomed, and the crabs are provided food (Miller 2013).

Sally lightfoot crabs reproduce throughout the year, without a defined breeding season (Miller 2013). As such, crabs spanning a range of colors from very dark to very red are present in the Galápagos year round. Crabs are an r-selected species, meaning they invest more in offspring quantity than in care for the individual offspring (Cassill 2019). Given the high reproductive rate and steep mortality rate for young individuals, I expected that there would be many more young, dark crabs than old, red crabs. I investigated population age structure of the crabs by comparing the relative abundance of darker and redder crabs. This study also provides a reference for relative abundance of ages of crabs, allowing future monitoring for changes in age structure. My study may therefore be useful for conservation efforts, especially in noting changes in recruitment related to environmental changes that are harder to detect.

Given the sally lightfoot crab’s important ecological role, it is important to understand their survival strategy in case the need may arise to manage crab population growth. These crabs are a relatively understudied group in the Galápagos. I investigated the use of camouflage by the sally lightfoot crab, in particular the use of dark rocks by darker-colored juveniles. I also investigated the age structure of the crabs based on their color. I hypothesized that darker crabs would be found on darker substrate for camouflage purposes, whereas red crabs would have no color substrate preference as they cannot blend in with any natural substrate in their environment. I also hypothesized that dark, younger crabs would be more abundant than redder adult crabs due to population age structure.

Methods and Materials

Data collection

During a week-long field trip to the Galápagos Islands, when I saw any sally lightfoot crab or group of crabs, I took a picture or pictures of the group using my phone camera. In some instances when crabs were too abundant or far away to photograph, they were counted in the field. Islands visited and sampled were Baltra, Santa Fe, Santa Cruz, South Plaza, Mosquera, North Seymour, Santiago, and Bartolomé.

Later, I analyzed the photos and categorized the crabs into four color types: fully red, mostly red, mostly dark, or fully dark. I also recorded what color substrate (light or dark) each crab was on. Dark substrate was basalt, and light substrate in-

cluded light concrete and basalt that was covered in light-colored bird droppings. Every possible observed crab was included to minimize bias, but some were too far away to be counted or were spotted during an activity that made it impossible for me to take photographs and therefore were not included. Dead crabs were also not included in the analysis.

Statistical Analysis

Once I recorded crab color and substrate color for each crab in the groups of crabs I photographed, I ran a chi-squared test to determine if crab color and substrate color were independent factors. I then ran a paired t-test to determine whether more crabs of any color were found on dark or light substrate on the islands. A paired t-test as opposed to an independent t-test was used to account for different islands (replicates) having different sizes of crab populations. Using color to represent age, I investigated the age structure of crabs on the islands by running a chi-squared test to evaluate if crabs were evenly distributed across color groups. Statistical analyses were run using R software.

Results

General Results

The total sample size was 247 crabs overall from the 8 islands. All crabs were found on the coastline of islands or on smaller islands near the coast of the main island studied. All crabs were found on hard substrate (either rock or concrete); crabs were never observed on sand or plants, regardless of color. Crabs were sometimes found hiding in cracks between rocks, or sheltered under overhanging rocks. Crabs of all colors across the range from very dark to very red were observed.

When crab color and substrate color were analyzed with a chi-squared test, the two factors were independent, meaning color groups of crabs did not exhibit significantly different preferences for substrate color ($X^2 = 1.8235$, $p = 0.6098$, Figure 1).

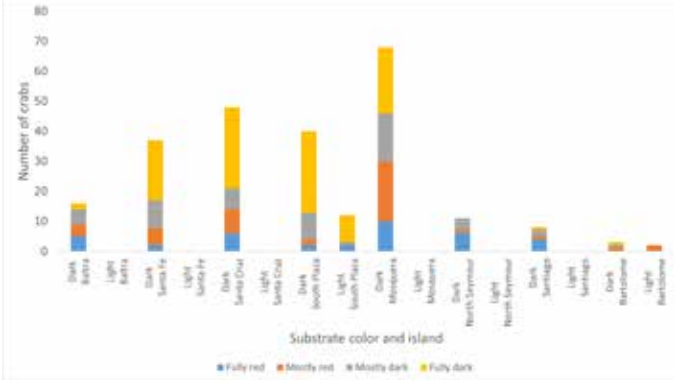


Figure 1: Number of crabs of each color on each island and substrate color. This stacked bar graph shows the number of crabs on the light and dark substrate of each island, broken down by crab color. The chi-squared test of substrate color and crab color indicated the two factors were independent ($X^2 = 1.8235$, $p = 0.6098$).

Substrate preference

A paired t-test revealed a significant difference between the number of crabs on light and dark substrate on each island ($p = 0.01199$). More than 16 times as many crabs were documented on dark substrate as on light substrate on the islands (Figure 2).

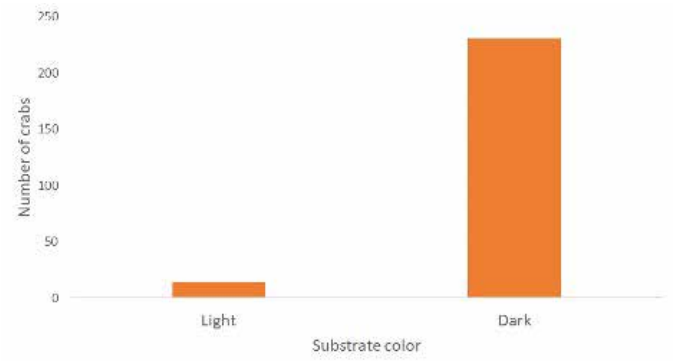


Figure 2: Number of crabs on each substrate color. This bar graph shows the total number of crabs on light and dark substrate across islands, regardless of crab color. A paired t-test indicated a significant difference between number of crabs on light and dark substrate ($p = 0.01199$). There were more than 16 times as many crabs on dark substrate as on light substrate on the islands.

Population structure

A chi-squared test evaluating the frequencies of each color of crab indicated that crabs were not evenly distributed among color groups ($p < 0.0001$). Dark crabs were more than twice as abundant as any of the other color groups (Figure 3).

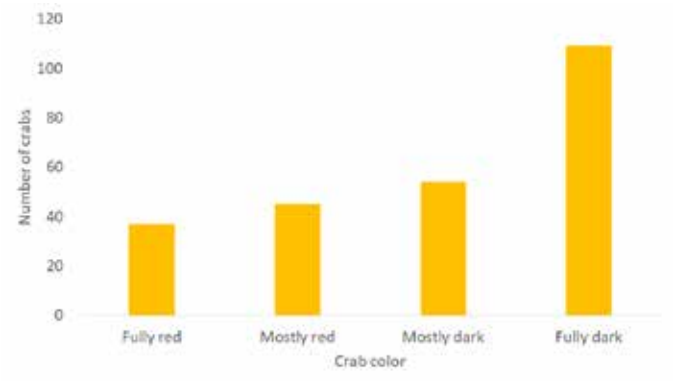


Figure 3: This bar graph shows the total number of crabs of each color across all islands. A chi-squared indicated the crabs are not evenly distributed among color groups, which here represent age groups ($p < 0.0001$). Crab population decreases with age.

Discussion

Overall, I found that substrate color preference of sally lightfoot crabs is not affected by crab color, as all colors of crab prefer dark substrate. This finding indicates that crabs do not show less preference for substrate color as they turn redder and more conspicuous as I hypothesized. However, the preferred color of substrate for dark crabs was dark, as predicted.

While the use of camouflage is a potential motivator for dark crabs preferring dark substrate, it does not explain the

older red crabs’ preference for dark rock. One explanation could be that the sally lightfoot crabs learn as juveniles to stay on the dark rock to avoid predation, and continue this behavior as they turn redder. Crustaceans have been observed to learn to avoid pain, so they could have learned from near-successful predation events to stay on darker substrates where they blend in (Elwood 2019). The behavior could also be genetic, meaning those crabs that instinctively avoid light substrate avoid predation as juveniles and are not at a disadvantage as adults, so dark substrate preference is selected for.

Other explanations besides camouflage include that dark rocks tend to be warmer, absorbing more solar radiation. This could be a motivator for crabs to bask on the rocks because crabs are ectothermic and must thermoregulate behaviorally, including by avoiding areas that are too cool or seeking warmer habitat (McGaw 2002). This choice would account for red crabs being equally motivated to congregate on dark substrates. In the future, we should measure the temperature on or above both substrate color types to determine if they are significantly different.

Another explanation is that there were far fewer light rocks than dark rocks. Though there was lighter substrate in the form of plants or soil inland on many islands, the coastline where crabs live was mainly comprised of dark rock and light sand. However, this does not explain why crabs were never found on light sand. The preference of the crabs for dark rock over light sand could either be due to color, in one of the ways described, or due to texture. Crabs may find it easier to scurry quickly across the hard rocks as opposed to the light sand. Another possibility is that a food resource was found on rocks and not sand, or that a predator or competitor was only found on sand and crabs spent time on rocks to avoid them.

This study would be improved by mapping the substrate colors on each island, because if crabs only have a choice of dark rock, then the fact that they are mostly found there is neither surprising nor indicative of crab behavior. While I observed that crabs had a choice of substrate colors, a quantitative survey of substrate types available would allow the proportion of substrate color to be compared to the proportion of crabs found on that substrate, giving a more precise evaluation of substrate preference. This behavior could be further investigated in a lab setting by presenting sally lightfoot crabs with a choice of substrates that vary in temperature but are the same color and seeing if they prefer one temperature or randomly disperse. This study would also improved if I conducted it over a longer timeframe and therefore got a larger sample size and accounted for seasonal or diel differences. It would also be benefited by traveling to other areas of the world where sally lightfoot crabs are present to observe separate populations of the crabs. This survey could help indicate whether the dark color preference was influenced by composition of island substrate, or whether they are usually found on dark substrate throughout their range.

This topic could be further investigated by using a more controlled, laboratory-based behavioral component wherein crabs would be presented with a choice of light or dark substrate as opposed to this purely observational study. In such a study, the factor motivating crab preference could be isolated by presenting crabs with different colors, textures, and tem-

peratures of substrate. As expected, I also found a much higher abundance of younger, dark crabs compared to older, red crabs. This observation reinforces the idea that the crabs are r-selected and depend on high numbers of offspring with low parental care. The age structure of the population may be even more skewed toward young, as they would be the most likely to be underrepresented in my counts due to small body size and inconspicuous color. If future studies find a significant change in this structure, especially seeing more red than dark crabs, this would be cause for concern as it would indicate low recruitment and a potential future population crash.

Although there are no active projects to conserve sally lightfoot crabs on the Galápagos, there may come a day when conservation becomes necessary. While crabs were clearly mostly found on dark substrate, a conclusion about the reason cannot be definitively reached with the available data. Further study investigating the motivation for substrate preference in crabs could help determine the mechanism at work and inform potential conservation efforts. I advise ensuring the availability of dark substrate on beaches where crab populations need encouragement and the monitoring of population structure to predict changes in population size.

Acknowledgments

Many thanks to the advisers of this trip, Dr. Gary Lamberti, Dr. Jeremy Fein, and Ms. Katherine O’Reilly. This study would not have been possible without Luis Rodriguez, our Galápagos National Park naturalist and guide. Thanks also to the Notre Dame Department of Biological Sciences and Department of Civil and Environmental Engineering and Earth Sciences for helping fund this trip. Thanks to Anthony Travel and Notre Dame International for helping organize travel and lodging during this expedition.

About the Author

Abigail White is a senior at Notre Dame majoring in environmental sciences with a minor in theology. She is a member of the Glynn Family Honors Program and on the Environmental Science Senior Leadership Committee. Her research was conducted in the Galápagos Islands as part of a course with Dr. Gary Lamberti. She has also conducted interdisciplinary research on the influence of human activity on stream and river ecosystems with Dr. Jennifer Tank, as well as in the Museum of Biodiversity on campus. After graduation, White intends to pursue a career in environmental education, likely at a natural history museum.

A Reproducible and Scalable Genome Assembly Pipeline for Sulfolobaceae

John Le

University of Notre Dame, College of Science:
Science-Business

Abstract

The members of the family *Sulfolobaceae* are one of the best-studied hyperthermophiles in the phylum Crenarchaeota due to their ability to be cultured and maintained in a laboratory. Currently, this family serves as an ideal model system to provide insights into the biochemical, structural, and genetic underpinnings of archaeal extremophiles. Additionally, these microbes serve as hosts to a suite of viruses including the *Sulfolobus* Spindle-shaped Virus (SSV). The SSV system is a popular model for studying virus-host interactions and the biology of thermophilic viruses. Recently, a comprehensive host-range study has brought to light new significant findings including: (1) SSV infection of *Sulfolobus* is independent of host and virus geography, and (2) SSV infection is independent of host species and extends beyond the genus *Sulfolobus*. However, the genetic underpinnings for these findings remain unknown. Six strains of *Sulfolobaceae* were selected for further analysis including two *Sulfolobus islandicus* strains (*S. islandicus* REN1H1 with plasmid and without plasmid), two *Sulphurisphaera* strains (*S. tokodaii* and *S. ohwakuensis*), and two unknown isolates from Kamchatka, Russia. Prior to any comparative analysis, the genomes of the six strains must be sequenced and assembled. Unfortunately, long read sequencing often produces data with an overall high error rate. Assembly pipelines have previously relied on additional error correction steps which can be time exhaustive and challenging as each step requires a specific set of tools and dependencies. Here, we address this need for a more efficient and adaptable workflow by providing an autonomous, reproducible, and scalable genome assembly pipeline for *Sulfolobaceae*.

Introduction

The study of *Sulfolobaceae* has played an integral role in investigating virus-host interactions in hyperthermophilic Archaea. In particular, the *Sulfolobus* Spindle-shaped Virus (SSV) system has emerged as an effective reduced model for studying virus-host biogeography and thermophilic archaeal virus biology (Ceballos et al. 2020). This system has risen in popularity for several reasons: (1) as a reduced model system, the *Sulfolobaceae* do not have a highly evolved immune system, making them ideal candidates in studying the fundamental properties of virus evolution (Brockhurst et al. 2007); (2) the high temperature and highly acidic environment of the *Sulfolobaceae* have low overall biodiversity limiting the potential for host switching (Munson-McGee et al. 2018); and (3)

because of their ability to be easily maintained under laboratory conditions, *Sulfolobaceae* and SSVs serve as a convenient model system to provide insight into the biochemical, structural, and genetic studies of Archaea and extremophiles in general (Ciaramella, Pisani and Rossi 2002).

Host: Sulfolobaceae

First described by Brock et al. in 1972, the family *Sulfolobaceae* include hyperthermophilic Archaea that grow optimally at temperatures between 70–85°C with a pH of 2–3 and have been isolated from various acidic thermal habitats around the world. The well-studied family *Sulfolobaceae* make up a branch of the kingdom Crenarchaeota. Previously, the genera of *Sulfolobaceae* only included *Acidianus*, *Metallosphaera*, *Stygiolobus*, *Sulfurococcus*, and *Sulfurisphaera*. However, two recent publications proposed the introduction of a new genus, *Saccharolobus*, and the reclassification of certain *Sulfolobus* species from analyses of newly discovered isolates and the re-examination of previously described species (Sakai and Kurosawa 2018; Tsuboi et al. 2018). The 16S rRNA phylogenetic tree highlighting the proposed genus and reclassifications are outlined in Figure 1. This includes the reclassification of *Sulfolobus tokodaii* to *Sulfurisphaera tokodaii*, *Sulfolobus acidocaldarius* to *Saccharolobus acidocaldarius*, and *Sulfolobus shibatae* to *Saccharolobus shibatae*, as well as the isolation of *Saccharolobus caldissimus* and *Sulfurisphaera javensis*.

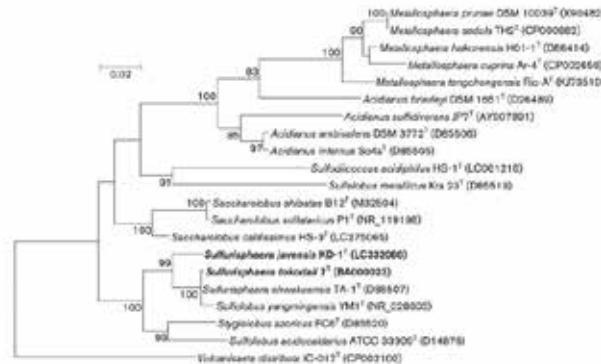


Figure 1: Maximum-likelihood phylogenetic tree based on 16S rRNA gene sequences including proposed genus and reclassifications. Bootstrap values derived from 1,000 samplings are shown at branch nodes. GenBank accession are given after the strain names. Bar, 0.02 substitutions per nucleotide position. (reproduced from Tsuboi et al. 2018)

Virus: Sulfolobus Spindle-Shaped Virus

The first member of this virus family, SSV1, was isolated from a *Saccharolobus shibatae* strain in Beppu, Japan (Palm et al. 1991). SSV virus production was shown to be induced by exposure to UV light or treatment with mitomycin C (Reiter et al. 1987; Schleper, Kubo and Zillig 1992). Studies have shown that the SSV genome varies in size from 14 to 17 kbp and resides in three forms: (1) a positively supercoiled virion; (2) an episomal genome in the host which includes positively supercoiled, negatively supercoiled, or relaxed double-stranded DNAs (Nadal et al. 1986); or (3) a provirus that is fully integrated into the host genome (Schleper, Kubo and Zillig 1992). SSVs have

long been reported to prefer a non-lytic “budding” replication strategy in *Sulfolobaceae* (Ceballos et al. 2012). However, it was recently suggested that SSV9 can induce cell dormancy and, ultimately, death in a sympatric host (Bautista, Zhang and Whitaker 2015). Moreover, two recent publications seek to expand the number of characterized genotypes by introducing additional SSV isolates (SSV19–22) as well as the observation of SSV-like remnants in *S. islandicus* genomes (Pauly et al. 2019; Zhang et al. 2020).

Sulfolobus Spindle-Shaped Virus System

Previously, a comprehensive host-virus study for the SSV system determined host ranges for six *bona fide* SSVs utilizing a set of 13 *Sulfolobaceae* (Table 1) (Ceballos et al. 2012). This study yielded several interesting findings, namely: (1) SSV infectivity and *Sulfolobus* susceptibility are independent of the geographical regions from where the hosts and viruses were isolated; and (2) SSV infection is independent of the host species and extend beyond the genus *Sulfolobus* (Ceballos et al. 2012).

For decades, SSV infection has also long been characterized as “non-lytic” as the double-stranded DNA viruses release virions via budding rather than host lysis. However, a recent study suggests SSV9 virion release results in a “lysis-from-within” phenomena where aggressive virus egress induces gross cell lysis in allopatric host but adaptation of the sympatric host supports typical SSV budding (Ceballos et al. 2020). While these new findings provide better insight into understanding of virus-host interactions in hyperthermophilic Archaea, their genetic underpinnings remain unknown. Therefore, six different strains including two *Sulfolobus* strains, two *Sulfurisphaera* strains, and two isolates were selected and split up into pairs based on phenotypic differences in susceptibility and virus-induced differences in growth that were of interest.

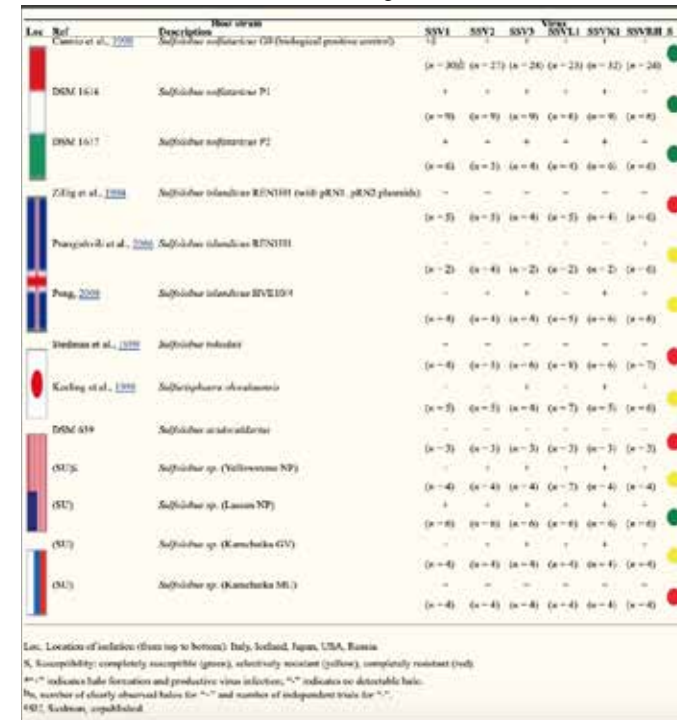


Table 1: Infectivity/susceptibility profiles of *Sulfolobaceae* (reproduced from (Ceballos et al., 2012)).

Sulfurisphaera tokodaii vs. *Sulfurisphaera ohwakuensis* (S311 vs. S198)

Sulfurisphaera is a close relative of the genus *Sulfolobus* with *Sulfurisphaera tokodaii* and *Sulfolobus acidocaldarius* sharing 90% of 16S ribosomal DNA. *S. tokodaii* (S311) and *S. ohwakuensis* (S198) are genomically similar sharing having identical 16S rDNA genes (Kurosawa et al. 1998). However, *S. ohwakuensis* was found to be susceptible to infection by SSV3, SSV9, and SSV8 while *S. tokodaii* was resistant to all tested SSVs (Ceballos et al. 2012). This was the first report of SSV infection outside of the *Sulfolobus* genus establishing that SSV infection is not limited to *Sulfolobus*. Therefore, SSV infection susceptibility may be driven by specific genomic features rather than genetic divergence. Plasmids of the pRN family (pST1 and pST3) have been found to be integrated into the genome of *S. tokodaii* (She, Brügger and Chen 2002). Similarly, *Sulfolobus islandicus* REN1H1 also contains pRN plasmids and expressed resistance to all tested SSVs as well (Ceballos et al. 2012). Analysis of these pRN-type plasmids may provide insight into the SSV resistance of both strains. The susceptibility of *S. ohwakuensis* to SSV infection remains unclear.

Mutnovsky Isolate vs. Geyser Valley Isolate (S150 vs. S147)

Two *Sulfolobaceae* isolates, a Mutnovsky isolate (MU) (S150) and a Geyser Valley isolate (GV) (S147), were derived from volcanic hot springs in Kamchatka, Russia. MU has been determined to be quasi-sympatric while GV was determined to be sympatric. However, MU has been shown to be resistant to SSV9 infection while GV was susceptible to SSV9 infection. Moreover, SSV9 infection of GV does not result in cell lysis as seen in allopatric hosts. Instead, the infection resembles non-lytic replication characteristic of other SSVs. This may be driven by allopatric evolution (Ceballos et al. 2020). Currently, the genus and species of these isolates have not yet been determined.

Sulfolobus islandicus (S42 vs. S17)

Sulfolobus islandicus REN1H1 (S42) which harbors two plasmids pRN1 and pRN2, with neither of these having a sequence similarity to any SSV genomes, was shown to be resistant to all SSVs (Ceballos et al. 2012). When the strain was cured of the two plasmids, REN1H1 (S17) was found to be susceptible to infection by SSV8 (Purschke and Schäfer 2001). Therefore, the susceptibility due to the absence of the plasmids is unclear.

Genome Assembly

To explore potential genetic underpinnings for differences in virus-host growth dynamics, a comparative analysis of the three pairs is necessary. However, prior to analysis, the genomes of the six different strains must be sequenced and assembled. Previous sequencing technologies such as Sanger or Illumina presented difficulties in resolving repetitive sequences when it comes to *de novo* assembly of larger genomes (Lu, Giordano and Ning 2016). Fortunately, the introduction of long-read sequencing technology such as MinION from Oxford Nanopore Technologies allows for sequencing of extremely long fragments without a reduction in sequence quality (Jain et al. 2015). How-

ever, studies have shown that the data produced from such long read sequencing devices often yield error-prone long reads and an overall high error rate (>5%) (Loman, Quick and Simpson 2015). Assembly pipelines have relied on additional time-consuming and resource-intensive steps such as error-correction and consensus-generation as a result of these high error rates. Methods such as Canu (Koren et al. 2017) and HGAP (Chin et al. 2013) have significantly improved the error rates and run-times of genome sequencing using nanopore. However, they are still involved in a larger process which can be broken down into the three stages of genome assembly: (1) error correction; (2) assembly of corrected reads; and (3) polishing (Loman, Quick and Simpson 2015). This process can be time exhaustive and prone to error as each step requires a specific set of tools and requisitive dependencies. Moreover, maintaining a workflow while allowing for rapid modification or adaptability to accommodate new analyses and data can often be a challenging task.

Here, we address this need for a more efficient, adaptable workflow by creating an autonomous, reproducible, and scalable genome assembly pipeline for *Sulfolobaceae* using Snakemake (Köster and Rahmann 2012). In addition to creating a reproducible pipeline, a phylogenetic analysis of the six genomes was also carried out in order to identify the Mutnovsky and Geyser Valley isolates.

Materials and Methods

Virus Isolation and Growth

Isolation and growth of each of the six strains were carried out as previously described (Ceballos et al. 2020).

Genome Sequencing

The six *sulfolobaceae* strains were sequenced on a MinION device (Oxford Nanopore Technology, ONT) and basecalling was done using Guppy (ONT).

Genome Assembly

Initially, the genome assembly pipeline precedes with merging all the fastq files generated from the Guppy basecaller. Base quality filtering was done with Filtlong for long reads. The parameters for filtering were as follows: minimum length was set to 3000 bp, mean quality weight was 30, length weight was 10, keep percent was 90%, and target bases was set to 100 Mbp. Following quality filtering, assembly of the genome was carried out using Flye with a genome size of 3m, 8 threads, and 5 iterations. The assembled fasta file was further processed and mapped with SAMtools and Burrow-Wheels Aligner (BWA). Finally, the assembled fasta file was indexed and polished with Nanopolish.

Phylogenetic Analysis

The genome sequences of the six *sulfolobaceae* strains were annotated using DFAST and uploaded to the Geneious Prime 2020.2.2 program. An additional seven *sulfolobaceae* genomes from the NCBI database including two references genomes were uploaded as well. The 16S and 23S rRNA genes were extracted from each of the strains and aligned using MUSCLE with default parameters. The ends of the genes were then trimmed and realigned. A phylogenetic tree was then generated

from the 16S and 23S rRNA genes using PhyML with default parameters and 1,000 samplings. In addition, the sequences from all six *sulfolobaceae* strains were also aligned using Mauve algorithm with default parameters for pairwise analyses of the genomes.

Implementation

The genome assembly pipeline can be broken down into three main steps: (1) quality control, (2) assembly, and (3) polishing (Figure 2). Each step can then be further divided into separate rules; each rule can be run independently, or all three steps can be combined in a complete workflow. The pipeline is implemented in Python and uses the Snakemake workflow manager allowing the pipeline to be reproducible, scalable, and autonomous. The pipeline is reproducible as it is based on a configuration, or config, file, which contains all of the required software packages and dependencies along with their respective versions. A user only needs to download Conda, which is the management system; Snakemake; and the genome assembly pipeline package, which is a Snakefile containing the code and the config file. The pipeline is scalable as it can be run on a personal computer or supercomputer by specifying the number of cores. Additional steps can be added, removed, or modified as necessary. Finally, the pipeline is autonomous as running the pipeline requires a single command, and all the output is stored into a single folder which is divided into easy-to-navigate sub-folders containing the generated files.

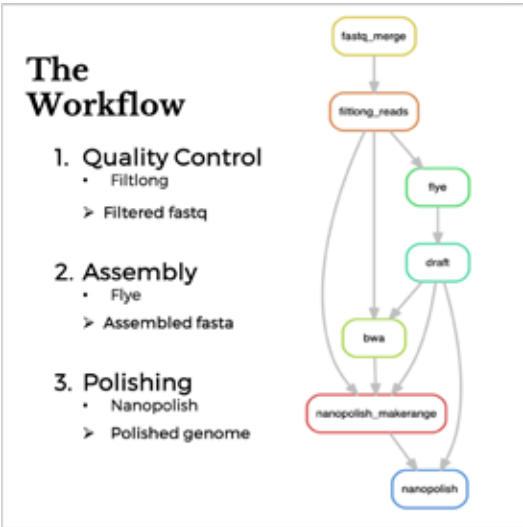


Figure 2: Overview of the genome assembly workflow. The workflow can be broken down into three main steps: (1) quality control, (2) assembly, and (3) polishing.

Results

General Features and Structure of the Sulfolobaceae Genomes

The general features of the six sequenced *Sulfolobaceae* genomes are reported in Table 2. The largest genome belonged to *Sulfurisphaera ohwakuensis* at 2.88 Mb and the smallest being the Geyser Valley isolate geome at 2.58 Mb. Interestingly, the Geyser Valley isolate genome was also significantly smaller, contained fewer genes, and lacked a CRISPR in comparison to the Mutnovsky isolate even though the Mutnovsky

isolate is quasi-sympatric. There were also significant differences between the two *Sulfolobus islandicus* REN1H1 strains with a 0.09 Mb difference in genome size and almost 150 difference in number of genes.

	<i>Sulfurisphaera tokodaii</i>	<i>Sulfurisphaera ohwakuensis</i>	Mutnovsky isolate	Geyser Valley isolate	<i>Sulfolobus islandicus</i> REN1H1 with pRN plasmids	<i>Sulfolobus islandicus</i> REN1H1 without pRN plasmids
Genome size (Mb)	2.70	2.88	2.76	2.58	2.84	2.75
Gene no.	3416	3807	3284	2953	3531	3387
CRISPR no.	7	6	3	4	3	3
GC content (%)	32.8	32.7	35.2	35.0	35.2	35.1

Table 2: Comparison of six *Sulfolobaceae* strains. Following assembly, the six strains were annotated using DFAST. Data generated from the gene annotation of each strain was compiled into a table including genome size, number of genes, number of CRISPRs, and GC content.

The program Mauve was used for alignment of the six *Sulfolobaceae* genomes and visualization of genome rearrangements. All the genomes have a common general organization in relation to its respective pair. The largest amount of differences within the pairwise genome alignments was found between *Sulfurisphaera tokodaii* and *Sulfurisphaera ohwakuensis*. Both genomes contain several relatively small species-specific regions and a small variable region. The pair with the least amount of differences was the *Sulfolobus islandicus* REN1H1 with and without the pRN plasmids. However, an approximately 5 kb deletion was found between 1.95 Mb and 1.97 Mb in each of the strains. Interestingly, the deletions in both of the strains appear to be the same size and upon mapping the segments back to one of the strains they matched up perfectly.

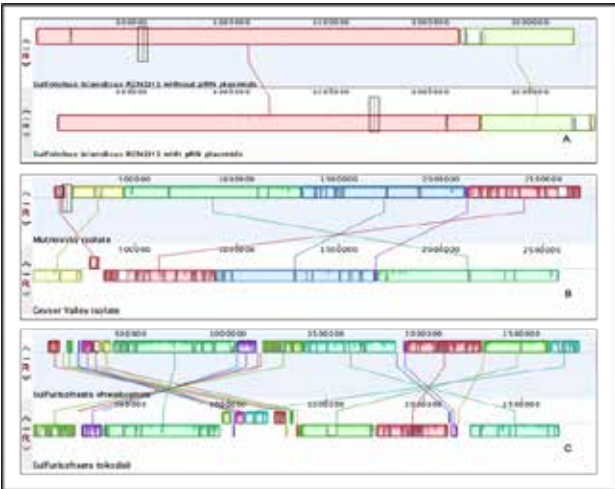


Figure 3: Alignment of the six *Sulfolobaceae* genomes by pairs using Mauve. (A) *Sulfolobus islandicus* with and without the pRN plasmids. (B) The Geyser Valley and Mutnovsky isolates, and (C) *Sulphurisphaera Ohwakuensis* and *Sulphurisphaera tokodaii*. The blocks of the same color indicate region of synten. The unique regions are indicated by the absence of blocks.

Phylogenetic Position of Isolates

The sequence identity of the Mutnovsky isolate 16S rRNA gene to the Geyser Valley isolate was 98.7%. In relation to *Sulfolobus islandicus* REN1H1, *Sulfolobus islandicus* LAL14/1, *Saccharolobus solfataricus*, and *Saccharolobus shibatae*, the sequence identity of the Mutnovsky isolate was 99.4%, 98.9%, 98.7%, and 98.2%, respectively. The Geyser Valley isolate relative to the latter was also 98.9%, 98.7%, 98.6%, and 98.1%. Sequence identity of both the isolates to other type strains of *Sulfolobaceae* were less than 91.7%. Phylogenetic analysis using the maximum-likelihood method based on the 16S rRNA always clustered the two isolates, *Sulfolobus islandicus*, and *Saccharolobus* strains together with high bootstrap value (Figure 3). More specifically, the isolates were clustered with *Sulfolobus islandicus* strains, but the bootstrap value for this separation was only slightly above 50. The sequence identities of the 23S rRNA gene sequences of both isolates and related species were all greater than 98% for *Sulolobus islandicus* REN1H1, *Sulfolobus islandicus* LAL14/1, *Saccharolobus solfataricus*, and *Saccharolobus shibatae*.

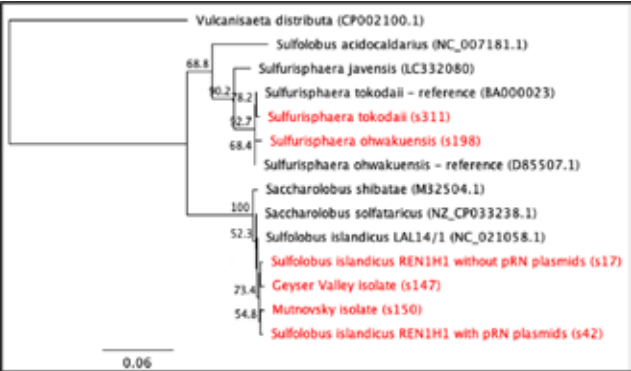


Figure 4: Maximum-likelihood tree constructed from 16S rRNA gene sequences of *Sulfolobaceae*. Bootstrap values derived from 1,000 samplings are shown at branch nodes; only values >50% are shown. GenBank accessions numbers are given in parentheses.

Discussion

Pairwise Differences Increase with Biogeographic Diversity

As expected, more differences were observed between genomic features and structure as biogeographic diversity increased among the strains. Differences in genomic features were most prevalent between *Sulfurisphaera tokodaii* and *Sulfurisphaera ohwakeuensis* with 0.18 Mb in genome size, almost 400 genes, and one CRISPR. Interestingly, the Geyser Valley isolate had the smallest genome size at 2.58 Mb which was 0.18 Mb smaller than the Mutnovsky isolate. There was also a difference of approximately 300 genes and one CRISPR between two the isolates despite the Mutnovsky isolate being quasi-sympatric. However, the most interesting observation was differences between the *Sulfolobus islandicus* REN1H1 strains. As the only difference between the strains was the presence of the pRN plasmids, therefore, little to no differences were expected in genome size and number of genes. However, the *Sulfolobus islandicus* strain lacking the plasmids appeared to be 0.09 Mb smaller

and had almost 150 fewer genes than the *Sulfolobus islandicus* strain with the plasmids present. This suggest that some of the observed differences in the genomic features may be a result of the quality of genome assembly.

In terms of genomic structure as seen in figure 3, the two *Sulfolobus islandicus* strains were relatively identical as the only difference between the two strains was the presence of the pRN plasmids. There was an approximately 5 kb deletion observed in each of the strains. However, further analysis found overlap in the supposed deletion region that was not aligned. After mapping one of the segments back to the *Sulfolobus islandicus* strain, it appeared to match up perfectly with each other. Therefore, the deletion within each of the strains may simply be a duplication and rearrangement of the genome sequence. Minor differences were observed between the genomes of the sympatric Geyser Valley isolate and the quasi-sympatric Mutnovsky isolate. The two isolates were located approximately 250 km apart. Significant differences were observed between the two genomes of *Sulfurisphaera tokodaii* and *Sulfurisphaera ohwakuensis* as they are two different species in the same genus. These two strains were located approximately 800 km apart. Therefore, differences between genomic features and structure increase with biogeographic diversity.

Identification of Isolates

The maximum-likelihood (ML) phylogenetic tree generated from the 16S rRNA genes of the *Sulfolobaceae* strains clusters the Mutnovsky and Geyser Valley isolates with *Sulfolobus islandicus* REN1H1 and *Sulfolobus islandicus* LAL14/1 (Figure 4). The sequence identity for the two isolates relative to the two *Sulfolobus islandicus* strains are 99.4% and 98.9%, respectively. This suggest that the two isolates may be *Sulfolobus islandicus* strains. However, the 23S rRNA ML phylogenetic tree interestingly clusters the two isolates with *Saccharolobus solfataricus* instead of *Sulfolobus islandicus* (not shown). Therefore, the two isolates cannot be identified with certainty, but phylogenetic analysis suggests that the isolates are either *Sulfolobus islandicus* or *Sachharolobus solfataricus* strains. The underpinnings for the phylogenetic differences between the 16S rRNA and 23S rRNA trees unknown at this time. However, it may be the result of random mutations within the two genes, which may also help to explain the observed low bootstraps values. Note that *Sulfolobus islandicus*, having close 16S and 23S rRNA gene sequence similarity (>98%) to *Saccharolobus shibatae* and *Saccharolobus solfataricus*, should be affiliated with the genus *Saccharolobus* as previously suggested (Sakai and Kurosawa 2018).

Conclusion

Our results indicate that: (1) the genome assembly pipeline is reproducible, scalable, and autonomous; (2) differences between genomic features and structures increase with biogeographic diversity; and (3) the Mutnovsky and Geyser Valley isolates are likely *Sulfolobus islandicus* or at least in the *Saccharolobus* and *Sulfolobus islandicus* clade. To better identify the Geyser Valley and Mutnovsky isolate, a maximum-likelihood phylogenetic tree should be constructed using internal transcribed spacers to resolve the differences between the 16S

rRNA and 23S rRNA trees. Uing other methods or tools of genome assembly will ensure proper genome assembly if similar results are achieved. Moreover, additional polishing steps should be added to the pipeline to resolve nuisances such as genome size, number of genes, or number of CRISPRs and to improve the overall quality of the genome assembly. These results and this genome assembly pipeline form a solid foundation to support future work focused on determining the genetic underpinnings of virus-host growth dynamics.

References

Bautista, M. A., Zhang, C. and Whitaker, R. J. (2015) ‘Virus-induced dormancy in the archaeon Sulfolobus islandicus’, mBio, 6(2).

Brock, T. D., Brock, K. M., Belly, R. T. and Weiss, R. L. (1972) ‘Sulfolobus: a new genus of sulfur-oxidizing bacteria living at low pH and high temperature’, Arch Mikrobiol, 84(1), pp. 54-68.

Brockhurst, M. A., Morgan, A. D., Fenton, A. and Buckling, A. (2007) ‘Experimental coevolution with bacteria and phage: The Pseudomonas fluorescens—Φ2 model system’, Infection, Genetics and Evolution, 7(4), pp. 547-552.

Ceballos, R. M., Drummond, C., Stacy, C. L., Crespo, E. P. and Stedman, K. (2020) ‘Host-dependent differences in replication strategy of the Sulfolobus Spindle-shaped Virus strain SSV9 (a.k.a., SSVK1): Lytic replication in hosts of the family Sulfolobaceae’, bioRxiv, pp. 2020.03.30.017236.

Ceballos, R. M., Marceau, C. D., Marceau, J. O., Morris, S., Clore, A. J. and Stedman, K. M. (2012) ‘Differential virus host-ranges of the Fuselloviridae of hyperthermophilic Archaea: implications for evolution in extreme environments’, Front Microbiol, 3, pp. 295.

Chin, C. S., Alexander, D. H., Marks, P., Klammer, A. A., Drake, J., Heiner, C., Clum, A., Copeland, A., Huddleston, J., Eichler, E. E., Turner, S. W. and Korlach, J. (2013) ‘Nonhybrid, finished microbial genome assemblies from long-read SMRT sequencing data’, Nat Methods, 10(6), pp. 563-9.

Ciaramella, M., Pisani, F. M. and Rossi, M. (2002) ‘Molecular biology of extremophiles: recent progress on the hyperthermophilic archaeon Sulfolobus’, Antonie Van Leeuwenhoek, 81(1-4), pp. 85-97.

Jain, M., Fiddes, I. T., Miga, K. H., Olsen, H. E., Paten, B. and Akeson, M. (2015) ‘Improved data analysis for the MinION nanopore sequencer’, Nat Methods, 12(4), pp. 351-6.

Koren, S., Walenz, B. P., Berlin, K., Miller, J. R., Bergman, N. H. and Phillippy, A. M. (2017) ‘Canu: scalable and accurate long-read assembly via adaptive’, Genome Res, 27(5), pp. 722-736.

Kurosawa, N., Itoh, Y. H., Iwai, T., Sugai, A., Uda, I., Kimura, N., Horiuchi, T. and Itoh, T. (1998) ‘Sulfurisphaera ohwakuensis gen. nov., sp. nov., a novel extremely thermophilic acidophile

of the order Sulfolobales’, Int J Syst Bacteriol, 48 Pt 2, pp. 451-6.

Köster, J. and Rahmann, S. (2012) ‘Snakemake--a scalable bioinformatics workflow engine’, Bioinformatics, 28(19), pp. 2520-2.

Loman, N. J., Quick, J. and Simpson, J. T. (2015) ‘A complete bacterial genome assembled de novo using only nanopore sequencing data’, Nat Methods, 12(8), pp. 733-5.

Lu, H., Giordano, F. and Ning, Z. (2016) ‘Oxford Nanopore MinION Sequencing and Genome Assembly’, Genomics Proteomics Bioinformatics, 14(5), pp. 265-279.

Munson-McGee, J. H., Peng, S., Dewerff, S., Stepanauskas, R., Whitaker, R. J., Weitz, J. S. and Young, M. J. (2018) ‘A virus or more in (nearly) every cell: ubiquitous networks of virus-host interactions in extreme environments’, ISME J, 12(7), pp. 1706-1714.

Palm, P., Schleper, C., Grampp, B., Yeats, S., McWilliam, P., Reiter, W. D. and Zillig, W. (1991) ‘Complete nucleotide sequence of the virus SSV1 of the archaeobacterium Sulfolobus shibatae’, Virology, 185(1), pp. 242-50.

Pauly, M. D., Bautista, M. A., Black, J. A. and Whitaker, R. J. (2019) ‘Diversified local CRISPR-Cas immunity to viruses of Sulfolobus islandicus’, Philos Trans R Soc Lond B Biol Sci, 374(1772), pp. 20180093.

Purschke, W. G. and Schäfer, G. (2001) ‘Independent replication of the plasmids pRN1 and pRN2 in the archaeon Sulfolobus islandicus’, FEMS Microbiol Lett, 200(1), pp. 97-102.

Reiter, W. D., Palm, P., Yeats, S. and Zillig, W. (1987) ‘Gene expression in archaeobacteria: physical mapping of constitutive and UV-inducible transcripts from the Sulfolobus virus-like particle SSV1’, Mol Gen Genet, 209(2), pp. 270-5.

Sakai, H. D. and Kurosawa, N. (2018) ‘Saccharolobus caldissimus gen. nov., sp. nov., a facultatively anaerobic iron-reducing hyperthermophilic archaeon isolated from an acidic terrestrial hot spring, and reclassification of Sulfolobus solfataricus as Saccharolobus solfataricus comb. nov. and Sulfolobus shibatae as Saccharolobus shibatae comb. nov’, Int J Syst Evol Microbiol, 68(4), pp. 1271-1278.

Schleper, C., Kubo, K. and Zillig, W. (1992) ‘The particle SSV1 from the extremely thermophilic archaeon Sulfolobus is a virus: demonstration of infectivity and of transfection with viral DNA’, Proc Natl Acad Sci U S A, 89(16), pp. 7645-9.

She, Q., Brügger, K. and Chen, L. (2002) ‘Archaeal integrative genetic elements and their impact on genome evolution’, Res Microbiol, 153(6), pp. 325-32.

Tsuboi, K., Sakai, H. D., Nur, N., Stedman, K. M., Kurosawa, N. and Suwanto, A. (2018) ‘Sulfurisphaera javensis sp. nov., a hyperthermophilic and acidophilic archaeon isolated from In-

donesian hot spring, and reclassification of Sulfolobus tokodaii Suzuki et al. 2002 as Sulfurisphaera tokodaii comb. nov’, Int J Syst Evol Microbiol, 68(6), pp. 1907-1913.

Zhang, J., Zheng, X., Wang, H., Jiang, H., Dong, H. and Huang, L. (2020) ‘Novel Sulfolobus fuselloviruses with extensive genomic variations’, J Virol, 94(8).

About the Author

John Le is a junior at Notre Dame majoring in science-business with a minor in digital marketing. His research was conducted during a remote summer research internship with Dr. Ruben Ceballos and Dr. Ek Han Tan at the University of Arkansas. During the semester, he serves as a teaching assistant for the introductory biology labs as well as a tour guide for the university. After graduating from Notre Dame, Le hopes to work in the biotech or pharmaceutical industry with prospects of medical school in the future.

A Numerical Investigation Into Modeling LEO Orbital Decay

Andrew Langford
University of Notre Dame, Department of Physics

Abstract

This paper presents an original numerical method for calculating orbital decay of artificial satellites in Low Earth Orbit (LEO). Difficulties in orbital decay calculations arise from coupled nonlinear differential equations of motion and the reliance on atmospheric modeling. Of the models readily available for use, few consider factors such as space weather fluctuations and mass to area ratios of the spacecraft. Our approach combined the usage of multiple atmospheric models to qualitatively describe uncertainty while also considering factors such as solar activity and mass to area ratios. The novel method takes advantage of the bound potential state of a two-body system by utilizing the spacecraft’s tangential velocity as the unifying dimension. The model was tuned and tested against existing mission data. Multiple uses for the model include single trajectory visualization, orbit lifetime calculations, and mission planning. The success of the model’s adaptability and accuracy suggests its usefulness for future studies in astrodynamic research.

Introduction

Since the beginning of the spaceflight era, scientists and engineers have relied on orbital trajectory calculations to ensure safety and meet mission requirements. A facet of spacecraft trajectory in LEO is orbital decay. Orbital decay is a result of particles in the high atmosphere inducing a drag force on spacecraft. As seen in Equation 1 Glenn (2015a), the drag force is a function of the spacecraft’s tangential velocity v and

$$F_d = \frac{1}{2} * C_d * \rho(a) * v(a)^2 \tag{1}$$

atmospheric density ρ . Both are functions of orbital altitude, a . Since a spacecraft’s tangential velocity increases with lower altitudes, and lower altitudes have higher atmospheric density, the orbital decay is a positive feedback loop which exponentially affects spacecraft as their orbits lower. A model of this phenomena is useful for two measures:

1. Predicting atmospheric re-entry of defunct spacecraft
2. Mission planning for LEO satellites

Predicting Atmospheric Re-entry of Defunct Spacecraft

As of late, an increasing number of orbital debris or “space junk” has contaminated the LEO space. These orbital debris include launch vehicle stages, defunct satellites, and fragmentation debris. With the advent of small satellites and

commercial space access, it is inevitable that LEO will become increasingly crowded with in-use and terminated spacecraft. These orbital hazards pose a serious threat to the safety of humans in space and on Earth. For this reason, mission planners have begun to implement measures which will decrease the chance of collision with ongoing missions.

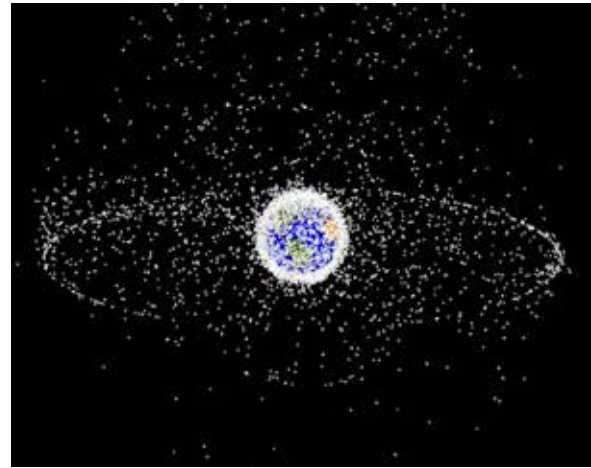


Figure 1. Data-generated graphic of orbital debris viewed from high Earth orbit. The two dense orbital fields present are Low Earth Orbit (LEO) and Geosynchronous Orbit (GEO) (Garcia 2015).

One popular measure is to de-orbit the spacecraft using either a retrograde burn or natural atmospheric drag. In many cases, both are used to decay the orbit to a point where the spacecraft burns up in the atmosphere. As a mission planner, a model of natural atmospheric decay would be a helpful tool for determining the required fuel needed to de-orbit the spacecraft in an adequate time period.

Mission Planning for LEO Satellites

Low Earth Orbit (LEO) is an advantageous orbit for its ease of access and near Earth observation capability. However, these advantages are a result of LEO being extremely close to Earth as shown in figure 2. As a result, LEO spacecraft experience a high atmospheric drag force when compared to spacecraft in higher orbits. Consequently, natural orbital decay of LEO spacecraft must be accounted for when mission planning. In this regime, the initial height of the orbit will significantly impact the lifetime of the mission and influence the objectives which can be completed. Therefore a reliable model of mission lifetimes in the presence of LEO atmospheric drag is essential. In this paper, a case study of a 3U CubeSat, AERO, will be discussed including a brief investigation into how various initial orbital altitudes will affect the ability to meet mission requirements.

Methods of Computation

While orbital decay is built on intuitive physical principles, an attempt at modeling a solution presents a variety of challenges. For one, the two forces on the spacecraft, gravitational and drag, are along orthogonal basis vectors. Therefore, Newtonian formalism fails to capture the scope of the problem. Instead, a more modern physics approach is helpful. Given that

the spacecraft is orbiting the Earth, it can be considered as a particle in a bound potential state. Therefore, its energy is a function of position. In this case, the velocity is determined by the altitude the spacecraft is orbiting. Coupled with the fact that atmospheric density is also a function of the spacecraft’s altitude, the interaction of perpendicular forces can be explained through the means of orbital velocity. Luckily, the relationships between orbital period, orbital altitude, and orbital velocity have been around for some time, and their manipulation is now all that is needed to find a solution.

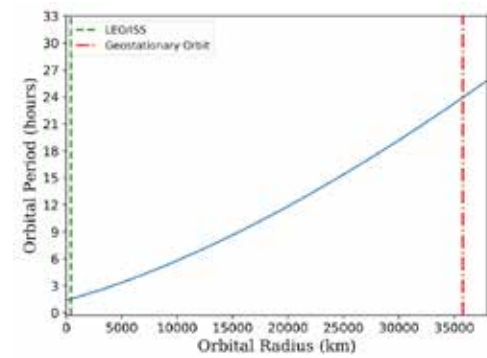


Figure 2. Using functions created for the orbital decay model to plot the relationship between orbital radius and orbital period. For context, the radii of LEO (400 km) and GEO (36,000 km) are plotted.

Analytic Derivations

Equation 2 illustrates some of the issues with addressing the orbital decay problem with a straightforward Newtonian approach. In a rotating frame the gravitational force is acting in the z direction while the drag force is acting in the i direction.

$$\sum F_{total} = \frac{GMm}{z^2} \mathbf{z} - \frac{1}{2} * C_d * \rho(z) * v^2 \mathbf{i} \tag{2}$$

In the following derivations, P is the orbital period, μ is the standard gravitational parameter, v is the tangential velocity of the spacecraft, and a is the radius of the orbit above Earth’s center.

An important first step is finding the relationship between altitude and velocity in the bound system. Equating the gravitational force to centripetal force and solving for velocity, it is apparent in Equation 3 that the tangential velocity decreases with altitude.

$$v(a) = \sqrt{\frac{\mu}{a}} \tag{3}$$

In upcoming derivations, the form $a = \mu/v^2$ is proven useful for substitution purposes. Another relationship to define is between the orbital period and orbital tangential velocity.

$$\begin{aligned} \frac{GMm}{a^2} &= \frac{mv^2}{a} \\ \frac{\mu}{a} &= \frac{v^2}{a} = \omega^2 a \\ \text{and } \omega &= \frac{2\pi}{P} \end{aligned}$$

Rearranging lines 2 and 3 gives the familiar Equation 4.

$$P^2 \mu = 4\pi^2 a^3 \tag{4}$$

Now making use of the bound state relationships, the orbital period can be put in terms of orbital velocity.

$$P = \frac{2\pi \mu}{v^3} \tag{5}$$

The last relationship to address is between atmospheric density and orbital velocity. The atmospheric density model $\rho(a)$ can be altered to be a function of orbital velocity with the velocity to altitude equation established above in Equation 3. However, a reliable atmospheric density model is an essential to the accuracy of orbital decay calculations. For this reason, a thorough investigation into the available models was conducted. We will explore the findings and conclusions in section 2.2.

Atmospheric Models

Atmospheric density models are used in a variety of engineering and scientific endeavors. The atmosphere is dynamic system which involves thermodynamic, chemical, and fluid mechanic properties. Since atmospheric density is variable at any given moment in time, it is helpful to characterize the value using “standard atmosphere” conditions (Glenn 2015b).

Atmospheric density models from two space agencies, NASA and the Australian Space Agency (ASA), were compared to test their validity and assess the usage in the orbital decay modeling. One of the preconditions for these models is the ability to give accurate densities at extremely high altitudes. Many atmospheric models are for altitudes appropriate for atmospheric flight (< 12 km); however, the spacecraft will be experiencing atmospheric densities at altitudes $50 < a < 500$ km.

The NASA atmospheric model chosen is optimized for calculating densities in the stratosphere (> 25 km) (Glenn 2015b). This makes it an eligible model for use in our calculations. Equation 6 gives the formula for atmospheric density where h is the altitude in meters, T is the temperature in Celsius, p is the pressure in kilo-Pascals, and ρ is the air density in kg/m³. It is a function of altitude; however, with the altitude to velocity relationship, a simple substitution can be made for the model’s use.

The ASA atmospheric model is broken into two

$$\begin{aligned} T &= -131.21 + .00299h \\ p &= 2.488 * \left[\frac{T + 273.1}{216.6} \right]^{-11.388} \\ \rho &= \frac{p}{(.2869 * (T + 273.1))} \end{aligned} \tag{6}$$

sections, a model from 25 to 180 km and a model from 180 to 500 km. Combining the results of these two sections creates a comprehensive function for use in the orbital decay calculations. While the lower altitude model is fit with a Legendre Polynomial, the higher altitude model considers space weather

conditions to calculate the atmospheric density. These two space weather parameters are the solar flux at 10.7 cm, F 10.7, and geomagnetic activity, Ap. Increases in both parameters result in denser atmospheric conditions at high altitudes. Figure 3 gives an illustration of the range of Ap and F 10.7 values to be considered when calculating atmospheric density. Given that Ap and F 10.7 tend to trend in similar fashion, density calculations with low, medium, and high activity for both parameters should be adequate at characterizing the possible atmospheric conditions. For the assessment of the atmospheric model, F 10.7 values of [50, 100, 150, 200] and Ap values of [7, 14, 21, 28] will be calculated. In future modeling, a more limited scope will be used to characterize realistic mission conditions.

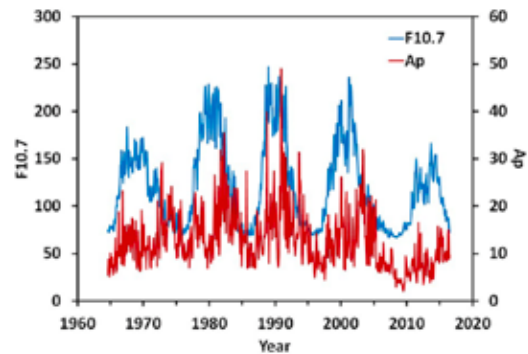


Figure 3. Historical F 10.7 and Ap data (Gavrilyeva and Ammosov 2018). This record was used in determining the appropriate F10.7 and Ap values to account for in orbital decay modeling.

Figure 4 provides a visual comparison of the two atmospheric models. There are a few key takeaways from this important plot. For one, it is a good confirmation that in general both models agree on the trend of atmospheric density. At higher altitudes, the models are within an order of magnitude. For this reason, we can assume that these models are a reliable basis for orbital decay calculations. Another takeaway is the influence that high space weather activity can have on high altitude atmospheric densities. The difference between the range of F 10.7 and Ap indices is roughly two orders of magnitude. Therefore, in orbital decay calculations, there should be parameters which take into account the space weather conditions. These parameters could also provide a qualitative uncertainty parameter when predicting the decay time of LEO satellites.

Numerical Method

Using a numerical method, we aimed to create a model which simulates the decay of a spacecraft's orbital altitude through time. The results of this model can be used in various capacities, some of which will be explored in section 3.

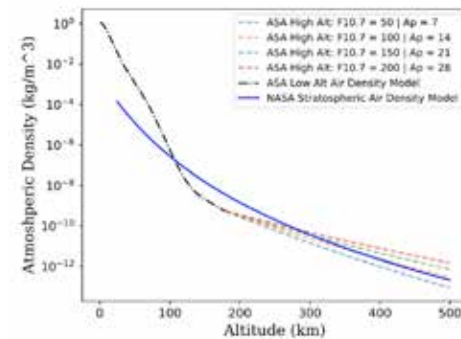


Figure 4. Comparison plot of NASA and ASA atmospheric density models. Various space weather conditions are illustrated using the ASA model at high altitudes. As the F 10.7 and Ap indices increase, the atmosphere is denser at high altitudes.

Numerical Adaptation of Analytic Conclusions

The coupled nonlinear ODE's to be solved are shown in Equation 7. It is quite evident that no analytical solution for $z(t)$ can be derived from these equations. Here z is substituted for the semi-major axis variable a so as to not confuse it with the acceleration of the spacecraft.

$$\begin{aligned} \frac{dv}{dt} &= -K * \rho(z) * v^2 \hat{\mathbf{i}} \\ \frac{dz}{dt} &= \frac{d}{dt} \left(-\frac{\mu}{v^2} \right) \hat{\mathbf{z}} \end{aligned} \quad (7)$$

Therefore, we must rely on numerical techniques in order to solve for a model. Using the derivations in section 2.1 and atmospheric models in section 2.2, a numerical calculation becomes relatively simple. A reformulated differential equation using the relationships developed in section 2.1 is shown in Equation 8.

$$\begin{aligned} a &= \frac{dv}{dt} = -\frac{A * C_d}{2m} * \rho(v) * v^2 \hat{\mathbf{i}} \\ \int_{v_i}^{v_f} dv &= \int_{t_i}^{t_f} -\frac{A * C_d}{2m} * \rho(v) * v^2 dt \hat{\mathbf{i}} \end{aligned} \quad (8)$$

From Equation 9, it is evident that a suitable Δt must be determined in order to find a numerical solution to any $a(t)$. Unlike some numerical ODE solvers, the right bound of the independent variable, t is unknown. For this particular ODE solver, the step dimension is time. Luckily, there is an easily associated Δt for each step, the orbital period. In these calculations the orbital period, τ , corresponding to the initial orbital velocity v , will be used as the time interval between iterations. Thus the time intervals will appropriately respond to changes in the orbital velocity preserving the same precision of the calculations.

$$\begin{aligned} \Delta v &= -\frac{A * C_d}{2m} * \rho(v) * v^2 * \Delta t \\ \Delta a &= \frac{\mu}{\Delta v^2} \end{aligned} \quad (9)$$

Iterative Process

In the model, the primary independent variable is the initial orbital altitude. However, other secondary parameters which affect the orbital decay include the mass to area ratio (m/A), atmospheric model ($\rho(a)$), and space weather conditions (F10.7 and Ap). When explaining the iterative process, we will assume that all secondary parameters are given.

The numerical simulation begins with a user input of the initial orbital altitude. It then relies on the “delta v ” function which takes an initial velocity argument, v , and calculates the new velocity of the spacecraft, v_f , after one orbital period with atmospheric drag forces. This process is shown step by step below.

1. Velocity \rightarrow Altitude \rightarrow Atmospheric Density - ρ
2. Velocity \rightarrow Altitude \rightarrow Orbital Period - τ
3. Calculation of Δv with v , ρ , τ using Equation 9
4. Find new v_f by adding Δv to the initial v

While the steps above seem relatively straightforward, there is a non-intuitive measure taken. In normal classical mechanics, when a particle experiences a drag force, the particle slows down. However, as in the Bohr Model of an atom, a decrease in energy level results in an increase in the expected velocity of the particle. Here, the atmospheric drag force is decreasing the spacecraft's total mechanical energy within Earth's potential well due to thermal heating. In order to satisfy orbital mechanical laws, the spacecraft will experience a natural increase in tangential velocity. Therefore, the calculation of Δv is added to the initial velocity to meet these conditions.

Using the outputs of the “delta v ” function, a function, “orbital decay” can iterate the calculations until a condition is met. Namely, the spacecraft has met a critical altitude where the atmosphere density and velocity are enough to burn up the spacecraft. The commonly used “Kármán line” of 100 km is a satisfactory critical altitude.

The “orbital decay” function can be optimized to display various results. One option is to plot the $a(t)$ graph for one orbital decay of one spacecraft. However, by returning the final last time value before termination, the paths of multiple trajectories can be shown for a more dynamic visualization of the model's results. Examples of these plots are shown in section 3.

Model Analysis

The success of the orbital decay model is proved through its agreement with existing data and adaptability to different parameters. Additionally, the model's output provides flexibility in visualizing a range of results from the model. Additional uses for the function created are shown in the Appendix.

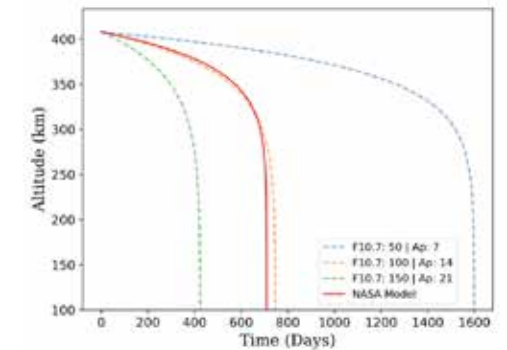


Figure 5. A single orbital decay simulation with identical parameters to the International Space Station: altitude = 408 km, $m/A = 52 \text{ kg/m}^2$. The figure shows possible trajectories based on different atmospheric density models. The ASA high altitude models illustrate how an increase in space weather activity can significantly decrease the orbital lifetime of a spacecraft.

Single Trajectory Models

The first result we will discuss is of a simple test particle with parameters similar to the International Space Station, altitude of 408 and m/A of 52 kg/m^2 . In figure 5, various decay trajectories are shown with differing atmospheric models. Using the ASA high altitude atmospheric model, a range of space weather conditions can be simulated resulting in radically different orbital trajectories. Our earlier predictions that an increase in space weather will result in faster orbital decay is confirmed.

The ISS requires its orbit to be boosted approximately every three months by visiting spacecraft in order to stay in a stable orbit. For regular or active solar weather, our model would agree that every 90 days is an appropriate time to heighten the orbit in order to stay at a relatively constant altitude. However, for unusually inactivate solar period, the ISS could go for more than a year without needing to boost its orbit. This model also predicts that when the very sad day comes when the ISS program is terminated, it will take roughly an additional two years for the ISS to burn up in the atmosphere. Hopefully this is done because we have a moon station!

Another interesting investigation of the single trajectory model visualization is testing the validity of the model against real mission data. NASA's Solar Maximum Mission was launched in 1980 to study the sun in a period of solar maximum. This can be visually confirmed by referencing back to figure 3. At the end of its mission lifetime in 1989, the satellite lost attitude control and began to naturally fall back into the atmosphere (Kennewell 1999). A visual comparison of the true mission data and simulated model is shown in figure 6. Using figure 3, it was estimated that the F 10.7 and Ap indices during 1989 were around 250 and 50 respectively. Therefore, the simulation was run using the ASA High Altitude Atmospheric to account for the extremely prominent space weather activity. A m/A ratio of 40 kg/m^2 was used to create the trajectory shown in Figure 6. ESA (2002) data report that the m/A ratio of the satellite would have been around 200 kg/m^2 . However, the dimensions given of the cylindrical bus do not include the

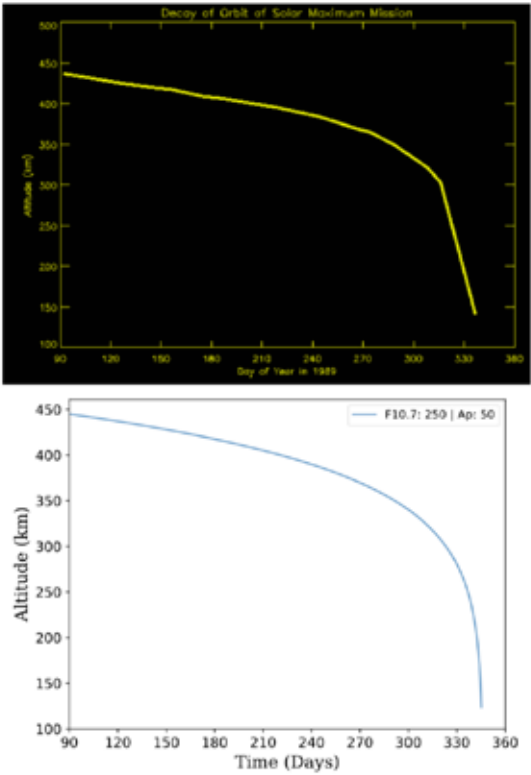


Figure 6. Comparison of the NASA Solar Maximum mission data Kennewell (1999) with orbital decay modeling using identical parameters to the mission characteristics.

large solar panels which would cause significant drag. No dimensions pertaining to the solar panels were able to be found. Therefore, more analysis must be conducted to confirm the validity of the model’s calculations.

Lifetime Calculations

A second useful visualization of the orbital decay calculations is to view satellite lifetime as a function of initial altitude. These graphs can be then used as a comparison between many possible orbital trajectories when mission planning or collecting data. Figure 7 is a recreation of real mission data presented in figure 10 using results obtained from the orbital decay model. Due to the widely varying test articles in

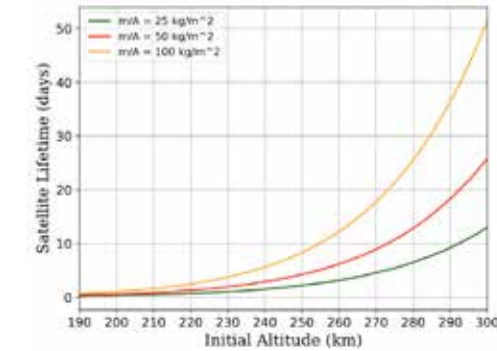


Figure 7. Replication of experimental data plot in figure 10. Data points are based on known orbital decay times of Soviet launch vehicle stages in the 1980s (Kennewell 1999). The results shown are using the NASA stratospheric density model.

Figure 10, the orbital decay calculations to agree with the known data points. Given that most of the articles in figure 10 were cylindrical launch vehicles, it can be assumed that the model will be most accurate for satellites of similar shapes.

An extension of the lifetime visualization technique is shown in figure 8. Here, the ASA High Altitude Atmospheric model calculations are shown as dotted lines. These can be regarded as an approximate uncertainty of the possible trajectories. The F10.7 and Ap measurements in each model are [80,100] and [12,14] respectively. One notable feature of the plot is the exponential relation between initial altitude and satellite lifetime. Although our atmospheric models are only rated for altitudes < 500 km, an extrapolation of the curves would suggest that high earth orbiting satellites have a nearly indefinite orbital lifetime. For this reason, it is evident that orbital debris above 400 km pose a serious threat to contaminating the orbital space. Another important takeaway from Figure 8 is how the m/A ratio differentiates the exponential curves drastically as initial altitude increases. This means that more massive spacecraft such as communication satellites left in orbit will require significant retrograde burns to de-orbit the satellite in a timely manner. However, CubeSats, which normally do not possess a propulsive unit, will require significantly less time to de-orbit.

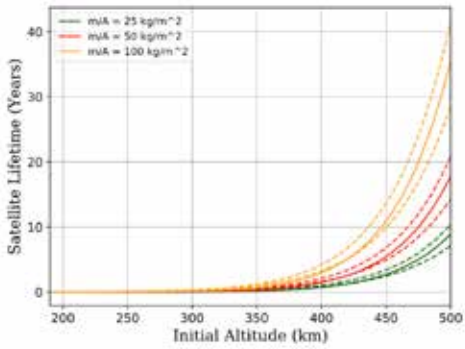


Figure 8. A lifetime projection visualization for satellites with various initial altitudes and m/A ratios using the NASA stratospheric model. The qualitative uncertainty on the model, illustrated by dotted lines, is generated using the ASA atmospheric model which takes into account space weather conditions.

3U CubeSat Case Study

The final portion of the model’s analysis will focus on a case study of an upcoming CubeSat mission to illustrate the model’s usefulness in a mission planning environment. The CubeSat mission of interest is the AERO mission led by an interdisciplinary team at the MIT Haystack Observatory. AERO is a 3U CubeSat aimed to study the auroral regions of the Earth in the radio frequency using the novel “Vector” sensor. The mission is set to launch in 2022 as a secondary payload on a launch vehicle. Therefore, as in many CubeSat missions, the orbital insertion altitude is uncertain. However, when mission planning, it is helpful to gauge potential science objectives and technology demonstrations based on an expected lifetime of the spacecraft. With this in mind, the orbital decay model can be used to visualize a range of mission lifetimes based on potential initial alti-

tudes. The results of this simulation are shown in figure 9. The figure includes a variety of atmospheric models to give a sense for the uncertainty in the mission lifetime. If the goal is to have a mission lifetime of no less than 100 days, the model predicts that an initial altitude of 375 km is needed. A list of the minimum orbital altitude needed for a variety of mission lifetimes is detailed in table 1.

Table 1. Model determined relationships between mission lifetimes and initial orbital altitudes.

100 days	365 km
200 days	400 km
365 days	430 km
1000 days	480 km

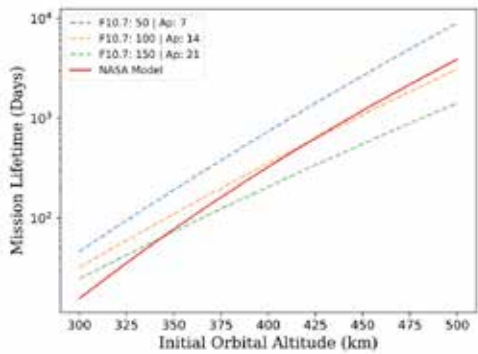


Figure 9. Predicted mission lifetimes of a 3U CubeSat in LEO based on the upcoming AEROVISTA mission. The m/A is taken to be 30, the standard for a 3U CubeSat.

Model Limitations and Future Studies

Model Limitations and Recommendations

While the model has proven to be a useful guide to estimating orbital decay trajectories, there are additional measures which can be taken in future versions of the model which will increase the precision, accuracy, and usefulness of the calculations.

Step Size

Decreasing the step size is a simple change to the simulations which could increase the precision of the calculations. Currently, the step size is determined by the orbital period of the respective revolution. Instead, using fractions of the orbital period would increase the precision while keeping the precision constant across calculations. In order to figure out if this is worth the increase in computing time, further studies are needed.

Circular Orbits

In the calculations, it is assumed that the orbit of the spacecraft in LEO is circular. In reality, the orbits of spacecraft are in the shape of an ellipse with an apoapsis and periapsis. As a result, the drag experienced due to atmospheric density would not be constant throughout the period of the orbit. A better representation of the true loss in mechanical energy would account for the different atmospheric densities. A possible solution to

this would be integrating the atmospheric density function over a range of heights to find the average density experienced by the spacecraft.

Aerodynamic Considerations

As mentioned in section 3.2, the drag coefficient, Cd, was estimated using existing mission data. While it was an effective measure for tuning the trajectory estimations, a more rigorous determination of the Cd is needed for more accurate calculations and describe a wider variety of geometric objects. An investigation of a function used to determine the constant’s value for a range of spacecraft would most likely require extensive aerodynamic research. Additionally, the calculations do not consider that the spacecraft may experience lift forces in the denser parts of the atmosphere resulting in longer orbital decay times. This, too, would be a parameter best investigated by a researcher with more aerodynamic experience.

Program Interface and Output

The model is currently composed of various functions written in Python 3. For more general use, a better software front end would allow the model to be more easily used. Options for additional visualization techniques would enhance the model’s usefulness in an educational and research setting. One visualization idea is to allow for formal printouts of important data determined by the model. For instance, a two-column chart recording the time taken to decline 25 km in altitude. In an educational setting, a 3-D animation of the orbital decay through time would provide an intriguing and easy-to-understand visualization.

Future Studies

This paper has only investigated Earth’s atmospheric conditions on satellites in LEO. However, with appropriate atmospheric density models, the same calculations could be made for a range of planetary bodies. Further work may also adapt the model for spacecraft entering an atmosphere from interplanetary travel. This would be useful in the active research field of trajectory design where aerobraking is used to capture a spacecraft within a potential well.

Concluding Remarks

Orbital decay calculations are an essential tool for any work in the LEO space. As Earth’s orbital space becomes increasingly accessible, reliable modeling of decay trajectories will be needed for defunct spacecraft and new mission planning. The novel orbital decay model presented was proved a useful measure to approximate the orbital trajectories in LEO. A significant advantage of the model is the ability to account for space weather conditions and provide a qualitative error on the timeline. Visualizations of the simulations can be presented in either single trajectory or lifetime predictions which were proved both useful measures in mission planning and analysis. The basis of the orbital model will be a useful tool for more challenging problems such as aerobraking and interplanetary travel.

Appendix

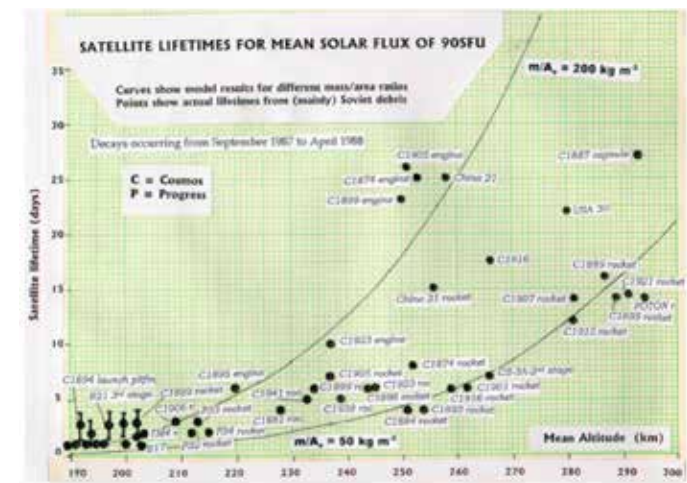


Figure 10. Lifetimes for various pieces of (mostly Russian) space, as a function of their initial altitude. These decays occurred over a few months when the geomagnetic field was relatively quiet and the solar radio flux had a mean value of 90 SFU. The model curves for m/A_e ratios of 50 and 200 are also drawn on the graph. Notice that the rocket engines cluster around the $m/A_e=50$ curve. These objects, devoid of fuel, are relatively “light.” The engines, on the other hand, are much “heavier” (Kennewell 1999).

References
ESA. 2002.
<https://earth.esa.int/web/eoportal/satellite-missions/s/smm>.

Garcia, M. 2015, “Space Debris and Human Spacecraft,” NASA.
<https://www.nasa.gov/missionpages/station/news/orbitaldebris.html>

Gavrilyeva, G., and Ammosov, P. 2018, Atmospheric Chemistry and Physics, 18, 3363, doi: 10.5194/acp-18-3363-2018.

Glenn. 2015a, The Drag Equation, NASA.
<https://www.grc.nasa.gov/www/k-12/airplane/drageq.html>
—. 2015b, Earth Atmosphere Model - Metric Units, NASA.
<https://www.grc.nasa.gov/WWW/K-12/airplane/atmosmet.html>.

Kennewell, J. 1999, Satellite Orbital Decay Calculations, IPS Radio Space Services.

About the Author

Drew Langford is an honors track physics major with concentrations in astrophysics, applied physics, and advanced physics. He is a Class of 2022 CUSE Sorin Scholar and 2021 Goldwater Scholar. Langford’s undergraduate research has focused on the dynamics of mass transfer between binary stars and the scientific operations of research small satellites. After graduating from Notre Dame, Langford intends to pursue graduate school in astrodynamics, studying multi-body dynamical systems such as binary stars and the Earth-Moon system.

Fluorinated Compounds in Fast Food Packaging

Molly DeLuca

University of Notre Dame, Department of Physics

Abstract

This study utilized particle-induced gamma-ray emission spectroscopy to identify the presence of fluorine in food contact materials. Fluorination typically indicates the presence of per- and polyfluoroalkyl substances (PFAS) which are carcinogenic and nonbiodegradable compounds typically employed as water- or grease-proofing agents. Fifty-six food paper and thin paperboard samples from national fast food chains located in the Mishawaka area were irradiated under a 4 MeV proton beam generated by the University of Notre Dame’s St. Andre 3 MV Tandem Accelerator. Nine of the 56 samples contained elevated levels of fluorine, a marked decrease from the last comprehensive survey of PFAS in fast food packaging in 2017 which found 46% of food contact papers and 20% of thin paperboard samples to be fluorinated. Although preliminary, these results suggest a market-wide shift among fast food retailers toward unfluorinated packaging alternatives. This trend, in tandem with a recent increase in legislation regulating PFAS use in consumer product, highlight the role that scientific investigation can play in galvanizing public support for driving change at the corporate level.

Introduction

Per- and polyfluoroalkyl substances (PFAS) are a class of synthetic chemicals characterized by a fluorinated carbon backbone with attached functional groups that distinguish the 4,700+ PFAS variants. These chemicals are effective and long-lasting waterproofing agents due to the strong hydrophobic and lipophobic properties that result from their alkyl tails, and as such have been employed in a myriad of products, in particular nonstick cookware, weather-treated textiles, and grease-proof food packaging materials (1).

Because of their tight fluorine-carbon bond, PFAS are extremely thermally and chemically stable. This inhibits natural biodegradation, leading to an accumulation of these chemicals in soil and water, as well as human tissues. Long-chain PFAS refer to perfluorocarboxylic acids (PFCAs) with a backbone of C8+ (8 or more linked carbon atoms), perfluoroalkane sulfonic acids (PFSA) with a carbon chain of C6+, as well as any precursors of these substances.

The PFCA perfluoronic acid (PFOA) and PFSA perfluorooctane sulfonate (PFOS) are two long-chain PFAS variants with human half-lives of 3+ years that have been linked to a myriad of health conditions including thyroid, reproductive, immune, and developmental disorders as well as testicular and kidney cancers (2).

Motivated by the growing body of evidence connecting long-chain PFAS to adverse health effects, most U.S. manufacturers voluntarily phased out production of PFOS, PFOA, and most long-chain PFAS chemicals between 2000 and 2015, replacing them with short-chain alternatives that were not, at

the time, understood to be carcinogenic or bioaccumulative (3).

However, emerging research into short-chain (SC) PFAS indicates that structural similarities to their long-chain counterparts raise similar health and environmental concerns. SC-PFAS have human half lives of weeks to months. In particular, the 6:2 fluorotelomer alcohol, a common degradation product of short-chain PFAS commonly utilized in food contact materials, demonstrates toxic and bioaccumulative effects similar to long-chain PFAS. Moreover, short-chain PFAS have shown higher migration efficiencies into foods when used in food contact materials (4).

PFAS in food packaging is particularly concerning as it provides a direct pathway to human consumption. In these materials, PFAS molecules are typically not polymerized but rather are attached as “sidechains” to non-PFAS polymerized molecules in order to create a surface water- and grease-proof layer. Because these agents are applied at lower temperatures, smaller PFAS molecules are not removed in the production process but can detach and migrate to enclosed food when the material is exposed to heat and grease—conditions almost ubiquitous in the practical use of fast food wrappers and paperboard (5,6).

In 2017, Laurel Schaider, a research scientist at the Silent Spring nonprofit research organization, led an investigation into PFAS in food packaging and published the largest, most comprehensive study to date on the topic. This investigation analyzed 400+ food contact materials collected in 2014 and 2015 from 27 national fast food restaurants using a novel application of particle-induced gamma-ray emission (PIGE) spectroscopy as a rapid screening technique for fluorine and solvent extraction and liquid chromatography/high-resolution mass spectrometry analyses to confirm that fluorine signatures indicated the presence of PFAS. This study detected fluorine in 46% of food contact papers (i.e., wrappers, pastry bags) and 20% of thin paperboard materials (i.e., French fry boxes).

Liquid chromatography mass spectrometry (LC-MS) analyses were performed on a subset of 20 samples in order to identify the compounds responsible for elevated fluorine levels. These analyses revealed the presence of the long-chain PFOA (supposedly phased out of production beginning in 2000) and the 6:2 fluorotelomer alcohol. (7)

Following the 2017 study, many fast food chains claimed to not have been aware that their packaging products contained PFAS and pledged to eliminate the chemicals from their packaging and utilize unfluorinated alternatives.

This study revisits the question of PFAS in fast food packaging, analyzing paper and thin paperboard samples from national fast food chains located in the Mishawaka area in order to see if growing awareness about PFAS human and environmental toxicity has decreased their prevalence in fast food packaging.

Materials, Methods

Ion Beam Analysis Background

Fluorine detection via proton-induced gamma-ray emission (PIGE) spectroscopy exploits isotopic-specific wavelengths of the gamma rays emitted in nuclear scattering

(p, p'γ) reactions that occur when a sample is bombarded with a beam of protons. The gamma-ray peaks of 110 and 197 keV correspond to fluorine (Figure 1) and have large cross-sections that do not interfere with other elemental signatures (8). While the spectroscopic technique is isotope specific, fluorine is a monoisotopic element and therefore the signal is indicative of all elemental fluorine. Fluorine content is calculated by numerical integration of the peaks. Each sample was irradiated with ~50nA of 4 MeV protons for 180 seconds. Two replicates were analyzed from each of the two sample sets in order to confirm the accuracy of measured fluorine counts. The ion beam penetrates solid materials up to 100–200 microns so it is likely that the beam completely penetrated the paper samples and the side of the sample exposed to the beam was not taken into consideration. Because the thin paperboard samples are much thicker, it is likely that the beam does not completely penetrate the sample. Therefore, the side in direct contact with food was exposed to the beam in order to get the most accurate sense of potential fluorine exposure that would result from contamination of enclosed food.

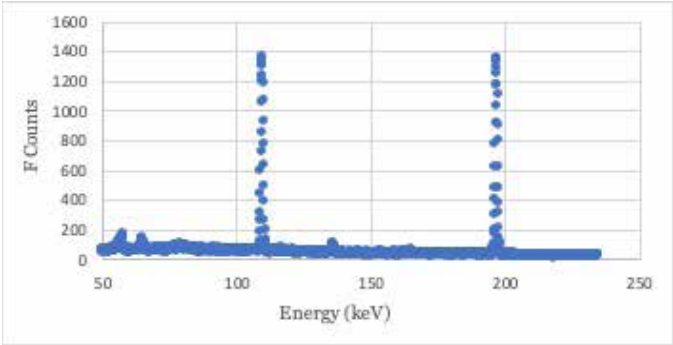


Figure 1: Gamma ray spectrum resulting from PIGE analysis of a 1,000 ppm sodium fluoride in cellulose standard. The peaks at 110 and 197 keV are characteristic of fluorine and indicate the element’s presence within the sample.

Sample Collection

Fifty-six samples were collected from large fast food chain restaurants (100+ U.S. establishments) located in the Mishawaka area. Twenty-nine samples were collected in January 2021 and 27 in February 2021. Although the samples collection was restricted to restaurants in a relatively small geographic area, the national scope of the establishments selected supports the conclusion that these results are representative of the food packaging materials utilized in the broader market. Samples were restricted to papers (sandwich/burger wrappers, pastry bags, bakery sheets) and thin paperboards (french fry boxes, popcorn containers, nugget boxes, soup containers) that are utilized in direct food contact applications. In order to prevent fluorine contamination among samples, each sample was immediately stored in a separate zip-lock bag.

Target preparation

Squares of roughly 2x2 cm were cut from samples and manually adhered to a stainless-steel target frame with hole

of 1 cm diameter with masking tape. The majority of samples had not been utilized in food contact applications and thus did not contain any food residue. In the instances of previous food contact applications, the analyzed piece was selected from a portion of the material that was free of any visible stains or residue.

Standards and Normalization

Both PIGE and PIXE are comparative measurements with fluorine count measurement that fluctuate daily with the intensity, energy, and tune of the beam. To allow for accurate comparison of fluorine content across days, each set of samples is preceded by a set of calibration standards treated with stock solutions of 0, 250, 500, and 1,000 ppm sodium fluorine in cellulose. A linear regression applied to the graph of measured F counts vs. known ppm allows for the conversion of measured counts to ppm F.

Moreover, because bombardment of the samples occurs ex-vacuo, discharged ions in the atmosphere can alter beam intensity and angular resolution, causing fluctuations in measured fluorine across samples. Atmospheric argon is used as a normalizing element due to its abundance in the atmosphere, as well as its general absence in food packaging. Measurements of the gamma rays released due to the argon (p, nγ) reaction provide insight into how beam fluctuations and transmission to target are biasing measured fluorine counts (9).

Results

Figure 2 summarizes the experimental data collected. Out of 56 samples, 9 contained levels of fluorine above the daily level of detections with concentrations ranging from 207 to 1,466 ppm F. Samples with fluorine concentrations between 200 and 500 ppm F are characterized as low fluorine, and samples with fluorine concentrations of 500 ppm and greater are considered high fluorine. High fluorine content indicates intentional fluorination while low fluorine could be the result of environmental contamination or fluorine unintentionally entering the production or recycling processes. Forty-seven of the samples were unfluorinated or contained levels of fluorine that were below the daily level of detection, six of the 56 samples (10%) contained low but quantifiable fluorine concentrations, and three of the 56 samples (5.3%) contained high fluorine concentrations.

Seven of the 9 samples with elevated levels of fluorine were thin papers that are utilized for serving hot food (burgers, breakfast sandwich, warmed pastries, pizza); two of the 9 fluorinated samples were thin paperboard materials utilized for serving hot (but not liquid) foods. Blank samples included sandwich wrappers, soup containers, and bakery sheets for pastries that were not warm. The types of fluorinated samples indicate that PFAS is predominantly utilized as a grease-proofing agent.

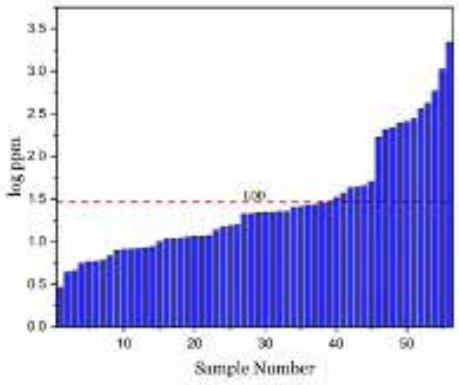


Figure 2: Summary of experimental data; samples presented in order of increasing fluorine concentration (ppm). The red line delineates the limit of detection (LOD), the lowest concentration of fluorine that can be accurately identified within a sample. Fluorine concentrations of ~3x the LOD typically reflect intentional fluorination.

Discussion

The results of this study identified elevated fluorine levels in 16% of paper and thin paperboard fast food packaging samples and suggests that fluorination of food contact products has decreased over the past five years. The 2017 national survey detected fluorine in ~33% of samples (20% in thin paperboard and 46% in food contact papers).

This decrease in overall fluorination levels indicates a market-wide movement toward alternative grease and water-proofing methods in food packaging materials. Moreover, even though multiple samples were collected from most locations, only one restaurant had multiple samples with elevated fluorine levels. In the 2017 study, fluorination was more consistent within sample types (e.g., burger wrappers at multiple locations were fluorinated) and within retailers. The variability in type of fluorinated samples and fluorination levels within specific retailers suggests that fast food chains as an industry are in the process of converting to packaging that does not contain PFAS.

Although PIGE spectroscopy provides an effective and efficient means of detecting elevated fluorine levels, it serves only as a screening mechanics and does not reveal the source of fluorine signatures. The next step in this investigation will be to perform an LC/MS analysis on the samples that had elevated fluorine levels. LC/MS would both confirm the results of the PIGE analysis as well as identify the specific PFAS analytes responsible for elevated fluorine levels, providing insight into where and why these fluorinated compounds are entering the production process. Long-chain PFASs (such as PFOA or PFOS) that were phased out by U.S. manufacturers between 2000 and 2015 would suggest residual PFAS from discarded or recycled products while short-chain PFAS and byproducts such as the 6:2 fluorotelmer alcohol would indicate intentional fluorination.

The use of PFAS in food packaging products has environmental ramifications and potential for human exposure that extend well beyond the food directly enclosed. Although

fast food consumption has been linked to elevated PFAS levels in blood, the most urgent and severe public health threat from PFAS in food packaging lies in the environmental buildup that occurs after products are disposed. The same strong, stable F-C bond that results in their long human half-lives prevents biodegradation and causes PFAS to build up in the environment after packaging has been discarded. Elevated PFAS levels in water and soil can enter the food chain and result in indirect human exposure. Animals—particularly in marine systems—that are exposed to PFAS contaminated soil and water accumulate PFAS in their tissues that is passed on to humans and other organisms that consume them. Because of their long half-lives within organisms, long-chain PFAS such as PFOA and PFOS are typically associated with this type of exposure.

Fruits and vegetables that are planted in contaminated soil and/or irrigated with contaminated water bioaccumulate PFAS, preferentially taking up the short-chain PFAS that are more prevalent in consumer products. These PFAS also are passed on to the organisms that consume these plants and proceed up the food chain to humans. Because of their toxicity and environmental persistence, PFAS pose a unique and powerful threat to human and ecological health that warrants immediate attention.

The widespread movement away from the use of these chemicals in consumer products lies at the intersection of science and policy. As scientific study continues to uncover the health dangers associated with PFAS exposure, an informed public can hold corporations accountable through a combination of selective patronization and regulatory legislation. Moreover, continued support for research into the development of waterproofing chemicals that biodegrade naturally after use will ameliorate the environmental degradation that occurs after products have been discarded.

In July 2020, the FDA announced a voluntary market phase-out of food contact materials that utilize the 6:2 fluorotelomer alcohol as a grease-proofing agent that will occur over a three-year period beginning in January 2021 (10). Additionally, New York, Maine, and Washington all have passed legislation banning PFAS in food contact materials (11). However, the decreased prevalence of fluorinated food contact materials observed in this study suggests that, even in the absence of legal enforcement, increased public awareness regarding the health and environmental dangers presented by PFAS has resulted in a market-wide movement toward unfluorinated packaging materials.

References

“Basic Information on PFAS.” EPA, Environmental Protection Agency, 14 Jan. 2021, www.epa.gov/pfas/basic-information-pfas.

Olsen Geary, W., Burris Jean, M., Ehresman David, J., Froehlich John, W., Seacat Andrew, M., Butenhoff John, L., et al. (2007). Half-life of serum elimination of perfluorooctanesulfonate,perfluorohexanesulfonate, and perfluorooctanoate in retired fluorochemical production workers. Environmental Health Perspectives, 115(9), 1298-1305. doi:10.1289/ehp.10009

Fact Sheet: 2010/2015 PFOA Stewardship Program; U.S. Environmental Protection Agency: Washington, DC, http://www.epa.gov/assessing-and-managing-chemicals-under-tsca/fact-sheet-20102015-pfoa-stewardship-program

Rice, P. A., Aungst, J., Cooper, J., Bandele, O., Kabadi, S. V. (2020). Comparative analysis of the toxicological databases for 6:2 fluorotelomer alcohol (6:2 FTOH) and perfluorohexanoic acid (PFHxA). Food and Chemical Toxicology, 138, 111210. doi:https://doi.org/10.1016/j.fct.2020.111210

Yuan, G.; Peng, H.; Huang, C.; Hu, J. Ubiquitous occurrence of fluo-rotelomer alcohols in eco-friendly paper-made food-contact materials and their implication for human exposure. Environ. Sci. Technol. 2016, 50 (2), 942– 950, DOI: 10.1021/acs.est.5b03806

Xu Y, Noonan GO, Begley TH. Migration of perfluoroalkyl acids from food packaging to food simulants. Food Addit Contam Part A Chem Anal Control Expo Risk Assess. 2013;30(5):899-908. doi: 10.1080/19440049.2013.789556. Epub 2013 May 24. PMID: 23701306.

Schaidler, L. A.; Balan, S. A.; Blum, A.; Andrews, D. Q.; Strynar, M. J.; Dickinson, M. E.; Lunderberg, D. M.; Lang, J. R.; Peaslee, G. F. Fluorinated compounds in U.S. fast food packaging. Environ. Sci. Technol. Lett. 2017, 4, 105– 111, DOI: 10.1021/acs.estlett.6b00435

Ritter, E. E.; Dickinson, M. E.; Harron, J. P.; Lunderberg, D. M.; DeYoung, P. A.; Robel, A. E.; Field, J. A.; Peaslee, G. F, PIGE as a screening tool for per-and polyfluorinated substances in papers and textiles. Nucl Instr Meth 2017, B407, 47-54.

Wilkinson, J. T., McGuinness, S. R., & Peaslee, G. F. (2020). External beam normalization measurements using atmospheric argon gamma rays. Nuclear Instruments and Methods in Physics Research Section B: Beam Interactions with Materials and Atoms, 484, 1-4. doi:https://doi.org/10.1016/j.nimb.2020.10.007

“FDA Announces Voluntary Agreement with Manufacturers to Phase Out Certain Short-Chain PFAS Used in Food Packaging.” U.S. Food and Drug Administration, FDA, www.fda.gov/news-events/press-announcements/fda-announces-voluntary-agreement-manufacturers-phase-out-certain-short-chain-pfas-used-food

Hoylman, B. (2020, December 03). New York Bans Dangerous, INDESTRUCTIBLE ‘FOREVER Chemicals’ from pizza boxes and other food packaging. Retrieved February 16, 2021, from https://www.nysenate.gov/newsroom/press-releases/brad-hoylman/new-york-bans-dangerous-indestructible-forever-chemicals-pizza

About the Author

Molly DeLuca is a junior at Notre Dame majoring in physics with a concentration in advanced physics and a minor in history. She is a Trustey Family Scholar and a member of the Glynn Family Honors Program, and her research was conducted in Notre Dame’s Nuclear Science Laboratory under the supervision of Professor Graham Peaslee. Her work within the Peaslee research group utilizes ion beam analysis techniques to detect per-and polyfluorinated compounds. After graduation, DeLuca hopes to attend a physics Ph.D. program and pursue a career at the intersection of applied physics and public service.

Zeros of Riemann Zeta Function

Yuxin Lin

University of Notre Dame, Department of Mathematics

Abstract

In this paper we show how some properties of Riemann zeta function lead to the proof of the Prime Number Theorem, the Prime Ideal Theorem, and Chebotarev’s density theorem. We then introduce some results related to Riemann Hypothesis, and Artin’s conjecture as a corollary of Generalized Riemann Hypothesis.

1 Introduction

The Prime number Theorem is a theorem about the distribution of primes. At the first glance primes appear to behave quite wildly. However, the Prime Number Theorem says that the distribution can be described by an asymptotic formula. A more stunning fact is that the proof of the Prime Number Theorem relies heavily on the zero locations of the Riemann zeta function. The fact that Riemann zeta function doesn’t have a zero on $\text{Re}(s) = 1$ is the most crucial step in the proof of the Prime Number Theorem. We will also see that an similar property of $L(s, \chi)$ for χ a character on $\text{Gal}(K/\mathbb{Q})$ leads to the proof of the Prime Ideal Theorem, a generalization of the Prime Number Theorem to general fields.

The original proof of Chebotarev’s density theorem requires extensive use of Galois theory, and doesn’t appear to be similar at all to the Prime Number Theorem. Here we present a classical alternative proof of Chebotarev in which Chebotarev’s density theorem in abelian field extensions is presented as a simple corollary of the non-zero property of $L(s, \chi)$ on $\text{Re}(s) = 1$, and Chebotarev’s density theorem for non-abelian field extensions can be obtained as a corollary by considering the non-zero property of the generalized $L(s, \chi)$ series, which is the Artin L series.

From the proof of the Prime Number Theorem and the Chebotarev Density Theorem we can guess intuitively that if we have more control of where the zeros of $\zeta(s)$ are, we can obtain a more precise estimation of density of primes. So in the second half of the paper, we will focus on getting more information about the zero location of zeta function. Firstly we extend the $\zeta(s)$ to the entire complex plane and present some results about the zeros of $\zeta(s)$. We also illustrate Riemann’s original proof of the functional equation, which gives the symmetricity of the zeros. After getting these fundamental results, we cite the Von Mangoldt’s formula of $\psi(x)$, from which we can see that the error bound of $\psi(x)$ depends entirely on the zeros of $\zeta(s)$. Since $\psi(x)$ and $\pi(x)$ differ by very little, to minimize the error bound of $\pi(x)$ is equivalent to minimize the terms contributed by the zeros of zeta function. The symmetricity of zeros determines that to least error bound is obtained when all the critical zeros of Riemann zeta function are on $\text{Re}(s) = \frac{1}{2}$, which is the Riemann Hypothesis. Assuming the Riemann Hypothesis and then following almost the same procedure as the proof of asymptotic formula of the Prime number Theorem, we can show that the Riemann Hypothesis gives the desired error bound of the prime counting function. We also have the Generalized Riemann Hypothesis, which is to assume the distribution of zeros of the Dedekind zeta function. At the end we present an application of the Generalized Riemann Hypothesis. The role of the Generalized Riemann Hypothesis here is to gives more room for the estimation so that the error won’t blow up.

The required group theory and Galois theory background is listed in section 2. Section 3 will introduce the Riemann zeta function and prove the Prime Number Theorem, and section 4 will introduce Artin L-functions and prove the Prime Ideal Theorem and Chebotarev’s density theorem. Section 5 will introduce some results related to the zeros of $\zeta(s)$ and how the Riemann Hypothesis leads to its number theoretical equivalence. Section 6 introduces Artin’s Primitive Root conjecture, which can be proven assuming the Generalized Riemann Hypothesis.

2 Background

2.1 Basic representation theory

Definition 2.1. Let V be a vector space over a field F , and G be a finite group. A representation of G on V is a homomorphism $\rho := G \rightarrow GL(V)$. We say that ρ_1, ρ_2 are isomorphic if there exists some matrix M such that $M\rho_1M^{-1} = \rho_2$.

We say the dimension of ρ is the dimension of V . Consider the ring $F[G]$, consists of $\sum_{i=1}^n a_i g_i$ with $a_i \in F$ and $g_i \in G$. This ring acts on V by

$$(\sum_{i=1}^n (a_i g_i)) \cdot v = \sum_{i=1}^n a_i (\rho(g_i) v)$$

So V can be regarded as an $F[G]$ module. So representation of G gives $F[G]$ modules. Conversely if we have a $F[G]$ module V then it’s a vector space over F . Every $g \in G$ acts on V as a linear transformation by scalar multiplication, so define $\rho(g)$ to be this transformation in $GL(V)$. ρ is then a representation of G . Therefore, we have the correspondence:

$F[G]$ module $V \iff \rho : G \longrightarrow GL(V)$
And this turns out to be a bijection. We say that V as a module affords the representation ρ of G .

We make the correspondence in order to state the following definition:

Definition 2.2. A representation ρ is irreducible if and only if the $F[G]$ module that affords it is irreducible. That is, the only submodules of $F[G]$ are 0 and V .

In terms of vector space, ρ is irreducible if V doesn’t have a G -stable subspace. That is, no subspace $V' \neq V$ has $gV' \subseteq V' \ \forall g \in G$.

Definition 2.3. Given a representation $\rho : G \rightarrow GL(V)$, the character of ρ is the map $\chi_\rho : G \longrightarrow F$ such that $\chi(g) = \text{Trace}(\rho(g))$.

We say a character χ_ρ is irreducible if ρ is irreducible representation. All representation of G are one dimensional iff G is abelian because $GL(V)$ is no longer commutative when the dimension of $V \geq 2$

Also notice that χ_ρ is the same for isomorphic presentations because trace is a invariant under matrix conjugation. This means that χ_ρ lands in the following category of functions:

Definition 2.4. A class function is any map $f : G \longrightarrow \mathbb{C}$ such that $f(g^{-1}xg) = f(x)$, $\forall x, g \in G$

- The followings are some facts that we are going to use.
- $\chi_{\rho_1} = \chi_{\rho_2}$ iff ρ_1 and ρ_2 are isomorphic representations. So the character determines the representation up to isomorphism.
 - For a group G , the number of irreducible characters equal the number of conjugacy classes of G .
 - Irreducible characters span the space of class functions. So every class function on G can be written as linear combination of irreducible characters.
 - (Orthogonality of characters) Define the inner product of two class functions ϕ and ψ on G as:

$$\langle \phi, \psi \rangle_G = \frac{1}{|G|} \sum_{g \in G} \phi(g) \overline{\psi(g)}$$

Then let $\chi_1, \chi_2, \dots, \chi_g$ be the irreducible characters of G . For any class function $f = \sum a_i \chi_i$, $\langle f, \chi_i \rangle = a_i$. In particular, the inner product of two different irreducible characters is zero.

The proof of all the above facts can be found in the section 18.1 and 18.3 of [9].

2.2 One dimensional representation

We just mentioned that G is abelian iff all its irreducible representations are 1-dimensional. In this special case, we can ignore the distinction between the representation and character, and call both of them as the character of G .

Definition 2.5. A character of a finite abelian group G is a homomorphism $\chi : G \rightarrow \mathbb{C}^*$. Let \widehat{G} denote the set of all characters of G

The followings are facts about abelian groups G we use. The proofs can be found in the chapter 7 of [10].

- $\widehat{\widehat{G}} \cong G$ (non-canonically)
- (Orthogonality relations of characters)
(1) For $\chi_1, \chi_2 \in \widehat{G}$, we have

$$\sum_{g \in G} \chi_1^{-1} \chi_2(g) = \begin{cases} |G|, & \text{if } \chi_1 = \chi_2 \\ 0, & \text{if } \chi_1 \neq \chi_2 \end{cases}$$

- (2) For $\sigma, \tau \in G$, we have

$$\sum_{\chi \in \widehat{G}} \chi(\sigma^{-1} \tau) = \begin{cases} |G|, & \text{if } \sigma = \tau \\ 0, & \text{if } \sigma \neq \tau \end{cases}$$

2.3 Induced representation and Frobenius reciprocity

Definition 2.6. Let H be a subgroup of G . Let ρ be a representation of H on V . Then the representation of G afforded by $F[G] \otimes_{F[H]} V$ by left-multiplication is the induced representation $\text{Ind}_H^G \rho$ of ρ .

When there is no ambiguity about G and H , we will use ρ^* to denote the character induced by ρ

We can actually write down explicit matrix for $\rho^*(g)$. Let g_1, g_2, \dots, g_m be representatives of left-cosets of H . Then $\rho^*(g)$ can be written as:

$$\begin{bmatrix} \rho(g_1^{-1}gg_1) & \cdots & \rho(g_1^{-1}gg_m) \\ \vdots & \ddots & \vdots \\ \rho(g_m^{-1}gg_1) & \cdots & \rho(g_m^{-1}gg_m) \end{bmatrix}$$

Where $\rho(g_i^{-1}gg_j)$ is the zero matrix whenever $g_i^{-1}gg_j \notin H$. This is obtain by considering the action of g on the basis of $F[G] \otimes_{F[H]} V$.

From this matrix we get the induced character

$$\chi_{\rho^*}(g) = \sum_{g_i^{-1}gg_i \in H} \chi_{\rho}(g_i^{-1}gg_i) = \frac{1}{|H|} \sum_{x \in G} \chi_{\rho}(x^{-1}gx)$$

The proof can be found in the section 19.3 of [9]. Now we state an important theorem about restriction and induction of characters.

Theorem 2.7 (Frobenius reciprocity). Suppose H is a subgroup of G , and let ψ, ϕ be two class functions such that $\psi: G \rightarrow \mathbb{C}$ and $\phi: H \rightarrow \mathbb{C}$. Then we have

$$\langle \phi, \text{Res}_H^G \psi \rangle_H = \langle \phi^*, \psi \rangle_G$$

where $\text{Res}_H^G \psi$ means restricting ψ to H .

The proof can be found in [12]

2.4 The Decomposition and Inertia groups

Let L/K be number field extension. Let \mathcal{O}_K denote the ring of integer of K and \mathcal{O}_L denote the ring of integer of L . For \mathfrak{p} a prime ideal of K , consider the prime decomposition of $\mathfrak{p}\mathcal{O}_L$. say

$$\mathfrak{p}\mathcal{O}_L = \prod_{i=1}^k \mathcal{P}_i^{e_i}$$

where \mathcal{P}_i are prime ideals of \mathcal{O}_L . We define e_i to be $e(\mathcal{P}_i|\mathfrak{p})$.

Definition 2.8. $\mathfrak{p} \subseteq \mathcal{O}_K$ is called unramified in L if $e(\mathcal{P}_i|\mathfrak{p}) = 1$, $\forall i$. Otherwise \mathfrak{p} is ramified.

Also, for a prime ideal $\mathcal{P} \in \mathcal{O}_L$, we denote the absolute norm of \mathcal{P} as $|\mathcal{P}| = |\mathcal{O}_L/\mathcal{P}|$. Notice norm of a prime ideal is a power of the rational prime below \mathcal{P} . It's a fact that $\mathcal{O}_L/\mathcal{P}_i$ is a field extension of $\mathcal{O}_K/\mathfrak{p}$. We denote the degree of extension of residue fields $[\mathcal{O}_L/\mathcal{P}_i : \mathcal{O}_K/\mathfrak{p}]$ as $f(\mathcal{P}_i|\mathfrak{p})$. It is known that

$$\sum_{i=1}^k e(\mathcal{P}_i|\mathfrak{p})f(\mathcal{P}_i|\mathfrak{p}) = [L : K]$$

Now if L/K is Galois, let G denote $\text{Gal}(L/K)$. Then $e(\mathcal{P}_i|\mathfrak{p})$ and $f(\mathcal{P}_i|\mathfrak{p})$ are all equal since $\mathcal{P}_i = \sigma\mathcal{P}_j$ for some $\sigma \in G$. Then let $e = e(\mathcal{P}_i|\mathfrak{p})$, $f = f(\mathcal{P}_i|\mathfrak{p})$. We have $kfe = |G|$. \mathfrak{p} ramifies in \mathcal{O}_L iff $\mathfrak{p} \mid \text{disc}(L/K)$, so there are only finitely many ramifying primes in \mathcal{O}_K . The proof is found in the chapter 3 of [10]

Definition 2.9. A prime $\mathfrak{p} \in \mathcal{O}_K$ is defined as splits completely in \mathcal{O}_L iff $e(\mathcal{P}_i|\mathfrak{p}) = f(\mathcal{P}_i|\mathfrak{p}) = 1$

In this paper we always assume L/K is Galois if not specified otherwise.

Definition 2.10. Define the decomposition group $D(\mathcal{P}_i|\mathfrak{p})$ of \mathcal{P}_i as

$$D(\mathcal{P}_i|\mathfrak{p}) = \{\sigma \in G \mid \sigma\mathcal{P}_i = \mathcal{P}_i \forall \alpha \in \mathcal{O}_L\}.$$

We can check it is a subgroup of G .

Definition 2.11. Define the inertia group of \mathcal{P}_i as $E(\mathcal{P}_i|\mathfrak{p})$ such that

$$E(\mathcal{P}_i|\mathfrak{p}) = \{\tau \in G \mid \tau\alpha \equiv \alpha \pmod{\mathcal{P}_i} \forall \alpha \in \mathcal{O}_L\}$$

We can check that $E(\mathcal{P}_i|\mathfrak{p})$ is a subgroup of $D(\mathcal{P}_i|\mathfrak{p})$.

Now consider $\mathcal{O}_L/\mathcal{P}_i$. For $\sigma \in D(\mathcal{P}_i|\mathfrak{p})$, it can also be regarded as acting on the residue field $\mathcal{O}_L/\mathcal{P}_i$ by sending $\alpha \pmod{\mathcal{P}_i}$ to $\sigma(\alpha) \pmod{\mathcal{P}_i}$. This is well defined because σ fixes \mathcal{P}_i . So we have a homomorphism

$$D(\mathcal{P}_i|\mathfrak{p}) \longrightarrow \text{Gal}((\mathcal{O}_L/\mathcal{P}_i)/(\mathcal{O}_K/\mathfrak{p})).$$

The kernel is $E(\mathcal{P}_i|\mathfrak{p})$. It turns out that this map is actually surjective. Thus we have

$$D(\mathcal{P}_i|\mathfrak{p}) / E(\mathcal{P}_i|\mathfrak{p}) \cong \text{Gal}((\mathcal{O}_L/\mathcal{P}_i)/(\mathcal{O}_K/\mathfrak{p})).$$

Also $|E(\mathcal{P}_i|\mathfrak{p})| = e(\mathcal{P}_i|\mathfrak{p})$, and thus we have

$$|D(\mathcal{P}_i|\mathfrak{p})| = e(\mathcal{P}_i|\mathfrak{p})f(\mathcal{P}_i|\mathfrak{p})$$

. The proofs of above facts can be found in the chapter 3 of [10]

2.5 Frobenius elements

Recall that \mathfrak{p} is unramified iff $e(\mathcal{P}_i|\mathfrak{p}) = 1$. Then $E(\mathcal{P}_i|\mathfrak{p})$ is trivial so $D(\mathcal{P}_i|\mathfrak{p})$ is isomorphic to the Galois group of residue fields. However, $\mathcal{O}_L/\mathcal{P}_i/\mathcal{O}_K/\mathfrak{p}$ is extension of finite fields, so its galois group is cyclic. By basic field theory the generator of $\text{Gal}((\mathcal{O}_L/\mathcal{P}_i)/(\mathcal{O}_K/\mathfrak{p}))$ is $\bar{\sigma}$ such that

$$\bar{\sigma}(\bar{\alpha}) = \bar{\alpha}^{|\mathfrak{p}|}$$

where $\bar{\alpha}$ is the reduction of $\alpha \pmod{\mathfrak{p}}$. Thus $D(\mathcal{P}_i|\mathfrak{p})$ has σ such that $\forall \alpha \in \mathcal{O}_L$, $\sigma\alpha \equiv \alpha^{|\mathfrak{p}|} \pmod{\mathcal{P}_i}$. This is what we called Frobenius element. We denote Frobenius element of $D(\mathcal{P}_i|\mathfrak{p})$ as $\left[\frac{L/K}{\mathcal{P}_i}\right]$

We observe some properties of the Frobenius element σ .

1. σ is unique in $D(\mathcal{P}_i|\mathfrak{p})$
2. The order of σ is $f(\mathcal{P}_i|\mathfrak{p})$
3. Let $\tau \in G$, then $\left[\frac{L/K}{\tau\mathcal{P}_i}\right] = \tau\left[\frac{L/K}{\mathcal{P}_i}\right]\tau^{-1}$. Specifically, when G is abelian, $\left[\frac{L/K}{\mathfrak{p}}\right]$ is the same for all \mathcal{P}_i above \mathfrak{p} . In this case we use $\psi(\mathfrak{p})$ to denote its Frobenius element because it's determined entirely by \mathfrak{p} .

This special case gives rise to the following definition:

Definition 2.12. Suppose G is abelian Let I^S be all the ideals in \mathcal{O}_K that are coprime to the ramifying primes. Then for the $\mathfrak{p} \in I^S$, \mathfrak{p} is unramified. Then Artin map is the homomorphism $\psi: I^S \rightarrow G$ such that for a prime \mathfrak{p} , $\psi(\mathfrak{p})$ is the corresponding Frobenius element. For $I \in I^S$, $\psi(I)$ is the product of Frobenius element of its prime factor.

(Notice that if G is non-abelian Artin map is not well defined)

5. Recall that for L/K Galois extension, we say $\mathfrak{p} \subseteq \mathcal{O}_K$ splits completely in \mathcal{O}_L iff $e(\mathcal{P}_i|\mathfrak{p}) = f(\mathcal{P}_i|\mathfrak{p}) = 1$. Now consider cyclotomic extension $\mathbb{Q}(\zeta_m)/\mathbb{Q}$. This is an abelian extension and a prime $p \in \mathbb{Q}$ ramifies iff $p|m$. Then for $p \in \mathbb{Q}$, we have $\psi(p)\alpha \equiv \alpha^p \pmod{\mathcal{P}_i} \forall \mathcal{P}_i$. Then by Chinese reminder theorem:

$$\psi(p)\alpha \equiv \alpha^p \pmod{p}$$

For all $p \nmid m$ But $\text{Gal}(\mathbb{Q}(\zeta_m)/\mathbb{Q})$ is isomorphic to $(\mathbb{Z}/m\mathbb{Z})^*$ with the map being

$$k \rightarrow (g_k : \zeta_m \rightarrow \zeta_m^k)$$

Thus there exists $\sigma \in G$ such that $\sigma\zeta_m = \zeta_m^p$, and there are,

$$\sigma\alpha \equiv \alpha^p \pmod{p}$$

Thus this σ is the Frobenius element $\psi(p)$.

On the other hand, recall that $f(\mathcal{P}_i|\mathfrak{p})$ is the order of $\psi(p)$, so the σ in this case is the identity. So σ should fix ζ_m . This happens iff

$$p \equiv 1 \pmod{m}$$

which is thus the sufficient and necessary condition for \mathfrak{p} to split completely in $\mathbb{Q}(\zeta_m)/\mathbb{Q}$.

3 Riemann zeta function and prime number theorem

3.1 Riemann zeta function

In this section we briefly mention some properties of Riemann zeta function. These proofs can be found in the chapter 7 of [10]

Lemma 3.1. Consider $f(s) = \sum_{n=1}^{\infty} \frac{a_n}{n^s}$. Series in this form are called the Dirichlet series. If $\sum_{n \leq t} a_n = O(t^r)$, then $f(s)$ is analytic and convergent for $\text{Re}(s) > r$

Definition 3.2. The Riemann zeta function is defined as

$$\zeta(s) = \sum_{n=1}^{\infty} \frac{1}{n^s}$$

By the lemma, $\zeta(s)$ converges and is analytic in $\text{Re}(s) > 1$. But this definition does not work $\text{Re}(s) \leq 1$. It turns out that we can find a meromorphic extension of $\zeta(s)$ to $\text{Re}(s) > 0$. i.e., we can find $g(s)$ a meromorphic function that is defined on $\text{Re}(s) > 0$ except for some poles, such that $g(s)$ agrees with $\zeta(s)$ on $\text{Re}(s) \geq 1$. By complex analysis, this means that $g(s)$ and $\zeta(s)$ agree whenever both of them are defined.

Our $g(s)$ is defined as follows. Consider

$$f(s) = 1 - \frac{1}{2^s} + \frac{1}{3^s} - \frac{1}{4^s} + \dots$$

Then the partial sums of the coefficients alter between 0 and 1, so are $O(t^0)$. Then by the lemma $g(s)$ is convergent on $\text{Re}(s) > 0$. Then let

$$g(s) = \frac{f(s)}{1 - \frac{1}{2^s}}$$

We know that $g(s) = \zeta(s)$ when $\text{Re}(s) > 1$. $\frac{f(s)}{1 - \frac{1}{2^s}}$ is analytic on $\text{Re}(s) > 0$ except for when $\frac{1}{2^s} = 1$, where it might have a pole. But it is not necessary since the pole can be cancelled if $f(s)$ is zero.

In order to find where the poles actually are, we construct another expression for $\zeta(s)$.

Let

$$t(s) = 1 + \frac{1}{2^s} - \frac{2}{3^s} + \frac{1}{4^s} + \frac{1}{5^s} - \frac{2}{6^s} + \dots$$

Then the partial sum of the coefficients alter between 0,1,2, so are $O(t^0)$. So $t(s)$ is also analytic on $\text{Re}(s) > 0$. We can get that $\frac{t(s)}{1 - \frac{1}{2^s}} = \zeta(s)$. Thus $\frac{g(s)}{1 - \frac{1}{2^s}}$ and $\frac{t(s)}{1 - \frac{1}{2^s}}$ are both meromorphic extension of $\zeta(s)$. Since they agree on $\text{Re}(s) > 1$, they agree whenever both of them are defined. Thus the pole of $\frac{g(s)}{1 - \frac{1}{2^s}}$ and $\frac{f(s)}{1 - \frac{1}{2^s}}$ should also agree.

Now say s is the pole, then we must have $1 - \frac{1}{2^s} = 0$ and $1 - \frac{1}{3^s} = 0$. Thus $(1-s)\log 2 = (1-s)\log 3$. This doesn't happen unless $s = 1$. So the only possible pole of the extension of $\zeta(s)$ is at $s = 1$.

Since $f(1) = \log 2$ is not 0, we have

$$\lim_{s \rightarrow 1} (s-1) \frac{f(s)}{1 - \frac{1}{2^s}} = \lim_{s \rightarrow 1} (s-1) \frac{f(1)}{1 - \frac{1}{2^s}} = \lim_{s \rightarrow 1} \frac{f(1)}{\frac{2^{1-s}-1}{s-1}}$$

which is 1. Thus $\zeta(s)$ has a simple pole at $s = 1$ with residue 1, and is analytic elsewhere on $\text{Re}(s) > 0$.

3.2 Proof of the Prime Number Theorem

Theorem 3.3 (the Prime Number Theorem). Let $\pi(x)$ denote the number of primes not exceeding x . Then we have

$$\pi(x) \sim \frac{x}{\log x}$$

$\pi(x) \sim \frac{x}{\log x}$ here just means that as x approaches infinty, $\frac{\pi(x)}{\frac{x}{\log x}}$ approaches

1. It is quite stunning that the proof of the Prime Number Theorem is based totally on the behavior of $\zeta(s)$ on $\text{Re}(s) \geq 1$.

Consider the product representation of zeta function when $\text{Re}(s) > 1$

$$\zeta(s) = \prod_{p \in \mathbb{Z}} \left(1 - \frac{1}{p^s}\right)^{-1}$$

which is equivalent to the fundamental theorem of arithmetic. Taking the logarithm, we have

$$\log \zeta(s) = - \sum_p \log \left(1 - \frac{1}{p^s}\right) = \sum_p \sum_{m=1}^{\infty} \frac{1}{mp^{ms}}$$

Differentiating gives

$$-\frac{\zeta'(s)}{\zeta(s)} = \sum_p \sum_{m=1}^{\infty} \frac{\log p}{p^{ms}} = \sum_p \frac{\log p}{p^s} + \sum_p \sum_{m=2}^{\infty} \frac{\log p}{p^{ms}}$$

Since $\log p < p^\sigma$ as $p \rightarrow \infty \forall \sigma > 0$, the sum of absolute value of each term is

$$\sum_p \frac{\log p}{|p^s|} = \sum_p \frac{\log p}{p^{\text{Re}(s)}} = \sum_p \frac{\log p}{p^{\frac{\text{Re}(s)+1}{2}}} \cdot \frac{1}{p^{\frac{\text{Re}(s)+1}{2}}}$$

For $\text{Re}(s) > 1$, $\frac{\text{Re}(s)+1}{2} > 1$, so $\sum_p \frac{\log p}{p^s}$ converges absolutely for $\text{Re}(s) > 1$, and so is analytic there. Similarly we can get $\sum_p \sum_{m=2}^{\infty} \frac{\log p}{p^{ms}}$ converges absolutely for $\text{Re}(s) > \frac{1}{2}$, and thus is analytic on $\text{Re}(s) = 1$. The term $\sum_p \sum_{m=2}^{\infty} \frac{\log p}{p^{ms}}$

converges absolutely for $\text{Re}(s) > \frac{1}{2}$. Thus the asymptotic growth of $-\frac{\zeta'(s)}{\zeta(s)}$ at $\text{Re}(s) = 1$ is the same as $\sum_p \frac{\log p}{p^s}$.

For $\log \zeta(s)$ and its derivative to be defined on $\text{Re}(s) \geq 1$ we need $\zeta(s)$ to be non-zero on $\text{Re}(s) \geq 1$. The non-zero property for $\text{Re}(s) > 1$ is shown by the product representation, so it remains to show that $\zeta(s) \neq 0$ on $\text{Re}(s) = 1$.

Theorem 3.4. $\zeta(s) \neq 0$ on $\text{Re}(s) = 1$

Proof. For $\text{Re}(s) > 1$ we can use the product representation. We have

$$\log \zeta(s) = \sum_p \sum_{m=1}^{\infty} \frac{1}{mp^{ms}} = \sum_p \sum_{m=1}^{\infty} e^{-ms \log p}$$

Now say $s = \sigma + it$, $\sigma, t \in \mathbb{R}$, we have

$$|\zeta(s)| = \left| \exp \left(\sum_p \sum_{m=1}^{\infty} \frac{1}{m} e^{-\sigma m \log p} (\cos(tm \log p) - i \sin(tm \log p)) \right) \right| = \exp \left(\sum_p \sum_{m=1}^{\infty} \frac{1}{mp^{m\sigma}} \cos(tm \log p) \right)$$

Now let $1 + it$ be the hypothetical zero, so $t \neq 0$ because $\zeta(s)$ has a pole at 1. Then we have

$$|\zeta(\sigma)|^3 |\zeta(\sigma + it)|^4 |\zeta(\sigma + 2it)| = \exp \left(\sum_p \sum_{m=1}^{\infty} \frac{1}{mp^{m\sigma}} (3 + 4 \cos(tm \log p) + \cos(2tm \log p)) \right)$$

But $3 + 4 \cos \theta + \cos 2\theta = 2(\cos \theta + 1)^2 \geq 0$ for all θ . So

$$\exp \left(\sum_p \sum_{m=1}^{\infty} \frac{1}{mp^{m\sigma}} (3 + 4 \cos tm \log p + \cos 2tm \log p) \right) \geq 1$$

Thus

$$|\zeta(\sigma)(\sigma - 1)|^3 \left| \frac{\zeta(\sigma + it)}{\sigma - 1} \right|^4 |\sigma(2 + it)| \geq \frac{1}{\sigma - 1} \quad (1)$$

Now let σ approach 1 from above. Then $|\zeta(\sigma)(\sigma - 1)|^3$ is a non-zero finite value; $|\zeta(\sigma + 2it)|$ is finite because $\zeta(s)$ is analytic on $\text{Re}(s) \geq 1$ except for $s = 1$; $\left| \frac{\zeta(\sigma + it)}{\sigma - 1} \right|^4$ is also finite because $\frac{1}{\sigma - 1}$ is cancelled by $\zeta(1 + it) = 0$. Thus the left of (1) is finite, while the right of (1) approaches infinity as $\sigma \rightarrow 1$. We reach a contradiction.

So $\zeta(s) \neq 0$ on $\text{Re}(s) \geq 1$ □

Since $\zeta(s)$ only has a simple pole at $s = 1$, $\zeta(s)(s - 1)$ is analytic everywhere on $\text{Re}(s) \geq 1$ and so is its derivative. We know that

$$(\zeta(s)(s - 1))' = \zeta'(s)(s - 1) + \zeta(s)$$

is finite on $s = 1$. Since $\zeta(s)$ is non-zero on $\text{Re}(s) \geq 1$, we can divide both sides by $\zeta(s)$ and take $s \rightarrow 1$, obviously

$$0 = \lim_{s \rightarrow 1^+} \frac{\zeta'(s)}{\zeta(s)} (s - 1) + 1$$

From here we know that $-\frac{\zeta'(s)}{\zeta(s)}$ has a pole at $s = 1$ with residue 1, and is analytic on the rest of $\text{Re}(s) \geq 1$.

Recall that $\sum_p \frac{\log p}{p^s}$ has the same residue and pole as $-\frac{\zeta'(s)}{\zeta(s)}$ when $s \rightarrow 1$. So $\sum_p \frac{\log p}{p^s}$ is analytic on $\text{Re}(s) \geq 1$ except for a simple pole at $s = 1$ with residue 1.

Now let us write $\sum_p \frac{\log p}{p^s}$ as Dirichlet series: let $a(n)$ be the prime indicator function, namely

$$a(n) = \begin{cases} 1, & \text{if } n \text{ is a prime} \\ 0, & \text{otherwise} \end{cases}$$

Then

$$\sum_p \frac{\log p}{p^s} = \sum_{n=1}^{\infty} \frac{a(n) \log n}{n^s}$$

Notice that $\pi(x) = \sum_{n \leq x} a(n)$, and we want to show that

$$\sum_{n \leq x} a(n) \sim \frac{x}{\log x}$$

We are then able to apply the following theorem:

Theorem 3.5. Let $f(t)$ be non-negative and non-decreasing piecewise continuous real function on $[1, \infty]$ and $f(t) = O(t)$. Then the Mellin transform $g(s) = s \int_1^{\infty} f(x) x^{-s-1} dx$ is analytic for $\text{Re}(s) > 1$. Additionally, If $g(s) - \frac{c}{s-1}$ has analytic extension to neighbourhood of $\text{Re}(s) = 1$, then as $x \rightarrow \infty$, $f(x) \sim cx$

This theorem is a corollary of Auxiliary Tauberian theorem. The proofs of both can be found at page 10 of [13]. Plugging in the $f(x) = \sum_{n \leq x} a(n) \log n$ into the theorem, we get that $g(s) = \frac{-\zeta'(s)}{\zeta(s)}$. Since $\frac{-\zeta'(s)}{\zeta(s)}$ has only a simple pole at $s = 1$ with residue 1, $\frac{-\zeta'(s)}{\zeta(s)} - \frac{1}{s-1}$ has analytic continuation to $\text{Re}(s) \geq 1$. Also it is true that $\sum_{n \leq x} a(n) \log n = O(x)$, as proved in chapter 4.5 of [17]. Now we have all the conditions required to apply Theorem 3.5. We get

$$\sum_{n \leq$$

We know that $\sum_{n \leq x} b(n) \sim x$. Using this we can show that

$$\int_3^x \frac{\sum_{n \leq t} b(t)}{t(\log t)^2} dt = o\left(\frac{x}{\log x}\right)$$

The detailed proof can be found in chapter 4.3 of [17]. Then we have

$$\sum_{3 < n \leq x} \frac{b(n)}{\log n} = \frac{x}{\log x} + o\left(\frac{x}{\log x}\right)$$

Which is the statement of the Prime Number Theorem.

We give another equivalent statement of the Prime Number Theorem: Define $Li(x) = \int_2^x \frac{1}{\log t} dt$, then we have:

$$\pi(x) \sim Li(x)$$

$Li(x)$ is a better approximation of $\pi(x)$ than $\frac{x}{\log x}$, but if we just look at the asymptotic formula the two statements are equivalent. From integrating by parts we know that

$$Li(x) = \frac{x}{\log x} - \int_2^x \frac{1}{(\log t)^2}$$

Notice that $\int_2^x \frac{1}{(\log t)^2}$ is small compared to $\frac{x}{\log x}$, so $\frac{Li(x)}{\frac{x}{\log x}}$ goes to 1 as $x \rightarrow \infty$. Therefore the two statements of the Prime Number Theorem are equivalent.

4 L-series and Prime Ideal Theorem

4.1 Dedekind zeta function

Now that we have introduced $\zeta(s)$ and its extension to $\text{Re}(s) > 0$, we can consider a generalized version of $\zeta(s)$, the Dedekind zeta function.

Definition 4.1. Let K be a finite extension of \mathbb{Q} . Let j_n denote the number of ideals I of \mathcal{O}_K with $\|I\| = n$. Then the Dedekind zeta function is defined as $\zeta_K(s) = \sum_{n=1}^{\infty} \frac{j_n}{n^s}$.

Equivalently it can also be written as $\zeta_K(s) = \sum_{I \in \mathcal{O}_K} \frac{1}{\|I\|^s}$.

Definition 4.2. Let \mathcal{O}_K be ring of integer of K . Then we define the class group C to be the group of all the fractional ideals in \mathcal{O}_K quotient out by principal ideals.

Then we cite a theorem about the distribution of ideals in a number ring. Readers can refer to chapter 6 of [10]

Theorem 4.3. Let C be a class group in \mathcal{O}_K , and let $i_c(t)$ denote the number of ideals in C with norm $\leq t$. Then we have

$$i_c(t) = \kappa t + \mathcal{O}(t^{1-\frac{1}{[K:\mathbb{Q}]}}), \text{ Where } \kappa \text{ is a constant independent of } C$$

Now let h be the number of ideal classes in K . Then we have

$$\sum_{n \leq t} j_n = h\kappa t + \mathcal{O}(t^{1-\frac{1}{[K:\mathbb{Q}]}})$$

Thus we know that $\sum_{n \leq t} j_n = \mathcal{O}(t)$, which by lemma 3.1 implies $\zeta_K(t)$ is convergent and analytic on $\text{Re}(s) > 1$

Now on $\text{Re}(s) > 1$, by changing the order of summation we have

$$\zeta_K(s) = \sum_{n=1}^{\infty} \frac{j_n - h\kappa}{n^s} + h\kappa \zeta(s)$$

But $\sum_{n \leq t} j_n - h\kappa = \mathcal{O}(t^{1-\frac{1}{[K:\mathbb{Q}]}})$. By the lemma 3.1 $\sum_{n=1}^{\infty} \frac{j_n - h\kappa}{n^s}$ is convergent and analytic for $\text{Re}(s) \leq 1 - \frac{1}{[K:\mathbb{Q}]}$. We also know that $\zeta(s)$ has extension on $\text{Re}(s) > 0$ except for a simple pole at $s=1$. So when K different from \mathbb{Q} , $\zeta_K(s)$ has meromorphic extension to $\text{Re}(s) > 1 - \frac{1}{[K:\mathbb{Q}]}$, analytic except for simple pole at $s = 1$ with residue $h\kappa$.

Similar to $\zeta(s)$ we have product representation for $\zeta_K(s)$ on $\text{Re}(s) > 1$. With the unique factorization of ideals in Dedekind domain, $\|I\| = \prod_{\mathfrak{p} \mid I} \|\mathfrak{p}\|^{e_i}$, where \mathfrak{p}_i denotes prime ideals of \mathcal{O}_K . Since norm is multiplicative, when $\text{Re}(s) > 1$, we have

$$\zeta_K(s) = \prod_{\mathfrak{p} \in \mathcal{O}_K} \left(1 - \frac{1}{\|\mathfrak{p}\|^s}\right)^{-1}$$

4.2 L-series

$\text{Gal}(L/K)$ is abelian. We continue to write $G = \text{Gal}(L/K)$, and we let χ to be a character at G .

Let S be set of all ramified prime, so S is finite. Let I^S be group of fractional ideals in \mathcal{O}_K that are coprime to primes in S . Recall we defined the Artin map:

$$\phi: I^S \rightarrow G$$

as sending the primes in I^S to the corresponding Frobenius element in G . We denote the image of \mathfrak{p} by $\phi(\mathfrak{p})$. By the multiplicity of ϕ , for ideals $I = \prod_{i=1}^k \mathfrak{p}_i^{e_i}$, $\phi(I) = \prod_{i=1}^k \phi(\mathfrak{p}_i)^{e_i}$. Then $\chi \circ \phi$ is a character on I^S . For $I \notin I^S$, we let $\chi \circ \phi(I) = 0$, thereby extending $\chi \circ \phi$ to all ideals.

Definition 4.4. $L(s, \chi) = \sum_{n=1}^{\infty} \frac{\sum_{\|I\| \leq n} \chi \circ \phi(I)}{n^s} = \sum_{I \subseteq \mathcal{O}_K} \frac{\chi \circ \phi(I)}{\|I\|^s}$

Since $\chi \circ \phi(I)$ is 0 or root of unity, $\sum_{\|I\| \leq n} \chi \circ \phi(I) \leq \sum_{k=1}^n j_k$. Thus $L(s, \chi)$ converges absolutely for $\text{Re}(s) > 1$.

By the multiplicity of $\chi \circ \phi$ has the product representation

$$L(s, \chi) = \prod_{\mathfrak{p} \in \mathcal{O}_K} \left(1 - \frac{\chi \circ \phi(\mathfrak{p})}{\|\mathfrak{p}\|^s}\right)^{-1}$$

Notice that if we take χ as the trivial character χ_0 ,

$$L(s, \chi) = \prod_{\mathfrak{p} \in \mathcal{O}_K, \text{ unramified}} \left(1 - \frac{1}{\|\mathfrak{p}\|^s}\right)^{-1}$$

So $L(s, \chi)g(s) = \zeta_K(s)$, if $g(s) = \prod_{\mathfrak{p} \text{ ramified}} \left(1 - \frac{1}{\|\mathfrak{p}\|^s}\right)^{-1}$. This is a finite product so it's analytic on $\text{Re}(s) > 0$. So for $1 - \frac{1}{[K:\mathbb{Q}]} < \text{Re}(s) \leq 1$, we can take $\frac{\zeta_K(s)}{g(s)}$ as the memorphic extension of $L(s, \chi_0)$. This extension should have the same asymptotic behavior as $\zeta_K(s)$. It's analytic in the range except for a simple pole at $s = 1$.

In general for $\chi \in \hat{G}$ we have the following:

Theorem 4.5. $\sum_{\|I\| \leq t} \chi \circ \phi(I) = at + \mathcal{O}(t^{1-\frac{1}{[K:\mathbb{Q}]}})$, where a is some non-zero constant if χ is trivial, and zero if χ is non-trivial

The case when the character is trivial has been proven above. Assuming the theorem is true for non-trivial characters, by Lemma 3.1 we know $L(s, \chi)$ has analytic extension to $\text{Re}(s) > 1 - \frac{1}{[K:\mathbb{Q}]}$, except for a simple pole at $s = 1$ when χ is trivial.

Now to prove the theorem, notice that $\chi \circ \phi$ as a character on I^S takes value 1 on kernel of ϕ . So $\chi \circ \phi$ can be regarded as a character on $I^S / \ker \phi$. Then we need to use the Artin reciprocity. Proofs is found in chapter 5.3 of [15]

Theorem 4.6 (Artin reciprocity). Let L be a finite abelian extension of K , S is the primes ramify in L . Then there exists m such that the primes dividing m are precisely the ramified primes. Then we have

$$I^S / K_{m,1} N m_K^L(I) \cong G$$

Here $K_{m,1}$ is the set of principal ideals (a) such that $a \equiv 1 \pmod{m}$ and a is totally positive. $N m_K^L(I)$ is the image of ideals in L under the norm map.

Now let ψ be a homomorphism $I^S \rightarrow G$ with $K_{m,1}$ included in the kernel. Since $K_{m,1}$ has a finite index in I^S (chapter 5.3 of [15]), $I^S / K_{m,1}$ is a finite abelian group, so ψ can be regarded as 1-dimensional character on $I^S / K_{m,1}$. Denote a coset of $K_{m,1}$ in I^S as C . Now consider $\sum_{\|I\| \leq x} \psi(I) = \sum_C \sum_{\|I\| \leq x, I \in C} \psi(I)$. Since ψ takes the same value on elements that belong to the same coset of $K_{m,1}$, we can denote the value of ψ on the coset C as $\psi(C)$. The sum is thus $\sum_C \psi(C) \sum_{\|I\| \leq x, I \in C} 1$

Now consider the inner sum

$$\sum_{\|I\| \leq x, I \in C} 1$$

Let J be a fixed ideal in C^{-1} . Then for any $I \in C$, there exists a such that $a \equiv 1 \pmod{m}$ and a totally positive such that $(a) = IJ$. Since a is totally positive we have:

$$\|a\| = \|(a)\| = \|IJ\| \|J\|$$

Thus the inner sum is also

$$\sum_{\|a\| \leq x \|J\|, (a) \subseteq J} 1$$

The question is now reduced to counting the number of ideal $(a) \subseteq J$ with some bound on the norm. In page 210 of [16] the author proves that $bx + \mathcal{O}(x^{1-\frac{1}{[K:\mathbb{Q}]}})$, where b is independent of C .

$$\sum_C \psi(C) bx + \mathcal{O}(x^{1-\frac{1}{[K:\mathbb{Q}]}})$$

By the orthogonality relations of characters, $\sum_C \psi(C) = 0$ for non-trivial ψ , and is $cx + \mathcal{O}(x^{1-\frac{1}{[K:\mathbb{Q}]}})$ for ψ being trivial, where c is some constant depending on \mathcal{O}_K . Since $\chi \circ \phi$ also takes value 1 on $K_{m,1}$, it has this property. Thus we have

$$\sum_{\|I\| \leq x} \chi \circ \phi(I) = \begin{cases} o(x^{1-\frac{1}{[K:\mathbb{Q}]}}), & \text{if } \chi \circ \phi \text{ is non-trivial} \\ cx + o(x^{1-\frac{1}{[K:\mathbb{Q}]}}), & \text{if } \chi \circ \phi \text{ is trivial} \end{cases}$$

Now we can apply the lemma on $L(s, \chi)$. From the above formula we know that $L(s, \chi)$ is analytic on $\text{Re}(s) \geq 1$ if $\chi \circ \phi$ is trivial, and that $L(s, \chi)$ is analytic on $\text{Re}(s) \geq 1$ except for a simple pole at $s = 1$ if $\chi \circ \phi$ is trivial character.

4.3 Prime Ideal Theorem

We want to prove here the following generalization of the Prime Number Theorem:

Theorem 4.7.

$$\sum_{\|\mathfrak{p}\| \leq x} \chi \circ \phi(\mathfrak{p}) = \begin{cases} \frac{x}{\log x} + o\left(\frac{x}{\log x}\right) & \text{if } \chi \circ \phi \text{ is the trivial character} \\ o\left(\frac{x}{\log x}\right) & \text{if otherwise} \end{cases} \quad (2)$$

Similar to the proof of prime number theory, we need to some properties of $\log L(s, \chi)$ in $\text{Re}(s) \geq 1$. $\log L(s, \chi)$ is analytic and doesn't have zero on $\text{Re}(s) > 1$, and we know that $L(s, \chi)$ is analytic on $\text{Re}(s) = 1$ except for maybe a simple pole at $s = 1$. Now we only need that $L(s, \chi)$ is non-zero on $\text{Re}(s) = 1$ to make $\log L(s, \chi)$ well defined.

Lemma 4.8. $L(s, \chi) \neq 0$ for any χ

Proof. The proof is divided into two cases.

Case 1. Suppose $(\chi \circ \phi)^2$ is not a trivial character. Then say that $L(1 + it, \chi) = 0$ for $t \neq 0$, and say $s = \sigma + it$. For $\text{Re}(s) > 1$, we can use the product representation of $L(s, \chi)$ and take its logarithm, which is

$$\log L(s, \chi) = \sum_{\mathfrak{p} \in \mathcal{O}_K} \sum_{m=1}^{\infty} \frac{\chi \circ \phi(\mathfrak{p}^m)}{m \|\mathfrak{p}\|^{ms}}$$

Let $\chi \circ \phi(\mathfrak{p}) = e^{ai}$ for \mathfrak{p} unramified. Thus

$$L(s, \chi) = \exp \left(\sum_{\mathfrak{p} \in \mathcal{O}_K, \mathfrak{p} \text{ unramified}} \sum_{m=1}^{\infty} e^{m(a-t \log \|\mathfrak{p}\|)} \frac{1}{m \mathfrak{p}^{ms}} \right)$$

Take the absolute value, we have

$$|L(s, \chi)| = \exp \left(\sum_{\mathfrak{p} \text{ unramified}} \sum_{m=1}^{\infty} \cos(m(a-t \log \|\mathfrak{p}\|)) \frac{1}{m \mathfrak{p}^{ms}} \right)$$

Then

$$|L(s, \chi_0)|^3 |L(\sigma + it, \chi)|^4 |L(\sigma + 2it, \chi^2)|$$

$$= \exp \sum_{\mathfrak{p} \text{ unramified}} \sum_{m=1}^{\infty} \frac{1}{m \mathfrak{p}^{ms}} (3 + 4 \cos m(a-t \log \|\mathfrak{p}\|) + \cos 2m(a-t \log \|\mathfrak{p}\|))$$

Also, $L(\sigma + 2it, \chi^2)$ isn't a pole, since $L(s, \chi)$ only has a pole when $s = 1$ and $\chi = \chi_0$. The rest is exactly the same as in the Prime number theorem. We can derive a contradiction. \square

Case 2. Now suppose $\chi \circ \phi^2$ is trivial character. If the hypothetical zero of $L(s, \chi)$ is not $s = 1$, say it's $s = 1 + it$. then $|L(1 + 2it, \chi_0)|$ is finite because $L(s, \chi)$ has a pole only when $s = 1$ and $\chi = \chi_0$. Then the above proof still works out.

Now we only need to consider the case when the hypothetical zero of $L(s, \chi)$ is $s = 1$. This is impossible for $\chi \circ \phi$ being trivial character, so we only need to consider the case when $\chi \circ \phi$ is non-trivial.

By extending the Dirichlet series product, we find

$$\zeta_K(s) L(s, \chi) = \sum_I \frac{\sum_{d \mid I} \chi \circ \phi(d)}{\|I\|^s} \quad (3)$$

when the series is convergent. Now let $a_n = \sum_{\|I\|=n} \sum_{d \mid I} \chi \circ \phi(d)$, and write (3) as a Dirichlet series $\sum_{n=1}^{\infty} \frac{a_n}{n^s}$.

Since

$$\sum_{d \mid I} \chi \circ \phi(d) = \prod_{\mathfrak{p} \mid I} (1 + \chi \circ \phi(\mathfrak{p}) + \chi \circ \phi(\mathfrak{p}^2) + \dots + \chi \circ \phi(\mathfrak{p}^{e_{\mathfrak{p}}}))$$

This sum is positive if $\chi \circ \phi(\mathfrak{p}) = 1$, and when $\chi \circ \phi(\mathfrak{p}) = -1$ then the sum is 1 for $e_{\mathfrak{p}}$ being odd and is 0 when $e_{\mathfrak{p}}$ being even. Thus $a(n) \geq 0$. For I being a square, we have $\sum_{d \mid I} \chi \circ \phi(d) \geq 1$. Thus we have the below inequality:

$$\sum_I \frac{\sum_{d \mid I} \chi \circ \phi(d)}{\|I\|^s} \geq \sum_J \frac{1}{\|J\|^{2s}} \quad (4)$$

Here we assume the fact that $\zeta_K(s)$ and $L(s, \chi)$ has meromorphic extension to the entire complex plane, analytic everywhere except for a simple pole at $s = 1$ for $\zeta_K(s)$ (page 7 of [18]). Then $\zeta_K(s) L(s, \chi)$ should be analytic everywhere as the pole of $\zeta_K(s)$ at $s = 1$ is cancelled by the hypothetical zero of $L(s, \chi)$ at $s = 1$. Here we cite a theorem of Dirichlet series from page 213 of [16]:

Theorem 4.9. The Dirichlet series $f(s) = \sum_{n=1}^{\infty} \frac{a_n}{n^s}$ with $a_n \geq 0$ has a half plane $\text{Re}(s) > a$ as its domain of convergence. If a is finite, then $f(s)$ is non-regular (has a pole) at $s = a$

To apply the theorem take $f(s) = \zeta_K(s) L(s, \chi)$ and so $f(s)$ is the series $\sum_I \frac{\sum_{d \mid I} \chi \circ \phi(d)}{\|I\|^s}$ when both are convergent. Knowing that $f(s)$ converges everywhere, we want to show that $\sum_I \frac{\sum_{d \mid I} \chi \circ \phi(d)}{\|I\|^s}$ also converges everywhere. If it doesn't, then there exists σ_0 such that $\sum_I \frac{\sum_{d \mid I} \chi \circ \phi(d)}{\|I\|^s}$ converges to the right of σ_0 and to the left. Then theorem 4.9 says that $f(s)$ can't be extended to the neighbourhood of σ_0 , which is not true because we just showed that $f(s)$ is

analytic on the entire complex plane. So $\sum_I \frac{\sum_{d \mid I} \chi \circ \phi(d)}{\|I\|^s}$ should be convergent everywhere.

Now take $\sigma \rightarrow \frac{1}{2}$ in equation 4. The left is convergent, while the right diverges. So we derive a contradiction, which means $L(s, \chi)$ can't have an zero at $s = 1$.

Combining with case 1 we show that $L(s, \chi)$ is non-zero on $\text{Re}(s) = 1$. Then if $\chi \circ \phi$ is non-trivial, $L(s, \chi)$ is non-zero and analytic on $\text{Re}(s) \geq 1$, thus $L(s, \chi)$ is also analytic in this region, and so is $-\frac{L'(s, \chi)}{L(s, \chi)}$. If $\chi \circ \phi$ is the trivial character, similar to in the proof of the Prime Number Theorem, we can prove that $-\frac{L'(s, \chi)}{L(s, \chi)}$ has a simple pole at $s = 1$ with residue 1

Now for $\text{Re}(s) > 1$, use the product representation of $L(s, \chi)$ and differentiate its logarithm, we obtain

$$-\frac{L'(s, \chi)}{L(s, \chi)} = \sum_{\mathfrak{p} \in \mathcal{O}_K} \frac{\log \|\mathfrak{p}\| \chi \circ \phi(\mathfrak{p})}{\|\mathfrak{p}\|^s} + \sum_{\mathfrak{p} \in \mathcal{O}_K} \sum_{m=2}^{\infty} \frac{\log \|\mathfrak{p}\| \chi \circ \phi(\mathfrak{p})}{\|\mathfrak{p}\|^s}$$

Since there are only at most $[K:\mathbb{Q}]$ of \mathfrak{p} above a rational prime p , and that $\|\mathfrak{p}\| \geq p$, we know that

$$\sum_{m=2}^{\infty} \frac{\log \|\mathfrak{p}\| \chi \circ \phi(\mathfrak{p})}{\|\mathfrak{p}\|^s} \leq \mathcal{O}(\sum_{\mathfrak{p}} \sum_{m=2}^{\infty} \frac{1}{p^{ms}})$$

Since $\sum_{m=2}^{\infty} \frac{1}{p^{ms}}$ is analytic on $\text{Re}(s) = 1$, $-\frac{L'(s, \chi)}{L(s, \chi)}$ has the same pole and same residue as $\sum_{\mathfrak{p} \in \mathcal{O}_K} \frac{\log \|\mathfrak{p}\| \chi \circ \phi(\mathfrak{p})}{\|\mathfrak{p}\|^s}$ when $s \rightarrow 1$. Now we write $\sum_{\mathfrak{p} \in \mathcal{O}_K} \frac{\log \|\mathfrak{p}\| \chi \circ \phi(\mathfrak{p})}{\|\mathfrak{p}\|^s}$ as a Dirichlet series, namely

$$\sum_{n=1}^{\infty} \frac{\sum_{\|\mathfrak{p}\|=n} \log \|\mathfrak{p}\| \chi \circ \phi(\mathfrak{p})}{n^s}$$

This allows us to apply the following Wiener-Ikehara theorem.

Theorem 4.10 (Wiener-Ikehara). Consider two Dirichlet series

$$f(s) = \sum_{m=1}^{\infty} \frac{a_m}{m^s}, \quad a_m \geq 0$$

And

$$g(s) = \sum_{m=1}^{\infty} \frac{b_m}{m^s}$$

such that both are absolutely convergent for $\text{Re}(s) > 1$. Also $f(s)$ is analytic on $\text{Re}(s) = 1$ except for a simple pole at $s = 1$ with residue 1, and $g(s)$ is analytic on $\text{Re}(s) = 1$, having either a simple pole at $s = 1$ with residue η or being analytic at $s = 1$ (in which case we can take $\eta = 0$). Then if $\exists \epsilon$ such that $|b_m| \leq \epsilon |a_m|$, we have

$$\lim_{x \rightarrow \infty} \frac{\sum_{m \leq x} b_m}{x} = \eta$$

i.e., $\sum_{m \leq x} b_m \sim \eta x$

Apply the Wiener-Ikehara theorem: let $f(s)$ be $\sum_{n=1}^{\infty} \frac{a(n) \log n}{n^s}$ where $a(n)$ is 1 if n is a prime and 0 otherwise. $f(s)$ is analytic on $\text{Re}(s) \geq 1$ except for a simple pole at $s = 1$ with residue 1. Let $g(s)$ be $\sum_{n=1}^{\infty} \frac{\sum_{\|\mathfrak{p}\|=n} \log \|\mathfrak{p}\| \chi \circ \phi(\mathfrak{p})}{n^s}$. We showed above that $g(s)$ is analytic on $\text{Re}(s) \geq 1$ except for possibly a simple pole at $s = 1$ with residue η ($\eta = 1$ if $\chi \circ \phi$ is trivial character and 0 otherwise). Also the coefficient of $\frac{1}{s^2}$ is at most $\sum_{\|\mathfrak{p}\|=n} \log \|\mathfrak{p}\| \leq [K:\mathbb{Q}]n$. Thus

$$\left| \sum_{\|\mathfrak{p}\|=n} \log \|\mathfrak{p}\| \chi \circ \phi(\mathfrak{p}) \right| \leq [K:\mathbb{Q}] a(n) \log n$$

Apply Wiener-Ikehara theorem, we get that

$$\sum_{\|\mathfrak{p}\| \leq x} \chi \circ \phi(\mathfrak{p}) \log \mathfrak{p} \sim \eta x$$

Now let $a(n) = \sum_{\|\mathfrak{p}\|=n} \chi \circ \phi(\mathfrak{p})$, $b(n) = \sum_{\|\mathfrak{p}\|=n} \chi \circ \phi(\mathfrak{p}) \log \mathfrak{p}$. Doing the same partial summation as we did in the Prime number theorem proof, we get that

$$\sum_{\|\mathfrak{p}\| \leq x} \chi \circ \phi(\mathfrak{p}) = \begin{cases} \frac{x}{\log x} + o\left(\frac{x}{\log x}\right) & \text{if } \chi \circ \phi \text{ is the trivial character} \\ o\left(\frac{x}{\log x}\right) & \text{if otherwise} \end{cases} \quad (5)$$

(5) is the generalized version of prime number theorem in number field extension. However, we can get more than the Prime Number Theorem from (5): we can derive Chebotarev's density theorem for L/K abelian.

$$\sum_{||\mathfrak{p}||\leq x}\sum_{\chi\in\bar{G}}\chi(a^{-1}\phi(\mathfrak{p}))\quad (6)$$

By orthogonality relations of characters, we know that $\sum_{\chi\in\bar{G}}\chi(a^{-1}\phi(\mathfrak{p}))$ is 0 if $\phi(\mathfrak{p})\neq a$ and is $|G|$ if $\phi(\mathfrak{p})=a$. Thus (6) is $|G|\cdot\#\{\mathfrak{p}:||\mathfrak{p}||\leq x,\phi(\mathfrak{p})=a\}$

However, (6) is also

$$\chi_0(a^{-1})\sum_{||\mathfrak{p}||\leq x}\chi_0\phi(\mathfrak{p})+\sum_{\chi\text{ non-trivial}}\chi(a^{-1})\sum_{||\mathfrak{p}||\leq x}\chi\phi(\mathfrak{p})\quad (7)$$

By (5), we know that (7) is $\frac{x}{\log x}+o(\frac{x}{\log x})$. Then equates two expressions of (6), we get that

$$\frac{\#\{\mathfrak{p}:||\mathfrak{p}||\leq x,\phi(\mathfrak{p})=a\}}{\#\{\mathfrak{p}:||\mathfrak{p}||\leq x\}}=\frac{\frac{1}{|G|}(\frac{x}{\log x})+o(\frac{x}{\log x})}{\frac{x}{\log x}+o(\frac{x}{\log x})}\rightarrow\frac{1}{|G|}$$

as $x\rightarrow\infty$

So we prove Chebotarev's density theorem for abelian extension.

4.5 Prime Ideal Theorem and Chebotarev for the non-abelian case

When L/K is not an abelian extension, $\text{Gal}(L/K)$ doesn't admit only 1-dimensional characters. So we need to generalize L-series associated to characters of G .

Definition 4.11 (Artin L-series). *For $G=\text{Gal}(L/K)$ not abelian, let ρ be an irreducible representation of G . Take \mathcal{P} an unramified prime in \mathcal{O}_L , and let \mathfrak{p} be the prime below it in \mathcal{O}_K . Recall that $[\frac{L/K}{\mathcal{P}}]\alpha\equiv\alpha^{||\mathfrak{p}||}\bmod\mathcal{P}$. Then $L(s,\rho,L/K)$ is defined as*

$$L(s,\rho,L/K)=\prod_{\mathfrak{p}\text{ unramified in } \mathcal{O}_L}\frac{1}{\det(\mathbb{1}-\rho[\frac{L/K}{\mathfrak{p}}]\cdot\frac{1}{||\mathfrak{p}||^s}}$$

Since determinant is an invariant under conjugation and different \mathcal{P} above the same \mathfrak{p} are conjugates of each other, the series is independent of the chose of \mathcal{P} .

Notice that $[\frac{L/K}{\mathcal{P}}]$ is diagonalizable since it has finite order in G . Also the eigenvalues satisfy the polynomial $x^f-1=0$, so they are roots of unity. Recall that the character of ρ is the trace of its matrix denoted as χ_ρ .

Now assume some nice properties of $L(s,\rho,L/K)$ that we will prove later on : $L(s,\rho,L/K)$ is analytic and non-zero on $\text{Re}(s)\geq 1$. Then we will know that $\frac{-L'(s,\rho,L/K)}{L(s,\rho,L/K)}$ is analytic on $\text{Re}(s)\geq 1$. But $\frac{-L'(s,\rho,L/K)}{L(s,\rho,L/K)}$ is also the derivative of $-\log L(s,\rho,L/K)$. So

$$\frac{-L'(s,\rho,L/K)}{L(s,\rho,L/K)}=\sum_{\mathfrak{p}\text{ unramified in } \mathcal{O}_L}\sum_{m=1}^{\infty}\frac{\log||\mathfrak{p}||\chi_\rho([\frac{L/K}{\mathfrak{p}}]^m)}{||\mathfrak{p}||^{ms}}$$

If the dimension of ρ is n , then

$$\left|\sum_{\mathfrak{p}\text{ unramified in } \mathcal{O}_L}\sum_{m=2}^{\infty}\frac{\log||\mathfrak{p}||\chi_\rho([\frac{L/K}{\mathfrak{p}}]^m)}{||\mathfrak{p}||^{ms}}\right|\leq n\sum_{\mathfrak{p}\text{ unramified in } \mathcal{O}_L}\sum_{m=2}^{\infty}\frac{\log||\mathfrak{p}||}{||\mathfrak{p}||^{ms}}$$

which we proved to be convergent for $\text{Re}(s)>\frac{1}{2}$. Thus $\frac{-L'(s,\rho,L/K)}{L(s,\rho,L/K)}$ has the same

pole and residue on $\text{Re}(s)=1$ as $\sum_{\mathfrak{p}\text{ unramified in } \mathcal{O}_L}\frac{\log||\mathfrak{p}||\chi_\rho([\frac{L/K}{\mathfrak{p}}])}{||\mathfrak{p}||^s}$. Then by exactly the same proof as in the abelian case we can show that

$$\sum_{||\mathfrak{p}||\leq x}\chi_\rho([\frac{L/K}{\mathfrak{p}}])=\begin{cases}\frac{x}{\log x}+o(\frac{x}{\log x}) & \text{if } \chi_\rho \text{ is the trivial character} \\ o(\frac{x}{\log x}) & \text{if otherwise}\end{cases}$$

This proves the Prime Ideal Theorem for the non-abelian case.

Corollary 4.11.1 (The Chebotarev Density theorem for non-abelian case). *Let C be an arbitrary conjugacy class in $G=\text{Gal}(L/K)$, then we have*

$$\frac{\#\{\mathfrak{p}:||\mathfrak{p}||\leq x, [\frac{L/K}{\mathfrak{p}}]\in C\}}{\#\{\mathfrak{p}:||\mathfrak{p}||\leq x\}}\rightarrow\frac{|C|}{|G|}\quad\text{as }x\rightarrow\infty$$

Proof. Let f be a class function on G that takes 1 on elements in C and 0 otherwise. Since the irreducible characters span the space of class function, we can write f as a linear combination of irreducible characters. Say $\chi_1,...,\chi_g$ are the irreducible characters of G , then say

$$f=\sum_{i=1}^ga_i\chi_i$$

Also $\sum_{\mu\in G}f(\mu)=|C|$. But we also have

$$\sum_{\mu\in G}f(\mu)=\sum_{i=1}^ga_i\sum_{\mu\in G}\chi_i(\mu)=a_0|G|$$

where a_0 is the coefficient of trivial character. Thus $a_0=\frac{|C|}{|G|}$

The number of $\mathfrak{p}\leq\mathcal{O}_K,||\mathcal{P}||\leq x$ that maps to C is $\sum_{||\mathfrak{p}||\leq x}f([\frac{L/K}{\mathfrak{p}}])$, then we have

$$\sum_{||\mathfrak{p}||\leq x}f([\frac{L/K}{\mathfrak{p}}])=\sum_{||\mathfrak{p}||\leq x}\sum_{i=1}^ga_i\chi_i([\frac{L/K}{\mathfrak{p}}])=\frac{|C|}{|G|}\frac{x}{\log x}+o(\frac{x}{\log x})$$

and we have

$$\frac{\#\{\mathfrak{p}:||\mathfrak{p}||\leq x, [\frac{L/K}{\mathfrak{p}}]\in C\}}{\#\{\mathfrak{p}:||\mathfrak{p}||\leq x\}}\rightarrow\frac{|C|}{|G|}\quad\text{as }x\rightarrow\infty$$

□

Now our task becomes to ensure that $L(s,\rho,L/K)$ has the nice properties we mentioned. We do this by reducing $L(s,\rho,L/K)$ into product of $L(s,\chi)$'s, in which χ are abelian characters.

For this purpose we need some properties.

1. $L(s,\rho_1+\rho_2,L/K)=L(s,\rho_1,L/K)L(s,\rho_2,L/K)$. This comes from the linearity of $\log L(s,\rho_1+\rho_2,L/K)$

2. Let ρ be representation of $\text{Gal}(L/F)$ with character χ_ρ , and ρ^* is the representation of $\text{Gal}(L/K)$ induced by ρ with character χ_{ρ^*} . Then

$$L(s,\rho^*,L/K)=L(s,\rho,L/F)/g(s,\rho)$$

for $g(s,\rho)$ being non-zero regular function. This is true also for F/K not Galois.

Proof. Take $g(s,\rho)$ to be $\prod_{p\in S}\frac{1}{\det(1-\rho^*[\frac{L/K}{\mathfrak{p}}]\cdot\frac{1}{||\mathfrak{p}||^s})}$, where S denotes the set of $\mathfrak{p}\in\mathcal{O}_K$ such that \mathfrak{p} is unramified in \mathcal{O}_F and ramified in \mathcal{O}_L , and $\mathcal{P}_F=\mathcal{P}\cap F$. Then it is sufficient to examine \mathfrak{p} unramified in L and the primes in F,L that is above \mathfrak{p} .

Say $\mathfrak{p}=q_1q_2....q_r$ in F . Let $f_i=f(q_i|\mathfrak{p})$, the inertia degree of q_i over \mathfrak{p} . We still denote the subgroup fixing F as H . Fix a prime $\mathcal{P}\in\mathcal{O}_L$ above \mathfrak{p} and let $\tau_i\in G$ such that $\tau_i\mathcal{P}\cap F=q_i$. Denote $[\frac{L/K}{\mathfrak{p}}]$ as μ . We have the decomposition of G into cosets of H given by

$$G=\bigcup_{i=1}^r\bigcup_{x=1}^{f_i}H\tau_i\mu^{x_i}$$

This can be checked by checking that $H\tau_i\mu^{x_i}\cap H\tau_j\mu^{x_j}=\emptyset$.

Now

$$\chi_{\rho^*}(\mu^n)=\sum_{i=1}^r\sum_{x_i=0}^{f_i-1}\chi_\rho(\tau_i\mu^{x_i}\tau_i^{-1})$$

where $\chi_\rho(\tau_i\mu^{x_i}\tau_i^{-1})=0$ if $\tau_i\mu^{x_i}\tau_i^{-1}$ is not in H , because μ^{x_i} and μ^{-x_i} cancel in the middle. So it is also

$$\sum_{i=1}^rf_i\chi_\rho((\tau_i\mu\tau_i^{-1})^n)$$

Notice that $(\tau_i\mu\tau_i^{-1})^n=[\frac{L/K}{\tau_i\mathfrak{p}}]^n$. It is in H iff it acts trivially in F . But $[\frac{L/K}{\tau_i\mathfrak{p}}]^n|_F=[\frac{L/K}{q_i}]^n$, which is trivial iff the order of $[\frac{L/K}{q_i}]$ divides n iff $f_i|n$

Thus each factor of $\log L(s,\rho^*,L/K)$ associated to \mathfrak{p} is

$$\begin{aligned}&\sum_{n=1}^{\infty}\frac{1}{n||\mathfrak{p}||^{ns}}\chi_{\rho^*}([\frac{L/K}{\mathfrak{p}}]^n)\\&=\sum_{i=1}^rf_i\sum_{n=1}^{\infty}\frac{1}{n||\mathfrak{p}||^{ns}}\chi_\rho((\tau_i\mu\tau_i^{-1})^n)\end{aligned}$$

But $\chi_\rho((\tau_i\mu\tau_i^{-1})^n)=0$ unless $f_i|n$. So it is summing over n that are multiples of f_i . Now take $n=f_it$, t running through all the positive integers. Then the sum is

$$\sum_{i=1}^r\sum_{t=1}^{\infty}\frac{f_i}{f_it||\mathfrak{p}||^{ts}}\chi_\rho(((\tau_i\mu\tau_i^{-1})^{f_i})^t)$$

But $||\mathfrak{p}||^{f_i}=||q_i||$, so $(\tau_i\mu\tau_i^{-1})^{f_i}=[\frac{L/K}{\tau_i\mathfrak{p}}]^{f_i}=[\frac{F/K}{q_i}]$. Thus the sum is

$$\sum_{i=1}^r\sum_{t=1}^{\infty}\frac{1}{t||q_i||^{ts}}\chi_\rho\left(\left([\frac{F/K}{q_i}]\right)^t\right)$$

This is the factor of $\log L(s,\rho,F/K)$ corresponds to q_i that are above \mathfrak{p} . So the proof is complete. □

We know L-series do not change under induction. We state a lemma that will be proven later.

Lemma 4.12. *Let ρ be an irreducible representation of G . Then χ_ρ is a rational linear combination of characters induced from the cyclic subgroups of G . Moreover, if ρ is non-trivial character, then it is a rational linear combination of characters induced from the non-trivial characters of cyclic subgroups of G .*

To be precise, let a denote the number of cyclic subgroups of G , and let i denote the i th cyclic subgroup. Let n_i denotes the cardinality of the i th cyclic subgroup H_i . For a fixed cyclic subgroup H_i , let ζ_{ij} be the irreducible (thus 1-dimensional) characters of H_i where j runs through 0 to n_i-1 , and ζ_{i0} is the trivial character. Then we have

$$\chi_\rho=\sum u_{ij}\zeta_{ij}^*$$

Where u_{ij} are rationals. When ρ is non-trivial representation on G , we can have $u_{i0}=0,\forall i$.

If we assume the lemma, we have

$$L(s,\rho,L/K)=\prod_{ij}L(s,\zeta_{ij},L/\Omega_i)^{u_{ij}}$$

where Ω_i is the fixed field of H_i . Moreover ζ_{ij} are all non-trivial. Since the cyclic group is abelian, we can apply what we proved in the abelian case: $L(s,\zeta_{ij},L/\Omega_i)$ is analytic and non-zero on $\text{Re}(s)\geq 1$, so we can take rational power of it in $\text{Re}(s)\geq 1$ and it is still analytic and non-zero, so the product $\prod_{ij}L(s,\zeta_{ij},L/\Omega_i)^{u_{ij}}$ is also non-zero and analytic here. Thus we prove the nice properties of $L(s,\rho,L/K)$ required.

Now the only thing left is to show the lemma.

Proof. Recall the Frobenius reciprocity we discussed in the background section:

Suppose H is a subgroup of G , and let ψ,ϕ be two class functions. Then we have

$$\langle\phi,Res_H^G\psi\rangle_H=\langle\phi^*,\psi\rangle_G$$

Let ψ_k run through the irreducible characters of G , $0\leq k\leq g-1$, and ψ_0 denote the trivial character. Since the induced character ζ_{ij}^* is a class function, we can have

$$\zeta_{ij}^*=\sum_kr_{jik}\psi_k$$

where r_{jik} are rationals. We also know the inner product $\langle\zeta_{ij}^*,\psi_k\rangle_G=r_{jik}$.By Frobenius reciprocity we have

$$\langle\zeta_{ij},Res_H^G\psi_k\rangle_H=\langle\zeta_{ij}^*,\psi_k\rangle_G=r_{jik}$$

Now restricting ψ_k to H_i is a character on H_i . So we have

$$\psi_k(\tau)=\sum_jb_{jik}\zeta_{ij}(\tau)$$

for $\tau\in H_i$. So $b_{jik}=\langle Res_H^G\psi_k,\zeta_{ij}\rangle_H=r_{jik}$. Now we have a system of equations

$$\zeta_{ij}^*=\sum_kr_{jik}\psi_k$$

Now if we collect these coefficients into a matrix, and let M be the matrix below:

$$\begin{bmatrix}r_{110}&\cdots&r_{11g}\\r_{210}&\cdots&r_{21g}\\\vdots&\ddots&\vdots\\r_{n_10}&\cdots&r_{n_1g}\\\vdots&\ddots&\vdots\\r_{n_g0}&\cdots&r_{n_gg}\end{bmatrix}$$

Then we have

$$\begin{bmatrix}\zeta_{11}^*\\\vdots\\\zeta_{1n_1}^*\\\zeta_{21}^*\\\vdots\\\zeta_{2n_2}^*\\\vdots\\\zeta_{g1}^*\\\vdots\\\zeta_{gn_g}^*\end{bmatrix}=M\begin{bmatrix}\psi_0\\\vdots\\\psi_g\end{bmatrix}$$

We wish to show that M has a left inverse, say M^* . Then

$$M^*\begin{bmatrix}\zeta_{11}^*\\\vdots\\\zeta_{gn_g}^*\end{bmatrix}=\begin{bmatrix}\psi_0\\\vdots\\\psi_g\end{bmatrix}$$

which exists if the rank of $M=\#$ columns of M . Suppose that rank of $M<g$, then the columns of M are linearly dependent. There exists $c_0,...,c_{g-1}$ not all zero such that

$$c_0r_{j10}+.....+c_{g-1}r_{jg-1}=0$$

for all j,i .

Now fix H_i and for any $\tau\in H_i$

$$\sum_{k=0}^{g-1}c_k\psi_k(\tau)=\sum_{k=0}^{g-1}c_k\sum_{j=0}^{n_i-1}r_{jik}\zeta_{ij}(\tau)=\sum_{j=0}^{n_i-1}\zeta_{ij}(\tau)\sum_{k=0}^{g-1}c_kr_{jik}=0$$

Since each element in G generates a cyclic group, each element is in some cyclic group H_i . Thus for all $\tau\in G$, $\sum_{k=0}^{g-1}c_k\psi_k(\tau)=0$. Thus $\sum_{k=0}^{g-1}c_k\psi_k=0$. Then $\psi_0,...,\psi_{g-1}$ are not linearly independent. But irreducible characters of G are linearly independent, so we derive a contradiction. Thus the rank of M is g , which shows that each ψ_k can be expressed as a rational combination of ζ_{ij}^* .

We have shown that $\psi_k=\sum_{i=1}^a\sum_{j=0}^{n_i-1}u_{ij}\zeta_{ij}^*$. We are going to show that if ψ_k is non-trivial then $u_{i0}=0$.

Proof. Fix H_i . By definition of induced character, we have that $\forall g\in G$

$$\sum_{j=0}^{n_i-1}\zeta_{ij}^*(g)=\sum_{t\in G,tgt^{-1}\in H_i}\sum_{j=0}^{n_i-1}\zeta_{ij}(tgt^{-1})\frac{1}{|H_i|}$$

Since ζ_{ij} runs through all characters of H_i , by the orthogonality relations of characters we know that

$$\sum_{j=0}^{n_i-1}\zeta_{ij}(tgt^{-1})=\begin{cases}0,&\text{if }tgt^{-1}\neq 1\\|H_i|,&\text{if }tgt^{-1}=1\end{cases}$$

But $tgt^{-1}=1$ iff $g=1$. Let's denote $\sum_{j=0}^{n_i-1}\zeta_{ij}(tgt^{-1})$ as $T_i(g)$. Then we know that $T_i(g)=0$ for $g\neq 1$, and is $|G|$ when $g=1$. Thus we know that

$$\zeta_{i0}^*=(\sum_{j=1}^{n_i-1}\zeta_{ij}^*)+T_i$$

Now consider ψ_k non-trivial character of G . We have that

$$\begin{aligned}\psi_k&=\sum_{i=1}^a\sum_{j=0}^{n_i-1}u_{ij}\zeta_{ij}^*\\&=\sum_{i=1}^au_{i0}T_i+\sum_{i=1}^a\sum_{j=1}^{n_i-1}(u_{ij}-u_{i0})\zeta_{ij}^*\end{aligned}$$

Now take the inner product with the trivial character ψ_0 . We know that

$$\langle\psi_k,\psi_0\rangle_G=\sum_{i=1}^au_{i0}\langle T_i,\psi_0\rangle_G+\sum_{i=1}^a\sum_{j=1}^{n_i-1}(u_{ij}-u_{i0})\langle\zeta_{ij}^*,\psi_0\rangle_G$$

But it is also 0. By Frobenius reciprocity, $\langle\zeta_{ij}^*,\psi_0\rangle_G=0$. So we have that

$$\begin{aligned}\langle\psi_k,\psi_0\rangle_G&=\sum_{i=1}^au_{i0}\langle T_i,\psi_0\rangle_G\\&=\sum_{i=1}^au_{i0}T_i(1)=0\end{aligned}$$

We already know that $\psi_k=\sum_{i=1}^a\sum_{j=1}^{n_i-1}u_{ij}\zeta_{ij}^*=\sum_{i=1}^au_{i0}T_i$. But $\sum_{i=1}^au_{i0}T_i$ takes 0 on $g\neq 1$ ($T_i(g)=0$ for each i) and also takes 0 on $g=1$. Therefore $\sum_{i=1}^au_{i0}T_i$ is identically zero. So we have $\psi_k=\sum_{i=1}^a\sum_{j=1}^{n_i-1}(u_{ij}-u_{i0})\zeta_{ij}^*$. This shows that ψ_k is a linear combination of characters introduced from non-trivial characters of cyclic subgroups of G , and we are done. □

5 Properties of Riemann zeta function and Riemann Hypothesis

The proof of the Prime Number Theorem reveals that the non-zero property of zeta function on $\text{Re}(s)=1$ gives the asymptotic formula for $\pi(x)$. The celebrated Riemann Hypothesis assumes a more precise distribution of zero of $\zeta(s)$: the non-trivial zeros are all on $\text{Re}(s)=\frac{1}{2}$. And this is expected to give a better error bound to the Prime Number Theorem. The equivalent statement, or say a well-known consequence of Riemann Hypothesis is that, (Assuming Riemann Hypothesis),

$$\pi(x)=Li(x)+\mathcal{O}(\sqrt{x}\log x)$$

For the statement of Riemann Hypothesis to even make sense, we need to first define Riemann zeta function on the entire complex plane.

5.1 Gamma function and some of its properties

Let's start by defining Gamma function, a component in the functional equation and in meromorphic extension for $\zeta(s)$.

Definition 5.1. $\Gamma(s)=\int_0^\infty e^{-t}t^{s-1}dt$ for $\text{Re}(s)>0$

First notice that this is a well defined function. Say $\text{Re}(s)=\varepsilon>0$, then

$$|\Gamma(s)|=\left|\int_0^\infty e^{-t}t^{s-1}dt\right|\leq\int_0^\infty e^{-t}t^{\varepsilon-1}dt=\int_1^\infty e^{-t}t^{\varepsilon-1}dt+\int_0^1 e^{-t}t^{\varepsilon-1}dt$$

$\int_0^\infty e^{-t}t^{s-1}dt$ always converges, and $\int_0^1 e^{-t}t^{s-1}dt = \mathcal{O}(\int_0^1 t^{s-1})$, which converges when $s > 0$. Thus the integral converges absolutely when $\text{Re}(s) > 0$

As $s \rightarrow 0$, $\int_0^1 e^{-t}t^{s-1}dt$ goes to infinity. So as for $\text{Re}(s) \leq 0$, we need other definition of $\Gamma(s)$

Below are two ways to extend the function. Each of them gives some property of $\Gamma(s)$.

1. Extension by "integrating by parts"

For $\text{Re}(s) > 0$, $\int_0^\infty e^{-t}t^s dt$. By integrating by parts, we have

$$\frac{\Gamma(s+1)}{s} = \Gamma(s)$$

For $-1 < \text{Re}(s) \leq 0$, $\frac{\Gamma(s+1)}{s} = \Gamma(s)$, $s \neq 0$ is well defined and analytic. For $s = 0$, $\Gamma(s+1) = \Gamma(1) = 1$, so $\frac{\Gamma(s+1)}{s} = \Gamma(s)$ will have simple pole at $s = 0$. Thus for $-1 < \text{Re}(s) \leq 0$, we can define $\Gamma(s)$ as $\frac{\Gamma(s+1)}{s}$. We obtain a meromorphic extension of $\Gamma(s)$ to $\text{Re}(s) > -1$. But now we can extend it to $-2 < \text{Re}(s) \leq -1$ in a similar way. Repeating the same process we can define Γ on the entire complex plane:

$$\Gamma(s) = \begin{cases} \int_0^\infty e^{-t}t^{s-1}dt, & \text{Re}(s) > 0 \\ \frac{\Gamma(s+k+1)}{s(s+1)\dots(s+k)}, & -k-1 < \text{Re}(s) \leq -k, k \in \mathbb{Z}^+ \cup \{0\} \end{cases}$$

From the above formula we can find out that the poles of $\Gamma(s)$ are 0 and all the negative integers, but we can't get accurate information about zeros. Here the product representation of $\Gamma(s)$ will tell us clearly that $\Gamma(s)$ is no-where 0.

Since

$$\lim_{n \rightarrow \infty} (1 - \frac{t}{n})^n \rightarrow e^{-t}$$

and the convergence is uniform, we can plug it into the integral representation of $\Gamma(s)$ and we get

$$\Gamma(s) = \lim_{n \rightarrow \infty} \int_0^n t^{s-1} (1 - \frac{t}{n})^n dt$$

By integrating by parts, this is

$$\lim_{n \rightarrow \infty} \frac{1}{n^n} \cdot \frac{n}{s} \cdot \int_0^n t^s (n-t)^{n-1} dt$$

Repeating the same process, we can get the expression of $\Gamma(s)$:

$$\begin{aligned} \lim_{n \rightarrow \infty} \frac{1}{n^n} \cdot \frac{n}{s} \cdot \frac{n-1}{s+1} \cdot \dots \cdot \frac{1}{s+n-1} \cdot \int_0^n t^{s+n-1} dt \\ = \lim_{n \rightarrow \infty} \frac{1}{n^n} \cdot \frac{n}{s} \cdot \dots \cdot \frac{1}{s+n-1} \cdot \frac{n}{s+n} \\ = \lim_{n \rightarrow \infty} \frac{n^s}{s} \cdot \frac{1}{s+1} \cdot \frac{2}{s+2} \dots \frac{n}{s+n} \end{aligned}$$

This product converges for $\text{Re}(s) > 0$. Now insert a "convergenve factor" to make this product converge everywhere.

Lemma 5.2.

$$\lim_{n \rightarrow \infty} \sum_{k=1}^n \frac{1}{k} - \log n \text{ exists}$$

Proof. Write $\log n$ as

$$(\log 2 - \log 1) + (\log 3 - \log 2) + \dots + (\log n - \log n-1)$$

So when n is finite , the sum is

$$\sum_{k=1}^{n-1} \frac{1}{k} - \log \frac{k+1}{k} + \frac{1}{n}$$

Use the Taylor expansion of $\log(1 + \frac{1}{k})$

$$\log(1 + \frac{1}{k}) = \frac{1}{k} - \frac{1}{2k^2} + \frac{1}{3k^3} - \frac{1}{4k^4} + \dots$$

Thus we have

$$\frac{1}{k} - \log(1 + \frac{1}{k}) = \frac{1}{2k^2} - \frac{1}{3k^3} + \frac{1}{4k^4} + \dots$$

Which is less than $\frac{1}{2k^2}$

Thus

$$\sum_{k=1}^{n-1} \frac{1}{k} - \log \frac{k+1}{k} + \frac{1}{n} \leq \sum_{k=1}^{n-1} \frac{1}{2k^2} + \frac{1}{n}$$

Take the limit as $n \rightarrow \infty$, $\sum_{k=1}^{n-1} \frac{1}{2k^2} + \frac{1}{n}$ converges. Also $\frac{1}{k} - \log \frac{k+1}{k} \geq 0$. Thus the limit exists. We denote the limit as γ , the Euler constant. \square

Now go back to $\Gamma(s)$. From the product representation of $\Gamma(s)$ we know that

$$\frac{1}{\Gamma(s)} = \lim_{n \rightarrow \infty} sn^{-s} \prod_{k=1}^n (1 + \frac{s}{k})$$

$$= \lim_{n \rightarrow \infty} s \cdot e^{s(\sum_{k=1}^n \frac{1}{k} - \log n)} \prod_{k=1}^n (1 + \frac{s}{k})e^{-\frac{s}{k}}$$

$$= se^{s\gamma} \prod_{k=1}^{\infty} (1 + \frac{s}{k})e^{-\frac{s}{k}}$$

Which converges everywhere. Thus we can take

$$\frac{1}{se^{s\gamma} \prod_{k=1}^{\infty} (1 + \frac{s}{k})e^{-\frac{s}{k}}}$$

as the meromorphic extension of $\Gamma(s)$ to the entire complex plane. This product representation shows that $\Gamma(s)$ is non-where 0.

5.2 Analytic continuation of $\zeta(s)$

Now we are in a good position to define the analytic continuation of $\zeta(s)$ to the entire complex plane.

When $\text{Re}(s) > 0$,

$$\int_0^\infty e^{-nt}t^{s-1}dt = \frac{1}{n^s} \int_0^\infty e^{-t}t^{s-1}dt = \frac{\Gamma(s)}{n^s}dt$$

Since the integral converges absolutely. Then

$$\lim_{n \rightarrow \infty} \sum_{k=1}^n \int_0^\infty e^{-kt}t^{s-1}dt = \lim_{n \rightarrow \infty} \sum_{k=1}^n \frac{1}{k^s} \int_0^\infty e^{-t}t^{s-1}dt = \Gamma(s)\zeta(s)$$

But on the other hand we also have

$$\lim_{n \rightarrow \infty} \sum_{k=1}^n \int_0^\infty e^{-kt}t^{s-1}dt = \int_0^\infty \sum_{k=1}^n e^{-kt}t^{s-1}dt = \int_0^\infty \frac{t^{s-1}}{e^t-1}dt$$

Thus we have for $\text{Re}(s) > 1$

$$\zeta(s) = \frac{1}{\Gamma(s)} \int_0^\infty \frac{t^{s-1}}{e^t-1}dt$$

For $\text{Re}(s) \leq 0$ consider

$$\int_0^\infty \frac{t^{s-1}}{e^t-1}dt = \int_1^\infty \frac{t^{s-1}}{e^t-1}dt + \int_0^1 \frac{t^{s-1}}{e^t-1}dt$$

The integral on $[1, \infty)$ certainly converges. For $\int_0^1 \frac{t^{s-1}}{e^t-1}dt$, consider the Laurent expansion

$$\frac{1}{e^t-1} = \frac{1}{t} + A_0 + A_1t + A_2t^2 + \dots$$

Where A_i are constant. The expression converges at $t = 1$. Apply Laurent expansion we get

$$\int_0^1 \frac{t^{s-1}}{e^t-1}dt = \frac{1}{s-1} + \frac{A_0}{s} + \frac{A_1}{s+1} + \dots$$

Which is analytic except for possible simple poles at $s = 1, 0, -1, -2, \dots$. Now we can take

$$\zeta(s) = \frac{1}{\Gamma(s)} \int_0^\infty \frac{t^{s-1}}{e^t-1}dt$$

As the meromorphic extension of $\zeta(s)$ to the entire complex plane. Also $\frac{1}{\Gamma(s)}$ has simple zeros at $s = 0, -1, -2, \dots$, which cancel out the possible simple poles of $\int_0^1 \frac{t^{s-1}}{e^t-1}dt$ except for at $s = 1$. So the meromorphic extension of $\zeta(s)$ to the entire complex plane is analytic everywhere except for a simple pole at $s = 1$.

5.3 Trivial zeros of $\zeta(s)$

Now that we have analytic extension of $\zeta(s)$, it's time to consider its zeros. Consider the Laurent Expansion

$$\frac{1}{e^t-1} = \frac{1}{t} + A_0 + A_1t + A_2t^2 + \dots$$

$$\frac{1}{e^{-t}-1} = -\frac{1}{t} + A_0 - A_1t + A_2t^2 - \dots$$

Summing up the two equations we get

$$-1 = 2A_0 + 2A_2t^2 + 2A_4t^4 + \dots$$

This forces A_{2k} to be 0 for k positive integers. Now plug $s = -2k$ ($k \geq 1$) into expression of $\zeta(s)$, we have

$$\zeta(s) = \frac{1}{\Gamma(-2k)} \left(\frac{1}{-2k-1} + \frac{A_0}{-2k} + \frac{A_1}{-2k+1} + \dots + \int_1^\infty \frac{t^{s-1}}{e^t-1}dt \right)$$

The pole at $\frac{-A_0}{-2k+2k}$ is cancelled by $A_{2k} = 0$ and $\frac{1}{\Gamma(-2k)} = 0$. Thus $\zeta(-2k) = 0$. Thus even negative integers are zeros of $\zeta(s)$. It turns out that they are the only zeros on the region $\text{Re}(s) \geq 1$ and $\text{Re}(s) \leq 0$, and we are going to show this by deriving a functional equation that $\zeta(s)$ satisfies.

5.4 The functional equation of $\zeta(s)$ and the proof from Riemann's original paper

Consider

$$\phi(s) = \frac{1}{2}s(s-1)\pi^{-\frac{1}{2}s}\Gamma(\frac{1}{2}s)\zeta(s)$$

$\phi(s)$ is analytic everywhere since the pole of $\zeta(s)$ is cancelled by $(s-1)$ and the pole of $\Gamma(\frac{1}{2}s)$ is cancelled by the trivial zeros of $\zeta(s)$ and s .

Theorem 5.3. $\phi(s)$ satisfies the functional equation

$$\phi(s) = \phi(1-s)$$

Let's see what happens if the functional equation is true. Say

$$\frac{1}{2}s(s-1)\pi^{-\frac{1}{2}s}\Gamma(\frac{1}{2}s)\zeta(s) = \frac{1}{2}s(s-1)\pi^{-\frac{1}{2}(1-s)}\Gamma(\frac{1-s}{2})\zeta(1-s) \quad (8)$$

When $\text{Re}(s) \leq 0$, $\text{Re}(1-s) \geq 1$. So $\zeta(1-s)$ and $\Gamma(\frac{1-s}{2})$ are non-zero. s is cancelled by the pole of $\zeta(1-s)$ at $s = 0$. Thus the left of equation (8) is zero-free, and so should be the right. That means that for $\text{Re}(s) \leq 0$, the zero of $\zeta(s)$ can only appear at the pole of $\Gamma(\frac{1}{2}s)$. Also $\zeta(s) \neq 0$ for $s = 0$ because the simple pole of $\Gamma(\frac{1}{2}s)$ there is cancelled by s . This means the zeros of $\zeta(s)$ on $\text{Re}(s) \leq 0$ are exactly the negative even integers $s = -2, -4, \dots$.

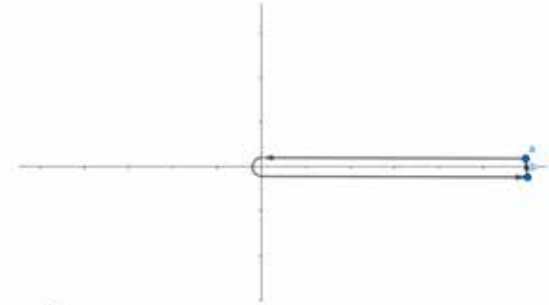
Moreover, for $0 < \text{Re}(s) < 1$, s is a zero of $\zeta(s)$ iff it's a zero of $\zeta(1-s)$ because other factors in $\phi(s)$ and $\phi(1-s)$ are analytic and non-zero. Thus the zeros of $\zeta(s)$ in $0 < \text{Re}(s) < 1$ is symmetric of $s = \frac{1}{2}$.

Riemann proved the functional equation of $\zeta(s)$ in the first page of [3], which is illustrated as below. The basic idea is to consider

$$\int_{-\infty}^{\infty} \frac{(-x)^{s-1}}{e^x-1}dx \quad (9)$$

for $s < 0$ and compute the integral on two contours.

The first way is to take a contour starting from a point a that is above x on real line by distance ε ; then go all the way to 0, and then go to point b that is below x by distance ε , and eventually go back to a . We denote this contour as P_1 . Equation 9 is the integral on this contour when $M \rightarrow \infty$ and $\varepsilon \rightarrow 0$.



Since

$$a = xe^{x+\varepsilon i}, \quad b = xe^{-x-\varepsilon i}$$

we have

$$-a = xe^{x+\varepsilon i}, \quad -b = xe^{x-\varepsilon i}$$

So

$$(-a)^{s-1} = e^{(s-1)\log x + (s-1)(\pi+\varepsilon)i}$$

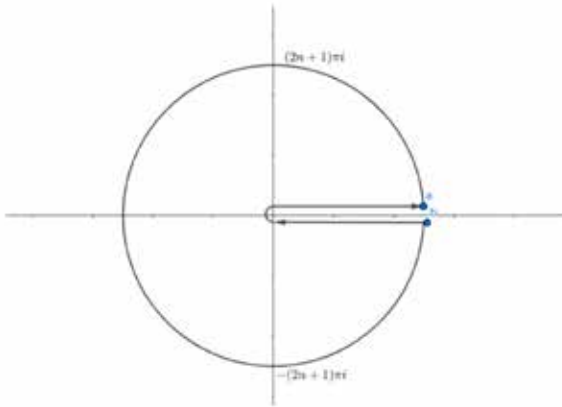
Here we take the angle of $\log x$ to be between πi and $-\pi i$, so the $\log x$ is continuous on positive real axis and has discontinuity on negative real axis. P_1 on the positive half plane so the logarithm function is continuous. The integral along P_1 is

$$\lim_{x \rightarrow \infty, \varepsilon \rightarrow 0} \int_0^x \frac{(-a)^{s-1}}{e^a-1}da + \int_x^0 \frac{(-b)^{s-1}}{e^b-1}db$$

When we take the limit, e^a-1, e^b-1 will be very closed to e^x-1 . So the integral will be

$$\begin{aligned} \lim_{x \rightarrow \infty, \varepsilon \rightarrow 0} \int_0^\infty \frac{(-a)^{s-1} - (-b)^{s-1}}{e^a-1}dx \\ = \frac{x^{s-1}(e^{(s-1)\pi i} - e^{-(s-1)\pi i})}{e^x-1}dx \\ = (e^{-\pi si} - e^{\pi si}) \int_0^\infty \frac{x^{s-1}}{e^x-1}dx \\ = -2i \sin \pi s \zeta(s) \Gamma(s) \end{aligned} \quad (10)$$

Another way to evaluate the integral $\int_{-\infty}^{\infty} \frac{(-x)^{s-1}}{e^x-1}dx$ is to consider the contour that starts from a little bit above $(2n+1)\pi$ and goes counterclockwise along the circle with radius $(2n+1)\pi$ and center as origin until a little bit below $(2n+1)\pi$. Then goes left all the way to the origin, goes above the positive real axis and back to where we start. We denote this path as P_2 .



We also denote the contour going counterclockwise of the circle as C . Then

$$P_2 = C - P_1$$

Also notice that $\frac{(-x)^{s-1}}{e^x-1}$ is analytic along P_2 because the poles only appear at $2n\pi i$, which is not on P_2

Now as $n \rightarrow \infty$, the integral of $\frac{(-x)^{s-1}}{e^x-1}$ along C tends to 0. We show this by $M-L$ estimation.

First find an upper bound for $|\frac{1}{e^x-1}|$. This is the same as finding a lower bound for $|e^x-1|$. Since e^x-1 is continuous, $\exists \varepsilon$ such that if $|y - (2n+1)\pi i| < \varepsilon$, then we have $|e^y-1| - (-1-1)| < \frac{1}{4}$, which means $\frac{7}{4} < |e^y-1| < \frac{9}{4}$. Now take a circle C_1 with center at $(2n+1)\pi$ and radius ε . On C_1 , $|\frac{1}{e^x-1}|$ is bounded from above. So as the circle C_2 with radius ε and center $-(2n+1)\pi i$. Now say C_1, C_2 intersect the big circle at points with x-coordinate t . So for $-t < \text{Re}(x) < t$, $\frac{1}{e^x-1}$ is bounded from above.

For $t \leq \text{Re}(x) < (2n+1)\pi$ and $-(2n+1)\pi < \text{Re}(x) \leq -t$, $|\frac{1}{e^x-1}|$ is bounded above by $\frac{1}{e^t-1}$. Thus on the entire circle, $|\frac{1}{e^x-1}|$ is bounded from above, say, by c .

The upperbound for $|(-x)^{s-1}|$ is $((2n+1)\pi)^{s-1}$

Thus by $M-L$ estimation, we have

$$\int_C \frac{(-x)^{s-1}}{e^x-1}dx \leq (4n+2)\pi^2((2n+1)\pi)^{s-1}c$$

But $\text{Re}(s) < 0$ by our assumption, so the exponent is negative. Since the integral of an entire function doesn't depend on its path, we can take $n \rightarrow \infty$, then $(4n+2)\pi^2((2n+1)\pi)^{s-1}C \rightarrow 0$. Thus the integral in 8 can only be 0.

Therefore

$$-\int_{P_1} \frac{(-x)^{s-1}}{e^x-1}dx = \int_{P_2} \frac{(-x)^{s-1}}{e^x-1}dx$$

On the other hand, by residue theorem,

$$\int_{P_2} \frac{(-x)^{s-1}}{e^x-1}dx = 2\pi i (\sum \text{residues}) \quad (11)$$

The poles inside P_2 are at $s = 0, \pm 2\pi i, \pm 4\pi i, \dots, \pm 2n\pi i$ for radius being $(2n+1)\pi$. For a pole at $2k\pi i$, the residue is:

$$\lim_{x \rightarrow 2k\pi i} \frac{(-x)^{s-1}(x-2k\pi i)}{e^x-1} = \lim_{x \rightarrow 2k\pi i} \frac{(-2k\pi i)^{s-1}}{\frac{e^x-e^{2k\pi i}}{x-2k\pi i}} = (-2k\pi i)^{s-1}$$

Plug this into equation (11), we have

$$\begin{aligned} \int_{-\infty}^{\infty} \frac{(-x)^{s-1}}{e^x-1}dx &= -2\pi i \sum_{n=1}^{\infty} [(-2n\pi i)^{s-1} + (2n\pi i)^{s-1}] \\ &= -2\pi i \cdot 2^{s-1}(i^{s-1} + (-i)^{s-1}) \cdot \sum_{n=1}^{\infty} \frac{1}{n^{1-s}} \end{aligned}$$

Equate the two expression for $\int_{-\infty}^{\infty} \frac{(-x)^{s-1}}{e^x-1}dx$, we get that

$$\sin \pi s \zeta(s) \Gamma(s) = (2\pi)^s \zeta(1-s) \sin \frac{\pi s}{2} \quad (12)$$

Here we cite two functional equations of $\Gamma(s)$ from page 250 of [17]:

$$\Gamma(\frac{1+s}{2})\Gamma(\frac{1-s}{2}) = \frac{\pi}{\cos \frac{\pi s}{2}}$$

$$\Gamma(\frac{s}{2})\Gamma(s + \frac{1}{2}) = \sqrt{2}\pi 2^{\frac{1}{2}-s}\Gamma(s)$$

Both of the above equations can be derived from the product presentation of $\Gamma(s)$. Plug

$$\Gamma(s) = \frac{\Gamma(\frac{s}{2})}{\sqrt{2\pi} 2^{\frac{1}{2}-s} \cos \frac{\pi s}{2} \Gamma(\frac{1-s}{2})}$$

into equation (12) and do some algebraic manipulation, we will eventually get

$$\pi^{-\frac{s}{2}}\zeta(s)\Gamma(\frac{s}{2}) = \pi^{\frac{s-1}{2}}\zeta(1-s)\Gamma(\frac{1-s}{2})$$

Thus $\phi(s) = \frac{1}{2}s(s-1)\pi^{-\frac{s}{2}}\zeta(s)\Gamma(\frac{s}{2})$ will have the property that $\phi(s) = \phi(1-s)$ for $\text{Re}(s) < 0$. But both $\phi(s)$ and $\phi(1-s)$ are analytic on the entire complex plane. So if they agree on $\text{Re}(s) < 0$, they will agree on the entire complex plane. Thus we finish the proof for the functional equation for $\zeta(s)$

We have some other facts about the zeros of $\zeta(s)$. $\zeta(s)$ has infinitely many zeros in the critical strip, and the number of zeros of $\zeta(s)$ in the rectangle $0 < \text{Re}(s) < 1, 0 < \text{Im}(s) < T$, denoted as $N(T)$, is approximately $\frac{T}{2\pi} \log \frac{T}{2\pi} - \frac{T}{2\pi}$. Readers can refer to page 19 of [6] for detailed proof.

5.5 Riemann's Hypothesis and the error of the Prime Number Theorem

We mentioned earlier an equivalent statement of Riemann's Hypothesis: All zeros of $\zeta(s)$ in critical strip are on $\text{Re}(s) = \frac{1}{2}$ iff $\pi(x) = Li(x) + \mathcal{O}(\sqrt{x} \log x)$. Let's see why the equivalence should be true.

Recall our proof for asymptotic formula for prime number theorem. We were largely dealing with $\psi(x)$ and we didn't get into $\pi(x)$ until the very last moment. Let's follow the same procedure here. For the sake of convenience let us define one more arithmetic function besides $\psi(x), \Lambda(x)$.

Definition 5.4. We define $\theta(x)$ such that

$$\theta(x) = \sum_{p \leq x} \log p$$

Notice that by definition of $\psi(x), \theta(x)$,

$$\psi(x) = \theta(x) + \theta(x^{\frac{1}{2}}) + \theta(x^{\frac{1}{3}}) + \dots + \theta(x^{\frac{1}{x}})$$

Where $x^{\frac{1}{x}} \geq 2$ and $x^{\frac{1}{x+1}} < 2$. But

$$\psi(x) - \theta(x) \leq m\theta(x^{\frac{1}{2}}) \leq \frac{\log x}{\log 2} \theta(x^{\frac{1}{2}})$$

Also we cite the fact that $\theta(x) = \mathcal{O}(x)$ from page 83 of ([17]). So we know that

$$\psi(x) - \theta(x) = \mathcal{O}(\sqrt{x} \log x)$$

This difference is way smaller than $\frac{x}{\log x}$. We can see in the following sketch of proof that this error is always smaller than $\psi(x) - x$, so we if we can get the error bound for $\psi(x) - x$, we can get it for $\theta(x) - x$.

The reason we use $\psi(x)$ is that we actually have a very precise formula for $\psi(x)$ which gives us insight of how the location of zero can determine the error bound of the Prime Number Theorem. This is the Von-Mangoldt's formula:

$$\psi(x) = x - \sum_{\rho} \frac{x^{\rho}}{\rho} + \sum_{n=1}^{\infty} \frac{x^{-2n}}{2n} - \frac{\zeta(0)'}{\zeta(0)} \quad (x > 1) \quad (13)$$

Where ρ is the zero of $\zeta(s)$ inside critical strip. This formula can be derived by evaluating the integral $\frac{1}{2\pi i} \int_{a-i\infty}^{a+i\infty} -\frac{\zeta'(s)}{\zeta(s)} \frac{x^s}{s} ds$ in two ways, one way gives $\psi(x)$ and the other way gives the right of equation (13). The detailed proof of this formula is in chapter 3 of [6].

As we can see, $\psi(x) - x$ consists of a constant, $-\sum_{\rho} \frac{x^{\rho}}{\rho}$ where ρ is the zeros in the critical strip, and $-\sum_{\rho} \frac{x^{\rho}}{\rho}$ when ρ is the trivial zeros.

Notice that $-\sum_{\rho} \frac{x^{\rho}}{\rho}$ behaves even nicer than the constant as it will get smaller when $x \rightarrow \infty$. So it contributes nothing to the error $\psi(x) - x$ (That's why we say these zeros are trivial). Therefore, the error term is dominated by $\sum_{\rho} \frac{x^{\rho}}{\rho}$ because they gets infinite as $x \rightarrow \infty$. We can see from here that $\zeta(s)$ being non-zero on $\text{Re}(s) = 1$ is crucial to the proof of $\psi(x) \sim x$: If $\zeta(s)$ has a zero on $\text{Re}(s) = 1$ then $\sum_{\rho} \frac{x^{\rho}}{\rho}$ would no longer be a minor term compare to x , and the asymptotic formula is no longer true.

Now say we want to minimize the error of approximating $\pi(x)$ by $Li(x)$, which is $|\pi(x) - Li(x)|$. Since we derive $\pi(x)$ from $\psi(x)$ we would hope to minimize $\psi(x) - x$, which is to minimize $\sum_{\rho} \frac{x^{\rho}}{\rho}$. Since the real part of ρ determines how x^{ρ} grows, we may hope that $\text{Re}(\rho)$ to very closed to 0. However, we proved in the functional equation that zeros appear in pairs: if ρ is a zero in the critical strip then $1 - \rho$ will also be a zero. So if $\text{Re}(\rho)$ is far from $\frac{1}{2}$, either ρ or $1 - \rho$ would have big real part. Therefore, the best hope for us is that all the zeros of $\zeta(s)$ has real part being $\frac{1}{2}$, and this is why we care about Riemann Hypothesis: It gives the smallest error bound for $\psi(x) - x$ and thus $\pi(x) - Li(x)$.

To go from here, if we assume that Riemann Hypothesis is true, then we can bound $\psi(x)$ by

$$\int_{x-1}^x \psi(t) dt \leq \psi(x) \leq \int_x^{x+1} \psi(t) dt$$

Then plug in Mangold's formula and that $\rho = \frac{1}{2} + it$. We can ignore $-\frac{\zeta(0)'}{\zeta(0)} + \sum_{n=1}^{\infty} \frac{x^{-2n}}{2n}$.

Now we need to use the fact that the vertical density of zeros is less than $2 \log T$. i.e., for large enough T , the number of zeros ρ for $T \leq \text{Im}(\rho) \leq T+1$ is less than $2 \log T$, and the proof is given in page 71 of [6]. This ensure that there won't be too many zeros anyway, so when we sum up the terms $\frac{x^{\rho}}{\rho}$ it is dominant by \sqrt{x} . Eventually we can get the following bound:

$$x - C\sqrt{x} \log x^2 \leq \int_{x-1}^x \psi(t) dt \leq \psi(x) \leq \int_x^{x+1} \psi(t) dt \leq x + C\sqrt{x} \log x^2$$

Where the \sqrt{x} comes from estimating $|(x+1)^{\rho} - x^{\rho}|$ and $\log x^2$ comes from summing up the term $|\frac{1}{\rho(\rho+1)}|$, where we need the vertical density of zeros. Now we have that

$$\psi(x) = x + \mathcal{O}(\sqrt{x} \log x^2)$$

The error term here is less than $\psi(x) - \theta(x)$, so we also have that

$$\theta(x) = x + \mathcal{O}(\sqrt{x} \log x^2)$$

To go from $\theta(x)$ to $\pi(x)$, Notice that

$$\pi(x) = \sum_{2 \leq n \leq x} \frac{\theta(n) - \theta(n-1)}{\log n}$$

And $Li(x) = \int_2^x \frac{1}{\log t} dt$. The upper Riemann sum $Li^*(x)$ is

$$\int_2^3 \frac{1}{\log 2} + \int_3^4 \frac{1}{\log 3} + \dots + \int_{[x]-1}^{[x]} \frac{1}{\log [x]-1} + \int_{[x]}^x \frac{1}{\log [x]} = \sum_{n=2}^{[x]-1} \frac{1}{\log n} + \frac{x - [x]}{\log [x]}$$

Then we have

$$\pi(x) - Li^*(x) = \sum_{n=2}^{[x]} \frac{\theta(n) - \theta(n-1) - 1}{\log n} + \mathcal{O}(1)$$

Apply Abel's identity:

$$\sum_{n=2}^{[x]} \frac{\theta(n) - \theta(n-1) - 1}{\log n} + \mathcal{O}(1) = \frac{\theta(x) - x}{\log x} + \int_2^{[x]} \frac{\theta(t) - t}{t \log t^2} + \mathcal{O}(1)$$

Then plug in $\theta(x) - x = \mathcal{O}(\sqrt{x} \log x)$, we can get that

$$|\pi(x) - Li^*(x)| \leq C\sqrt{x} \log x$$

Similarly, let $Li_*(x)$ denote the lower Riemann sum of $Li(x)$, we can get $|\pi(x) - Li_*(x)| \leq C\sqrt{x} \log x$. Thus we get

$$|\pi(x) - Li(x)| \leq \mathcal{O}(\sqrt{x} \log x)$$

So assuming the Riemann Hypothesis, we get the intended bound.

6 Artin's conjecture on primitive roots

Recall that

$$\zeta_K(s) = \sum_{n=1}^{\infty} \frac{j_n}{n^s} = \sum_{I \in \mathcal{O}_K} \frac{1}{|I|}$$

Where j_n is the number of I such that $|I| = n$. This is a natural extension of Riemann zeta function which shares lots of asymptotic behavior with $\zeta(s)$. It turns out that $\zeta_K(s)$ also has meromorphic extension to the entire complex plane and also satisfies a functional equation. The proof involves use of higher dimensional Gamma function. Readers can refer to page 7 of [18] for detailed proof. It should be not surprising that $\zeta_K(s)$ has its own version of Riemann Hypothesis. This is the Generalized Riemann Hypothesis:

Let ρ be zeros of $\zeta_K(s)$ such that $0 < \text{Re}(\rho) < 1$, then $\text{Re}(\rho) = \frac{1}{2}$.

6.1 Artin's conjecture on primitive roots

Here we will present a corollary of generalized Riemann Hypothesis: Artin's conjecture on primitive roots

Definition 6.1. We say that a is a primitive root mod p if the order of a mod p is $p-1$. i.e., $a^{\frac{p-1}{q}} \not\equiv 1 \pmod{p}$ for any prime $q|p-1$.

Then the Artin's conjecture on primitive roots is stated as follow:

For any $a \in \mathbb{Z}$ such that $a \neq 0, \pm 1$ or any perfect square, there exists infinitely many primes p such that a is a primitive root mod p . What's more, fix a , denote $N_a(x)$ as the number of primes $p \leq x$ such that a is a primitive root mod p , then we have the following asymptotic formula:

$$N_a(x) \sim A(a) \frac{x}{\log x}$$

In which $A(a)$ is a non-zero constant depending on a .

Artin's primitive root conjecture was proven by Hooley in 1967 assuming the generalized Riemann Hypothesis and the proof is contained in [7]. In fact he gets an error bound for $N_a(x)$:

$$N_a(x) = A(a) \frac{x}{\log x} + \mathcal{O}\left(\frac{x \log \log x}{\log x^2}\right)$$

And he gave an expression for $A(a)$. I will present intuition and a sketch of how the proof uses generalized Riemann's Hypothesis, but the computational details will be omitted. Here we define some notations that are going to be used in the proof:

$R(q, p)$ denotes the event that " $p \equiv 1 \pmod{q}$ and $a^{\frac{p-1}{q}} \equiv 1 \pmod{p}$ ". Notice that a is a primitive root mod p iff $R(p, q)$ doesn't happen for any prime q .

$P_a(x, k)$ (k is square free) denotes the number of $p \leq x$ such that $R(p, q)$ holds for any prime $q|k$.

Lemma 6.2. If k_1, k_2 are co-prime and square-free, then p is counted by $P_a(x, k_1 k_2)$ iff p is counted by $P_a(x, k_1)$ and $P_a(x, k_2)$

Proof.

$$p \text{ is counted by } P_a(x, k_1) \text{ iff } \forall q|k_1 \begin{cases} p \equiv 1 \pmod{q} \\ a^{\frac{p-1}{q}} \equiv 1 \pmod{p} \end{cases}$$

And by Bezout's lemma, for two primes q_1, q_2 that are co-prime, we have

$$a^{\frac{p-1}{q_1}} \equiv 1 \pmod{p} \text{ and } a^{\frac{p-1}{q_2}} \equiv 1 \pmod{p} \text{ iff } a^{\frac{p-1}{q_1 q_2}} \equiv 1 \pmod{p}$$

By Chinese Remainder theorem, for two primes q_1, q_2 that are co-prime, we have

$$p \equiv 1 \pmod{q_1} \text{ and } p \equiv 1 \pmod{q_2} \text{ iff } p \equiv 1 \pmod{q_1 q_2}$$

Since k_1 is square free, each of its prime factor is co-prime to others, so we have

$$a^{\frac{p-1}{k_1}} \equiv 1 \pmod{p} \text{ and } p \equiv 1 \pmod{k_1}$$

Same for k_2 . But now k_1, k_2 is co-prime. So by the same reasoning, p is counted by $P_a(x, k_1)$ and $P_a(x, k_2)$ iff

$$a^{\frac{p-1}{k_1 k_2}} \equiv 1 \pmod{p} \text{ and } p \equiv 1 \pmod{k_1 k_2}$$

Which is true iff p is counted in $P_a(x, k_1 k_2)$

Since by definition,

$N_a(x) =$ the number of $p \leq x$ - the number of $p \leq x$ such that $R(p, q)$ holds for some q

Then by inclusion-exclusion principle, the number of $p \leq x$ that satisfies $R(p, q)$ for some prime q is:

$$\sum_i P_a(x, q_i) - \sum_{i,j} P_a(x, q_i q_j) + \sum_{i,j,k} P_a(x, q_i q_j q_k) + \dots = - \sum_{k=2}^{\infty} P_a(x, k) \mu(k)$$

And we can think of $P_a(x, 1)$ as the number of all the primes $p \leq x$. Then we have

$$N_a(x) = \sum_{k=1}^{\infty} P_a(x, k) \mu(k)$$

So we have expression of $N_a(x)$ in terms of $P_a(x, k)$. But what exactly is $P_a(x, k)$? It turns out that $P_a(x, k)$ can be categorized in terms of algebraic extension.

6.2 Categorizing $P_a(x, k)$ by algebraic number theory

First if a is an h th power (h must be odd because a is not a square), we take $k_1 = \frac{k}{(h,k)}$. We do this essentially because we want $x^{k_1} - a$ to be irreducible.

Now

$$p \text{ counted by } P_a(x, k) \text{ iff for all } q|k \begin{cases} p \equiv 1 \pmod{q} \\ a^{\frac{p-1}{q}} \equiv 1 \pmod{p} \end{cases} \text{ i.e., } a \text{ is a } q\text{th power mod } p$$

But if $q|h$, then a is automatically a q th power. So essentially we only need to ensure that

$$p \equiv 1 \pmod{k} \text{ and } a^{\frac{p-1}{k_1}} \equiv 1 \pmod{p}$$

Now consider $\mathbb{Q}(\zeta^m)/\mathbb{Q}$ and $\text{Gal } \mathbb{Q}(\zeta^m)/\mathbb{Q} = G$. We have shown that $p \equiv 1 \pmod{k}$ iff p splits completely in $\mathbb{Q}(\zeta^m)/\mathbb{Q}$

$a^{\frac{p-1}{k_1}} \equiv 1 \pmod{p}$ iff a is a k_1 th power iff $u^{k_1} - a$ has a solution in \mathbb{F}_p^* . From basic number theory we know that $u^{k_1} - a$ has a solution iff it has k_1 solutions, which happens iff $u^{k_1} - a$ splits into linear factor in \mathbb{F}_p^* .

Here we cite a lemma from algebraic number theory which is proven in [10]

Lemma 6.3. Let α to be an algebraic integer and $f(x)$ is the minimal polynomial of α . For $p \nmid [\mathbb{Q}(\alpha) : \mathbb{Q}]$, if

$$f(x) = \prod_{i=1}^k g_i(x)^{e_i} \pmod{p}$$

Then

$$p = \prod_{i=1}^k \mathfrak{p}_i^{e_i}$$

in $\mathbb{Q}(\alpha)$, and the degree of $g_i(\alpha) = f(\mathfrak{p}_i|p)$

We want to apply this lemma to $\mathbb{Q}(a^{\frac{1}{k_1}})/\mathbb{Q}$. But we need to make sure that $u^{k_1} - a$ is irreducible. Suppose it is not, then say $[\mathbb{Q}(a^{\frac{1}{k_1}}) : \mathbb{Q}] = m \mid k_1$. Then let q be a prime factor of $\frac{k_1}{m}$. Since $q|k_1$, $a^{\frac{1}{q}} \in \mathbb{Q}(a^{\frac{1}{k_1}})$. so $\mathbb{Q}(a^{\frac{1}{q}})/\mathbb{Q}$ is a subextension of $\mathbb{Q}(a^{\frac{1}{k_1}})/\mathbb{Q}$ with degree q . so $q|m$. But this is impossible because k_1 is squarefree, so we reach a contradiction, so $u^{k_1} - a$ is irreducible. And by our assumption $p \nmid k_1$. Then the lemma says that $u^{k_1} - a$ splits completely in \mathbb{F}_p iff p splits completely in $\mathbb{Q}(a^{\frac{1}{k_1}})$.

Now we finally establish the equivalence: p is counted by $P_a(x, k)$ iff p splits completely in $\mathbb{Q}(\zeta^k)$ and in $\mathbb{Q}(a^{\frac{1}{k_1}})$. But p splits in two fields iff it splits in the composite field (proven in chapter 4 of [10]). So We have

p is counted by $P_a(x, k) \leftrightarrow p$ splits completely in $\mathbb{Q}(\zeta^k, a^{\frac{1}{k_1}})$

6.3 Where the Generalized Riemann Hypothesis gets into place

Now we know that $P_a(x, k)$ counts the number of primes $\leq x$ that splits completely in $\mathbb{Q}(\zeta^k, a^{\frac{1}{k_1}})$. But p splits completely iff it's mapped to the identity of the Galois group. Let $n_k = [\mathbb{Q}(\zeta^k, a^{\frac{1}{k_1}}) : \mathbb{Q}]$. The Chebotarev Density theorem tells us that such primes has density $\frac{1}{n_k}$. Then $P_a(x, k)$ should be $\frac{1}{n_k} \frac{x}{\log x}$. Plug these into the expression of $N_a(x)$, we will get that

$$N_a(x) = \sum_{k=1}^{\infty} \frac{\mu(k)}{n_k} \frac{x}{\log x} + \text{error}$$

We will calculate the $\sum_{k=1}^{\infty} \frac{\mu(k)}{n_k}$ later, and this is indeed the expression for $A(a)$ in Hooley's proof.

The problem with this intuition is that the error of the Chebotarev Density theorem is too big to be directly plugged into the expression. We need some kind of bound to the error such that after our algebraic manipulation the error can still stay as an error term. And that's where the Generalized Riemann Hypothesis comes in: it can lead to a more precise bound for the Prime Number Theorem (and thus the Chebotarev Density theorem), such that there is more "room" for approximation. Assuming Generalized Riemann Hypothesis, Hooley essentially derived the Prime Ideal Theorem and effective form of the Chebotarev Density theorem. However, if we then plug in the effective form of Chebotarev, we still couldn't get then error to be small enough. The reason is that we don't have much control on the sign of $\mu(k)$, so during the approximation we have to think it as 1, and that causes the error to blow up.

What Hooley did in his proof is to decompose $N_a(x)$ into four parts. He chooses each part carefully that when he applies the corollary of generalized Riemann Hypothesis, the error of each one won't blow up. Eventually he shows that $\sum_{k=1}^{\infty} \frac{\mu(k)}{n_k}$ is actually the density.

To better illustrates his method, we need to define more notations and make some observations on them.

$N_a(x, y)$ denotes the number of primes $p \leq x$ such that $R(p, q)$ is not true for any $q \leq y$.

$M_a(x, y_1, y_2)$ denote the number of prime $p \leq x$ such that $R(p, q)$ holds for some prime q that $y_1 < q \leq y_2$

Below are some observations:

1. $N_a(x) = N_a(x, x-1)$. Because for any q that satisfies $R(p, q)$ should have $q|p$ so $q \leq p-1 \leq x-1$

2. $N_a(x) \leq N_a(x, y)$ for any y . That's because $N_a(x)$ = the number of all primes $\leq x$ - the number of p that satisfies $R(p, q)$ for some q , while $N_a(x, y)$ = the number of all primes $\leq x$ - the number of p that satisfies $R(p, q)$ for $q \leq y$. So the part being subtracted in $N_a(x, y)$ is a subset of the part being subtracted in $N_a(x)$

3. $N_a(x) \geq N_a(x, y) - M_a(x, y, x-1)$. That's because in the right handside of the inequality we subtract for twice the primes p that satisfies $R(p, q)$ for some $q \leq y$ and for some q that $y < q \leq x-1$

4. $M_a(x, t_1, t_3) \leq M_a(x, t_1, t_2) + M_a(x, t_2, t_3)$ because the right handside of the inequality over counts the primes that satisfies $R(p, q)$ for some $t_1 < q \leq t_2$ and some q that $t_2 < q \leq t_3$. We can think of this as the traingular inequality

Use these observatons we can get that

$$N_a(x) = N_a(x, t_1) + \mathcal{O}(M_a(x, t_1, t_2)) + \mathcal{O}(M_a(x, t_2, t_3)) + \mathcal{O}(M_a(x, t_3, x-1))$$

Where $t_1 = \frac{1}{6} \log x$, $t_2 = \frac{\sqrt{x}}{\log x^2}$, $t_3 = \sqrt{x} \log x$

It turns out that $\mathcal{O}(M_a(x, t_2, t_3))$ and $\mathcal{O}(M_a(x, t_3, x-1))$ can be approximated without assuming Generalized Riemann hypothesis. These two give $\mathcal{O}(\frac{x \log \log x}{\log x^2})$, and the computational details can be found in [7].

The Generalized Riemann Hypothesis is required for the approximation of $N_a(x, t_1)$ and $\mathcal{O}(M_a(x, t_1, t_2))$. The idea of deriving the Prime Ideal Theorem from Generalized Riemann Hypothesis is similar to how we derive the Prime Number Theorem with error bound from Riemann Hypothesis except that it's much more tedious([7]). Let $\pi(x, k)$ denotes the number of prime ideals \mathcal{P} in $\mathbb{Q}(\zeta^k, a^{\frac{1}{k_1}})$ such that $|\mathcal{P}| \leq x$, then assuming generalized Riemann Hypothesis we have the following error bound for Prime Ideal Theorem:

$$\pi(x, k) = Li(x) + \mathcal{O}(n_k \sqrt{x} \log kx)$$

But if we consider separately the primes that splits completely, use $\omega(x, k)$ denotes the number of prime ideals \mathcal{P} such that $|\mathcal{P}| \leq x$ and that the prime $p \in \mathcal{P}$ below it splits completely in $\mathbb{Q}(\zeta^k, a^{\frac{1}{k_1}})$ (and thus $|\mathcal{P}| = p$). Use $\omega(x, k)'$ to denote the number of \mathcal{P} with norm not exceeding x and p belows it ramifies in $\mathbb{Q}(\zeta^k, a^{\frac{1}{k_1}})$ (This happens iff $p|n_k$). Use $\omega(x, k)''$ to denote the number \mathcal{P} that is unramified but also not splits completely. Then we have

$$\pi(x, k) = \omega(x, k) + \omega(x, k)' + \omega(x, k)''$$

For \mathcal{P} counted by $\omega(x, k)$, there are n_k of \mathcal{P} that is above a p that splits completely, and the number of $p \leq x$ that splits completely is counted by $P_a(x, k)$. So we have

$$\omega(x, k) = n_k P_a(x, k)$$

Notice that each $p \in \mathbb{Q}$ can have at most n_k numbers of primes above it in $\mathbb{Q}(\zeta^k, a^{\frac{1}{k_1}})$, and $\|\mathcal{P}\| \geq p$ for $p \in \mathbb{Q}$ below \mathcal{P} . Also recall that p ramifies iff

p divides the discriminant of $\mathbb{Q}(\zeta^k, a^{\frac{1}{k_1}}) / \mathbb{Q}$, which is equivalent to $p|ak$ in our case. So

$$\omega(x, k)' \leq n_k(\text{number of prime divisor of } ak) \leq n_k \frac{\log ak}{\log 2}$$

For p unramified but doesn't split completely, $\|\mathcal{P}\| \geq p^2$. Thus

$$\omega(x, k)'' \leq n_k \sum_{p \leq \sqrt{x}} \leq n_k \sqrt{x}$$

So now we have

$$\pi(x, k) = n_k P_a(x, k) + n_k \mathcal{O}(\sqrt{x})$$

Now express $P_a(x, k)$ in terms of $\pi(x, k)$ and then plug in $\pi(x, k) = Li(x) + \mathcal{O}(n_k \sqrt{x} \log kx)$, we will get

$$P_a(x, k) = \frac{1}{n_k} Li(x) + \mathcal{O}(\sqrt{x} \log kx)$$

This is essentially the effective form of the Chebotarev density theorem.

Now back to $N_a(x, t_1)$ and $\mathcal{O}(M_a(x, t_1, t_2))$.

Let $k = \prod_{p \leq t_1} p$, k square free. Similar to how we get the formula for $N_a(x)$, we have

$$N_a(x, t_1) = \sum_{d|k} \mu(d) P_a(x, d) = \sum_{d|k} \frac{\mu(d)}{n_d} Li(x) + \mathcal{O}(\sum_{d|k} \mu(d) \sqrt{x} \log dx)$$

Now we can see why t_1 is chosen to be $\frac{1}{6} \log x$. $k = \prod_{p \leq t_1} p = e^{\theta(t_1)} \leq e^{2t_1} = x^{\frac{1}{2}}$. So for $d|k$, $d \leq x^{\frac{1}{2}}$, which means the number of divisor of k is also $\leq x^{\frac{1}{2}}$. Then we have

$$\sum_{d|k} \mu(d) \sqrt{x} \log dx \leq \sum_1^{x^{\frac{1}{2}}} \sqrt{x} \log x = x^{\frac{1}{2}} \log x$$

Now let S denotes the set of d that is square free and has at least one prime factor $> t_1$. Then we have

$$\sum_{d|k} \frac{\mu(d)}{n} Li(x) = \sum_{n=1}^{\infty} \frac{\mu(d)}{n_d} Li(x) + \mathcal{O}(Li(x) \sum_{d \in S} \frac{\mu(d)}{\varphi(d)})$$

The error can be verified to be bounded by $\mathcal{O}(\frac{x}{\log x^2})$

For $\mathcal{O}(M_a(x, t_1, t_2))$ bound it by $\sum_{t_1 < q \leq t_2} P_a(x, q)$. Then plug in the formula for $P_a(x, q)$ directly and some approximation shows that it is $\mathcal{O}(\frac{x}{\log^2 x})$

Thus we know that $N_a(x) = \sum_{k=1}^{\infty} \frac{\mu(k)}{n_k} \frac{x}{\log x} + \mathcal{O}(\frac{x \log \log x}{\log x^2})$. Now the last task is to evaluation $\sum_{n=1}^{\infty} \frac{\mu(k)}{n_k}$.

6.4 Formula of $A(a)$

Recall that $n_k = [\mathbb{Q}(\zeta^k, a^{\frac{1}{k_1}}) : \mathbb{Q}] = [\mathbb{Q}(\zeta^k, a^{\frac{1}{k_1}}) : \mathbb{Q}(\zeta^k)][\mathbb{Q}(\zeta^k) : \mathbb{Q}]$. We know that $[\mathbb{Q}(\zeta^k) : \mathbb{Q}] = \varphi(k)$ so only need to evaluate $[\mathbb{Q}(\zeta^k, a^{\frac{1}{k_1}}) : \mathbb{Q}(\zeta^k)]$.

Case 1.If k_1 is odd, for $k_1 = 1$ this is trivial. For $k_1 \geq 3$, let $k_1 = \prod_{i=1}^t q_i$. Then $\mathbb{Q}(a^{\frac{1}{k_1}})$ is the composite field of $\mathbb{Q}(a^{\frac{1}{q_i}})$. The only subfield of $\mathbb{Q}(a^{\frac{1}{q_i}})$ is \mathbb{Q} or itself since the degree of extension is a prime. So $\mathbb{Q}(\zeta_k) \cap \mathbb{Q}(a^{\frac{1}{q_i}})$ is either \mathbb{Q} or $\mathbb{Q}(a^{\frac{1}{q_i}})$. But for $q_i \geq 3$, $\mathbb{Q}(a^{\frac{1}{q_i}})$ is no longer a normal extension while all the subfield of $\mathbb{Q}(\zeta_k)$ is normal. Thus $\mathbb{Q}(\zeta_k) \cap \mathbb{Q}(a^{\frac{1}{q_i}}) = \mathbb{Q}$, so $\mathbb{Q}(a^{\frac{1}{k_1}}) \cap \mathbb{Q}(\zeta_k) = \mathbb{Q}$. Thus $[\mathbb{Q}(\zeta^k, a^{\frac{1}{k_1}}) : \mathbb{Q}] = k_1 \varphi(k)$

Case 2. If k_1, k is even, then say $k_1 = 2m$ so m is odd. Then $[\mathbb{Q}(\zeta_k, a^{\frac{1}{k_1}})] = \varphi(k)m$. Then $[\mathbb{Q}(\zeta^k, a^{\frac{1}{k_1}}) : \mathbb{Q}]$ can only be $\varphi(k)m$ or $2\varphi(k)m$ and it is $\varphi(k)m$ iff $\sqrt{a} \in \mathbb{Q}(\zeta_k)$.

Now consider $a = b^2 c$ where c is square free. so $\sqrt{a} \in \mathbb{Q}(\zeta_k)$ is the same as saying $\sqrt{c} \in \mathbb{Q}(\zeta_k)$. say $k = 2 \prod_{i=1}^m q_i$. Then the only quadratic subfields of $\mathbb{Q}(\zeta_k)$ are $\mathbb{Q}(\sqrt{q_1^* q_2^* \dots q_t^*})$ such that $q^* = (-1)^{\frac{q-1}{2}}$. So we need that $c = q_1^* q_2^* \dots q_t^*$ so $c|k$. Notice that c can't be $-q_1^* q_2^* \dots q_t^*$ because otherwise $\mathbb{Q}(\zeta_k)$ will contains i , which is impossible because $4 \nmid k$. Thus $c \equiv 1 \pmod{4}$ since each $q_i^* \equiv 1 \pmod{4}$. Thus we have the following:

$$n_k = \begin{cases} \frac{k_1 \varphi(k)}{2}, & \text{if } c \equiv 1 \pmod{4}, 2c|k \\ k_1 \varphi(k) & \text{if otherwise} \end{cases}$$

The last step is to evaluate $\sum_1^{\infty} \frac{\mu(k)}{n_k}$.

Case 1. if $c \not\equiv 1 \pmod{4}$ then $\mu(k), n_k$ are both completely multiplicative, so decompose the sum as product of terms involving prime. We eventually have

$$\sum_{k=1}^{\infty} \frac{\mu(k)}{n_k} = \prod_{q|h} (1 - \frac{1}{\varphi(q)}) \prod_{q \nmid h} (1 - \frac{1}{q \varphi(q)})$$

Let's denote this as $C(h)$ [7]

Case 2. if $c \equiv 1 \pmod{4}$. Then for $2c|k, n_k = \frac{k_1 \varphi(k)}{2}$ and otherwise $n_k = k_1 \varphi(k)$. Then we have

$$\sum_{k=1}^{\infty} \frac{\mu(k)}{n_k} = \sum_{k=1}^{\infty} \frac{\mu(k)}{k_1 \varphi(k)} + \sum_{2c|k} \frac{(k, h) \mu(k)}{k \varphi(k)}$$

We already know the first sum, and the second sum is $\sum_{k, (k, 2c)=1}^{\infty} \frac{\mu(2|c|k)(2|c|k, h)}{2|c|k \varphi(2|c|k)}$. This is similar to the previous sum, except that we have to get rid of the terms corresponds to prime factors of $2|c|k$. Eventually we will get

$$\sum_{k=1}^{\infty} \frac{\mu(k)}{n_k} = C'(h)(1 - \mu(|c|)) \prod_{q|h, q|c} (\frac{1}{q-2}) \prod_{q \nmid h, q|c} (1 - \frac{1}{q^2 - q - 1})$$

This is the formula for $A(a)$.

Acknowledgement

I would like to thank my friend Sophia for accompanying me during the program. I would like to thank little baby Deepesh Singhal for teaching me most of the materials. I would like to thank professor Andrei Jorza from my home institution who provides references I needed for this paper. I would like to thank my mentor Noah Taylor for guiding me throughout the process of writing the paper. I would also like to thank Peter May for organizing this program and offering the opportunities.

About the Author

Yuxin (Benny) Lin is a senior at Notre Dame majoring in mathematics with a minor in Japanese. She is a member of the Glynn Family Honors Program and the Department of Mathematics Honors Program. Her research on number theory was conducted at the University of Chicago REU program. During the academic year, she also conducts research on numerical semigroups. After graduating, Lin will be attending graduate school in number theory and aims to pursue a career in teaching and research in mathematics.



PUBLISH

Interested in publishing your research in the next issue of *Scientia* or presenting at the next Talk Science seminar? Email the editors at scientia@nd.edu.

Student Spotlight

Many Notre Dame students publish their scientific research in peer-reviewed journals each year. For this year's Student Spotlight section, we interviewed three of these students, including Jessamine Kuehn, Matthew Donahue, and Sophie Yue. Jessamine is a junior studying biochemistry and theology. Matthew is a senior studying biological sciences (ecology/environment and evolution/genetics tracks) and theology. Sophie is a junior studying science pre-professional and Chinese.

Title of research publication or topic:

Jessa: "Low pH facilitates heterodimerization of mutant isocitrate dehydrogenase (IDH1-R132H) and promotes increased production of 2-hydroxyglutarate"

Matthew: "Historical evolution may have facilitated the development of pesticide resistance in tetrodotoxin-resistant caddisflies"

Sophie: "Improving the Sexual Activity in Polycystic Ovary Syndrome in Animal Models: A Study in Zebrafish" (in submission) and "An Assistive Computer Vision Tool to Automatically Detect Changes in Fish Behavior In Response to Ambient Odor" (accepted to Scientific Reports in December 2020)

How did you become involved in undergraduate research?

Jessa: I emailed professors whose lab descriptions looked interesting on chemistry.nd.edu, and I was interviewed by Professor Katharine White in the spring of my freshman year. I worked in the lab over the following summer, after submitting a research proposal and receiving the Research Like A Champion (RLAC) grant from the Harper Cancer Research Institute.

Matthew: After intro bio lab confirmed my interest in research, I read on the department website about the faculty members with labs at Notre Dame and emailed those whose interests most closely matched mine just to talk about their research. I decided to join Dr. Jason McLachlan's lab and worked there for a year. The summer after my sophomore year, I did the UNDERC program and loved the work I did with my grad student mentor. He pulled me into his lab, and I have worked with Dr. Mike Pfrender since.

Sophie: I became involved in undergraduate research pretty early in my college career. I knew that this was something I wanted to pursue before coming to college, and so I actively searched for resources and opportunities my freshman year. I reached out to many upperclassmen regarding their research experiences, and they taught me how to reach out to faculty and gave excellent advice about what lab to join. I took note of any professors in the biology department whose research

piqued my interest, and drafted several emails expressing my desire to meet and discuss their work. I ended up having several meetings with different professors regarding their current research plans and chose the lab that I thought would give me the most hands-on experience.

What is your research topic and details of the lab in which you research?

Jessa: I work in the White lab in the Harper Cancer Research Institute, which focuses on how intracellular pH dynamics affect molecular mechanisms involved in cancer. My first individual project investigated the pH-sensitive mechanism of the R132H-IDH1 mutation recurrent in 70% of gliomas. With a further understanding of this mechanism, it may be possible to use this mutation as a drug target or biomarker for treatment or earlier diagnosis of cancer patients.

Matthew: I work in the Pfrender lab, and we study ecological and evolutionary genomics. My project explores the evolutionary history of caddisflies in the Pacific Northwest. Some populations of these caddisflies are resistant to both tetrodotoxin, a highly deadly poison in the newt eggs they eat, and pyrethroid and pyrethrin pesticides, which were applied in huge quantities during the 1950s and 1960s. Because both of the toxins target the sodium ion channel, we think the two may be related. I am sequencing their sodium ion channels, combing newspaper archives, learning biochemistry, and maybe even doing some modeling soon, to try to piece together this evolutionary puzzle. Ultimately, this research will have applications to conservation, agriculture, and evolutionary ecology.

Sophie: I currently work in the Li lab, which focuses on the development and function of the nervous system using zebrafish models. A large focus in our lab is cross-modal sensory communication, specifically, analyzing the interaction between olfactory and visual systems; in addition, we manipulate exposure to different hormones to study addiction patterns and/or their effects on sexual behavior. The first paper we completed centered on a polycystic ovarian syndrome zebrafish model used to analyze female sexual behaviors. We raised young adult female zebrafish with dissolved testosterone and compared their sex drive in mating conditions with control zebrafish. This research provided proof-of-concept of development of new strategies for treatment of reproductive diseases related to polycystic ovary syndrome.

Which journal do you plan to submit your research to, or where have you previously published your research?

Jessa: The paper will be submitted to ACS Biochemistry.

Matthew: I think Evolutionary Applications may be a good fit, but I'm not sure yet.

Sophie: Scientific Reports.

Do you have any advice for Notre Dame Students hoping to be involved with research at Notre Dame and for those who want to publish their research?

Jessa: I would not be discouraged if the first few professors you contact do not respond; I emailed 10 different professors and only 2 responded. If you want to participate in undergraduate research, just be persistent in sending emails to different professors indicating your interest in their lab. If you are interested in publishing research, mention that to your professor and ask if there is a project available that has potential to be ready for publication within 2 or 3 years. However, being one of the authors for a research publication does not necessarily indicate that you devote a significant amount of time to your research; in some cases someone is mentioned on a paper though they did minimal work on the project, while in other cases someone might spend years working on a project that is not completed during his or her time as a student.

Matthew: Reach out to professors and talk with them about their research! Scientists love talking about science, so even if there's no room in their lab, you'll learn a ton and have a great time. Also, don't be afraid to join a lab you aren't completely interested in. You can always switch if you don't like it, and if you do switch, you'll take a lot of knowledge with you.

Sophie: I strongly recommend joining medical/research societies. I was a part of Building Bridges, a mentorship program that paired students based on career interests, and my mentor was extremely helpful and willing to talk me through all aspects of her research experience. Many clubs send out opportunities for summer and abroad research positions through email, but on-campus undergraduate research is harder to advertise. Thus, for on-campus research, I recommend reaching out to upperclassmen and even professors you're familiar with to see if they can point you to any open doors. In addition, there's tons of research in different departments, so find a topic you're genuinely interested in and can see yourself enjoying in the long run (I have been in my lab for over 2 years and plan on staying until I graduate!).



Jessamine Kuehn, '22



Matthew Donahue, '21



Sophie Yue, '22

Alumni Spotlight

OLIVIA JAZBUTIS

Kara Miecznikowski graduated from Notre Dame in 2020, majored in biological sciences with a minor in journalism, ethics, and democracy, and lived in Howard Hall. Hailing from Chesterton, Indiana, she returned there the summer after her freshman year to lifeguard and volunteer.

The following summer, in 2018, she participated in the Summer Undergraduate Research Training (SMART) Program at Baylor College of Medicine in Houston, Texas. While there, she contributed to a project that investigated the correlation between stress response and recovery time—controlled by the hypothalamo-pituitary-adrenal (HPA) axis—and sex hormones. As part of the project, she conducted experiments using mouse models and a variety of assays to study the impact of estrogen and testosterone on corticosterone levels and hypothalamic gene expression. She also performed gonadectomies on mice, which sparked her interest in surgery. Through diligent research and attention to detail, she helped discover important temporal patterns in corticosterone levels between sexes and identified crucial time points for assessing hypothalamic gene expression.

In the summer of 2019, she worked as a summer associate at The diaTribe Foundation in San Francisco, California, a nonprofit that aims to improve the lives of people with diabetes and prediabetes through education and advocacy. Her primary role was to write articles for diaTribe Learn, a free patient-facing publication annually read by more than 2.4 million people. She researched complex pathologies and technological advancements. She then translated her findings to make them accessible to the general public, particularly to those without a scientific background. Since awareness and education are crucial in mitigating the prevalence and impact of diabetes, her work continues to have a direct impact on the lives of people with diabetes today. Looking toward the future, Miecznikowski plans to attend medical school beginning in the fall of 2021. In addition to practicing medicine, she aspires to sit on a medical ethics board, to write and edit for a medical ethics journal, and to continue conducting clinical research.

How did you get involved in research at Notre Dame? What kind of research did you do?

Reaching out to upperclassmen for advice and getting in contact with lab PIs after reading about their research on their respective department's website was especially helpful for me. Through my participation in the Biology Uplift Program, I was able to meet with upperclassmen on several occasions to discuss their research and shadow in a couple of labs. Then, after emailing PIs and learning more about their research, I joined Professor Bradley Gibson's Attention, Memory & Perception Lab in the Psychology Department at the end of my freshman year. I ended up working as a research assistant in this lab for the rest of my time at Notre Dame. As a research assistant, I studied how attention and working memory allow humans to concentrate on, retrieve, and maintain information. One study I helped with explored a possible correlation between pupil dilation and working memory capacity.

At Notre Dame, what helped you form your career goals? Engaging in conversations with my peers had a tremendous impact on my career goals. I became friends with a lot of really smart and motivated pre-med students at Notre Dame, and these friends continue to inspire me to this day!

Could you describe a bit about the work you've done since graduating?

I currently work at the American Hip Institute, an orthopedic clinic that specializes in hip arthroscopy and innovative medicine. As a clinical research assistant, I collaborate with the institute's fellows to author manuscripts for peer-reviewed journals. I have grown into a more perceptive and effective researcher as I collect and handle patient data, run statistical analyses, and engage with the publication process. Serving as a medical assistant in the clinic has also given me a wide range of clinical experiences, from taking vitals and managing reports in EMR to guiding patients through musculoskeletal assessments. These experiences, combined with shadowing various orthopedic hip, knee, and shoulder surgeries, have allowed me to contribute to high-quality treatment and have furthered my understanding of how medical teams work to deliver dynamic and compassionate care. In addition, I lead the institute's education initiative by creating medical articles and videos to educate patients and physicians alike; this role aligns my love of writing with my belief that accessible information supports patient autonomy and empowers patients to take charge of their health. I am particularly grateful for the guidance and mentorship that I have received from the institute's diverse group of physicians as I continue my journey in medicine.

What inspired you to pursue your current position?

I conducted some basic science research at Baylor College of Medicine during my undergraduate years, and although I was interested in the research aspects, I found that my interests lay outside of benchwork. After working as a research assistant in the Attention, Memory, and Perception Lab for three years, I knew that I wanted to continue doing research during my gap year. As I was interested in exploring research in a medical context, I pursued a clinical research position.

What advice do you have for undergraduates who want to be involved in scientific research?

Reach out! People want to help you—professors and fellow students alike. Research the different labs on campus and ask PIs if you can shadow in their labs so that you know if the research area is a good fit. Ultimately, the most important thing to keep in mind when getting involved with research is making sure that you are passionate about what you are studying. I ended up choosing psychology research because I had an interest in specializing in psychiatry, and I wanted to learn more about neurobehavioral disorders such as ADHD.



Kara Miecznikowski, B.S.,
Notre Dame Class of 2020

Talk Science

September 8, 2020

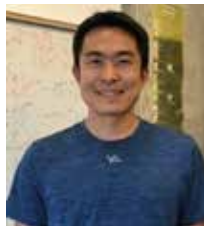


Dr. Dervis Vural
Department of Physics
*Evolution of Cooperation and
Specialization in Dynamic Fluids*

Isabel Snee
Neuriscience & Behavior '22
*Chiari I Malformation with
Klippel-Trenaunay Syndrome*



October 15, 2020



Dr. Yuhsin Tsai
Department of Physics
*Theoretical Intersection of Particle
Physics and Cosmology*

Kimberly Riordan
Honors Chemistry '21
*Synthesis of a Trigonal Pyramidal Sulfur
Radical and Exploration of Sulfur
Stability*



October 31, 2020



Dr. Christopher Patzke
Department of Biological Sciences
*Human Neurons and Synapses:
Development, Function, and Disease*

Gretchen Andreasen
Biological Sciences '21
*Temporal Effects on Route Selection by
the Woodland Deer Mouse, *Peromyscus
maniculatus**



February 25, 2021



Dr. Clive Neal
College of Engineering
Getting Humans Back to the Moon

Rhea DeSouza
Biochemistry and Anthropology '21
*The Effects of Diet-Induced Obesity and
Ketogenic Diet on Cancer Progression*



April 1, 2021



Dr. Zach Schafer
Department of Biological Sciences
*Regulation of Cancer Cell Death and
Metabolism by Attachment to Extracel-
lular Matrix*

Alex Kokot
Honors Mathematics and Philosophy '21
*Applications of Differential Geometry to
Computer Vision*



April 25, 2021



Dr. Tim Beers
Department of Physics
*Archaeology of the Stars: Evidence
for the Origin and Evolution of the
Elements*

Shannon Steines
Biological Sciences '22

*Characterizing the Retinal Pigment
Epithelium During Retinal Regeneration
in Zebrafish*



JOIN US

Want to help publish the next issue of *Scientia*?
We are currently seeking reviewers, editors,
news columnists, and graphic designers for the
upcoming semester.
Email scientia@nd.edu for details.

